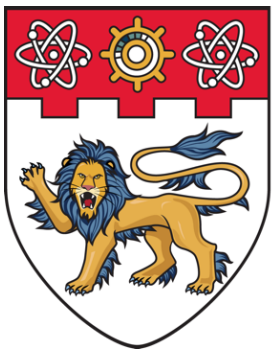

NANYANG TECHNOLOGICAL UNIVERSITY
SINGAPORE

THERMAL PERFORMANCE OF CONDUCTION AND FORCED CONVECTION IN THREE-DIMENSIONAL PRINTED LATTICE STRUCTURES

ZHOU YI

SCHOOL OF MECHANICAL AND AEROSPACE ENGINEERING

NANYANG TECHNOLOGICAL UNIVERSITY

2022

THERMAL PERFORMANCE OF CONDUCTION AND FORCED CONVECTION IN THREE-DIMENSIONAL PRINTED LATTICE STRUCTURES

By

ZHOU YI

A thesis submitted to the Nanyang Technological University

in partial fulfillment of the requirement for the degree of

Doctor of Philosophy

School of Mechanical and Aerospace Engineering

2022

Statement of Originality

I hereby certify that the work embodied in this thesis is the result of original research, is free of plagiarized materials, and has not been submitted for a higher degree to any other University or Institution.

Jan-19-2022	Zhou Yi
. . . . .	.....
Date	[Input Name Here]

Supervisor Declaration Statement

I have reviewed the content and presentation style of this thesis and declare it is free of plagiarism and of sufficient grammatical clarity to be examined. To the best of my knowledge, the research and writing are those of the candidate except as acknowledged in the Author Attribution Statement. I confirm that the investigations were conducted in accord with the ethics policies and integrity standards of Nanyang Technological University and that the research data are presented honestly and without prejudice.

Jan-19-2022 Duan Fei

. . . . . .

Date [Input Supervisor Name Here]

Authorship Attribution Statement

*(B) This thesis contains the materials from 2 papers published in the following peer-reviewed journal(s) / from papers accepted at conferences in which I am listed as an author.

Chapter 4, is partially published as

Y. Zhou, F. Duan. Heat Conduction Performance of 3D Printed Lattice Structure. The 15th International Conference on Heat Transfer, Fluid Mechanics and Thermodynamics (HEFAT) and Editorial Board of Applied Thermal Engineering (ATE) 26-28 Jul 21.

The contributions of co-authors are as follows:

- Prof F. Duan provided the initial project direction and edited the manuscript drafts.
- I prepared the manuscript drafts.
- I designed and fabricated the test samples at Singapore Centre for 3D Printing.
- I performed the simulation and laboratory work at the School of Mechanical and Aerospace Engineering, as well as analyzed the data.

Chapter 6, is partially published as

S. Shen, B. B. Kanbur, **Y. Zhou**, and F. Duan. Thermal and Mechanical Assessments of the 3D-Printed Conformal Cooling Channels: Computational Analysis and Multi-objective Optimization. Journal of Materials Engineering and Performance 2020, 29: 8261–8270. https://doi.org/10.1007/s11665-020-05251-5.

The contributions of co-authors are as follows:

- Prof F. Duan provided the initial project direction and edited the manuscript drafts.
- S. Shen, B. B. Kanbur, and I prepared the manuscript drafts.
- I designed and fabricated the samples.
- S. Shen performed the numerical simulations.
- B. B. Kanbur conducted the multi-objective optimization programming.
- I performed the laboratory work and analyzed the data at the School of Mechanical and Aerospace Engineering.

Jan-19-2022	Zhou Yi
.....	.....
Date	[Input Name Here]

Abstract

The lattice structure is promising for the application as heat exchange media due to its porous and controllable geometric characteristics. The recent developments in three-dimensional (3D) printing technology make the post-process-free and eco-friendly fabrication of complex-shaped lattice structures possible, while the potential of 3D printing for manufacturing thermally used lattice structures has not been explored. In this study, different types of lattice structures are designed and developed for analyzing and further controlling the thermal performance in conduction and forced convection. Based on the findings from thermal performance analysis, the lattice structure is integrated with a conformal cooling channel design to improve the productivity of plastic injection molding. The first effort of this study is to employ experimental and numerical methods to study the steady-state thermal conduction mechanism in lattice structures used as lightweight materials. A conjugated 3D heat transfer model accounting for the flow pattern of lattice structure coupled air has been built. The quantitive agreement on effective thermal conductivity is observed by comparing the experimental and simulation results. The effects of lattice structure design variables on the conductive heat transfer performance are analyzed in detail. The results reveal that either decreasing the porosity or specific surface area strengthens the conductive heat transfer in the specific typed lattice structure. The effective thermal conductivity can also be adjusted by varying the cross-section area along the main heat conduction direction, which is firstly found in the thermal conduction study. The analysis of parameter studies provides direct and effective methods for controlling the thermal conduction performance of lattice structures by setting the structure design variables.

The second effort of this study is to experimentally and numerically investigate the hydraulic and thermal characteristics of different lattice structures in air-forced convection. A 3D steady-state conjugated heat transfer model has been developed, in which incompressible turbulent airflow is defined. The simulated pressure drop gradient values fit well with the experimental ones, which support the effectiveness of experiments and simulation models meanwhile. The numerically reproduced temperature and velocity contours visually present the temperature distributions in different lattice structures and flow motions in the coupled air, which are found in agreement with the experimentally derived orders of convective heat transfer efficiency and fluid media transfer capability. The lattice structures with a larger inter-facial surface area and a more complex topology exhibit better convective heat transfer capability, while the one with a larger open area ratio performs lower flow resistance. The findings benefit the heat exchanger design by providing scientific improvement fundamentals on lowering the pumping power needed and enhancing the forced convective heat transfer efficiency. Finally, based on the results from conductive and forced convective thermal performance investigations, lattice structures are integrated into the conformal cooling channel design in a specific plastic injection mold for balancing the objectives of minimum plastic cooling time, minimum plastic surface temperature non-uniformity, and minimum pressure drop from the coolant inlet to the outlet. The channel dimensions are optimized and determined by the multi-criteria decision making approach, and then both experimental and numerical investigations are performed on the 3D printed molds with optimized conformal cooling channels. A 3D transient conjugated heat transfer model has been developed to simulate the cooling process of plastic, which is validated by experiments in terms of pressure drop and cooling time. The integration of lattice structures shortens the cooling time dramatically

by enhancing conductive and forced convective heat transfer efficiencies in channels at the cost of slightly increased temperature non-uniformity and pressure drop. The use of lattice structures in conformal cooling channel design has been proved effective for promoting the productivity of plastic injection molding, hence the lead time and cost are reduced significantly. To sum up, the lattice structure is a promising solution for thermal management in which the controllable thermal performance of conduction and forced convection is wished. Future recommendations call for utilizing 3D printing technology to facilitate the innovative designs and fabrications of lattice structures in broadened thermal applications.

Acknowledgments

Firstly, I would like to express my sincerest gratitude to my supervisor, Associate Professor Fei Duan. Without his guidance in the research and daily life, I cannot continue with the Ph.D. study till now. His patience, kindness, and understanding help me overcome the hard days in the past five years. His efficient working style and optimistic attitude always inspire me a lot.

Second, I would like to sincerely express my appreciations to my co-supervisors, Dr. Tong Liu and Dr. Peifeng Li for their encouragements and the academic resource support in the past years. My gratitude also goes to my friends and colleagues, especially Dr. Baris Burak Kanbur, Dr. Suping Shen, Mr. Chenlong Wu, and Dr. Junheng Ren. The friendship with them benefited me too much in the past, and will continue warming me in the future.

Thirdly, I also need to say thanks to the technicians from Energy Systems Lab and Singapore Centre for 3D Printing (SC3DP). They provided professional suggestions on the use of equipment at the beginning of my research, and helped me a lot with the purchase of experimental instruments.

Besides, I would like to thank my family's understanding, and support during the past five years.

Last but not least, I would like to thank SC3DP provided the scholarship and the 3D printing facilities to be used for my studies.

Contents

List of figures

List of tables

List of Symbols

Symbols

$A_{c.}$	Cross-section area, [mm^2]
C_F	Forchheimer coefficient
C_p	Specific heat capacity, [J/kg°C]
D_h	Hydraulic diameter, [mm]
d	Layer thickness, [mm]
E	Laser power, [W]
f	Friction factor
H	Unit cell length, [mm]
h	Scan spacing, [mm]
h_c	Heat transfer coefficient, [W/m^2K]
K	Permeability, [m^2]
$\dot{M}$	Mass flow rate, [kg/s·]
NT	Normalized temperature
Nu_c	Nusselt number based on channel hydraulic diameter
P	Laser power, [W]
ΔP	Pressure drop, [Pa]
q	Heat flux, [W/m^2]
T	Temperature, [K]
u	Scan rate, [mm/s]
$\vec{V}$	Flow velocity, [m/s]
V	Volume, [mm^3]

Greek Symbols

Ψ	Laser energy density, [J/mm^3]
η	Fractional density
λ	Thermal conductivity, [W/m°C]
ε	Porosity
ϕ	CCCs channel diameter
η	Convective heat transfer rate
ρ	Density, [kg/m^3]
μ	Dynamic viscosity, [Pa·s]

Subscripts

eff	Effective
f	Fluid
l	Lower
r	Relative
s	Solid
u	Upper

Abbreviations

BCC	Body-centred cubic
CCC	Conformal cooling channel
DMLS	Direct metal laser sintering
FCC	Face-centred cubic

Chapter 1. Introduction

1.1. Background

The lattice structure is an architecture formed by an array of spatial periodic unit cells with edges and faces [1]. As Figure 1.1. Industrial applications of lattice structures as: (a) construction structure, (b) energy absorber, and (c) support in mold cooling channels shows, since it has many excellent physical properties, the lattice structure has been widely used as a promising solution for a mass of applications, such as a lightweight construction structure due to the high specific strength [2], an energy absorber due to the excellent anti-compression ability [3], and a support in mold cooling channels due to the high strength and long fatigue life [4]. The most distinguishing characteristic of lattice structure is the regularly shaped porous topology, as well as the derived large surface area and tortuous solid profile, which make it popularly used as heat exchange media in thermal applications [5–7].

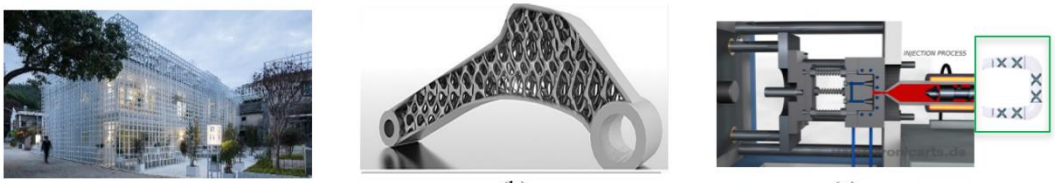

Figure 1.1. Industrial applications of lattice structures as: (a) construction structure, (b) energy absorber, and (c) support in mold cooling channels

The traditional manufacturing methods including investment casting, deformation forming, and textile techniques have been employed to manufacture lattice structures [8]. However, these approaches are categorized as subtractive manufacturing which wastes massive raw materials in fabrication, and further integration or bonding

processes are required to form the designed structure. In addition, the possible types of lattice structures are very limited when employing the traditional subtractive manufacturing methods. The introduction of metal three-dimensional (3D) printing provides an effective methodology to manufacture satisfactory metal lattice structures. Since the use of fixtures, cutting tools, coolants, and other auxiliary post-process is not required in the 3D printing technology, many resources can be saved [9]. Selective laser melting (SLM) and direct metal laser sintering (DMLS) are the ones of the best performance-to-cost ratio metal 3D printing techniques, which share the same fabrication principle and process. The advantage of SLM and DMLS over other 3D printing techniques is the capability of producing complex-shaped structures from relatively high thermal conductivity metallic powders, which enables the fabrication of thermally used lattice structures that caters to the demands of efficient heat exchange media from the industries.

For investigating lattice structure properties, too much attention was paid to the mechanical properties such as failure behavior [10], strength [11], energy absorption capability [12], fatigue life [13], and so on. However, a limited amount of researchers tried to investigate thermal properties of them. In the thermal management, the lattice structure fabricated via the metal 3D printing technology is potential for controlling the thermal performance of conduction and forced convection due to its adjustable spatial geometric parameters.

As porous structures, lattice structures are promising for functioning as heat exchange media. The effective thermal conductivity is one of the key thermo-physical properties of the heat exchange media [14]. Many analytical and numerical models have been applied to predict the effective thermal conductivity of porous structure, which ought to be effective in lattice structures. But the analytical models all employ the porosity to

predict the effective thermal conductivity of multi-phase material, without analyzing the effect of structure topology on the effective thermal conductivity. The lattice structure topology is strongly related to the porosity, conduction area, and characteristic length. As each geometric factor may affect the effective thermal conductivity dramatically, it is necessary to investigate the more detailed effects of structural parameters on the effective thermal conductivity, so as to better control and utilize the heat conduction process in industry.

The lattice structure can also be defined as cellular structures, which are made of repeated unit cells. The cellular structure with high porosity is always used as heat exchange media to transfer heat through the heat convection process. Hence, the lattice structures ought to have the promising applications used as heat exchangers to dissipate the heat through the forced heat convection. The hydraulic and heat transfer characteristics are the two most popular concerns to evaluate the performance of the heat exchange media. The ones with the relatively low needed pumping power and the relatively high heat transfer efficiency are preferred in industries. In this condition, the analysis of parameter study on lattice structure convective characteristics is beneficial to the heat exchanger design.

There are many applications utilizing the excellent mechanical properties of lattice structures, integrating them with the conformal cooling channel (CCC) design is one of them. The CCCs are designed to follow the plastic injection mold outer profiles, so as to dissipate the heat transferred from the hot plastic in the plastic injection molding process. The integration of lattice structures enhances the anti-compression capability and elongates the fatigue life of the mold. However, using the lattice structures to improve the cooling performance of CCCs has not been investigated. Actually, employing the lattice structures as the media in the CCCs increases the contacting

surface area for the convective heat transfer, and the lattice structures also build additional heat conduction paths in the CCCs to increase the heat transfer rate. Since the cooling performance is the most concern in plastic injection molding, making full use of lattice structure thermal performance in conduction and forced convection is useful to promote the productivity.

In summary, thanks to the development of 3D printing, the lattice structure has been becoming one of the most popular porous media used in the thermal management. Compared to the stochastic porous heat exchange media, the lattice structure has controllable thermal performance due to the adjustable geometric parameters. Till now, the heat conduction studies on lattice structures were still confined to employing the porosity value related analytical models to determine the effective thermal conductivity, which ignores the effects of structural parameters. Besides, the lattice structure can also be used as the heat exchange media to accelerate the forced convective heat transfer process, but it is necessary to achieve a perfect balance between the high heat transfer rate and low pumping power needed. Finally, the CCC design in the plastic injection molding can combine the conductive and convective heat transfer characteristics of lattice structure, which really realize the thermal management and application of lattice structure beyond theories.

1.2. Research objectives and scopes

In the present study, the body-centered cubic (BCC), face-centered cubic (FCC), and octet-truss lattice structures with different dimensional parameters are fabricated by the SLM system, and the optimized CCCs are fabricated by the DMLS system. The objectives of this work are summarized below:

- Controlling the conductive and convective heat transfer performance of lattice structures by studying the effects of structure design variables.
- Applying lattice structures in the conformal cooling channel design to improve the productivity of plastic injection molding.

This thesis aims at investigating the steady state heat conduction and air forced connection processes in different types of lattice structures, so as to better manage the thermal applications of them in industry. The scopes are listed as follows:

- Design and fabricate different typed lattice structures with variable structural parameters.
- Investigate the steady-state heat conduction performance of lattice structures.
- Investigate the hydraulic and convective heat transfer characteristics of lattice structures.
- Design, optimize, and fabricate the conformal cooling channel containing lattice structures for a specific plastic injection mold, to realize the thermal management of lattice structure in the industry.

1.3. Thesis layout

The thesis is organized in accordance with the study sequence, and the layout is shown as follows:

Following Chapter 1 of introduction, Chapter 2 reviews typical metal 3D printing methods firstly. The advantages and flow process of SLM or DMLS are then elaborated. After that, the development and geometric characteristics of different lattice structures are presented. Besides, several analytical models used for predicting the effective thermal conductivity of the porous structure are listed to show previous studies on

porous structure heat conduction process. Then, the previous investigations on convective heat transfer characteristics of cellular structures are narrated clearly as the reference resources for studying the forced convection process in lattice structures. Finally, the development of conformal cooling channel in the plastic injection molding industry is reviewed.

Chapter 3 shows the unit cell geometric design of lattice structures, and the design and fabrication of test samples for the heat conduction and convection experiments. As the test samples are fabricated by the commercial SLM system, the setting and validation of the related process parameter are also included in this chapter.

Chapter 4 summarizes the experimental and numerical investigations of the steady state heat conduction process on SLM processed lattice structures. In this chapter, the effects of structural parameters on the effective thermal conductivity are studied, and a new conception of the specific thermal conductivity is introduced for helping the industry select the lattice structures based on lightweight characteristic and good conductive properties at the same time.

In Chapter 5, the air forced convection experiments are conducted on different SLM processed lattice structures, and numerical simulations were used to support the reliability of experimental data. The correspondent hydraulic and convective heat transfer characteristics are derived under the different air flow velocity values. The comparisons of hydraulic and heat transfer characteristics among different lattice structures are used for the further reasonable use of the lattice structure as heat exchange media in industry.

Chapter 6 illustrates an example of using lattice structure as heat exchange media in the conformal cooling channels. In this chapter, an entire process of design, computational

simulation, multi-objective optimization, fabrication of optimized designs, and validation experiments on the 3D printed design are involved. The hydraulic and cooling performance of the used lattice structures are summarized for further and better applying lattice structures as heat exchange media.

Chapter 7 presents the main conclusions from Chapter 4 to Chapter 6, as well as the recommendations for the future work. The future recommendations focus on building a comprehensive decision system for screening the best lattice structure design with optimized structural parameter values in the conformal cooling. Prior to inputting big data of the specific CCCs and specific lattice structure designs to the system, the controllable heat conduction and forced convection should be both considered at the design stage.

Chapter 2. Literature review

The present review includes: (i) development of metal 3D printing, (ii) brief introduction of SLM and DMLS, (iii) development history and geometric characteristic summary of lattice structures, (iv) analytical models for predicting the effective thermal conductivity of multi-phase materials, (v) convective heat transfer studies on cellular structures, and (vi) development of conformal cooling channels in the plastic injection molding.

2.1. Metal 3D Printing

The birth of metal 3D printing can be tracked back to 1962, when Seagle et al. [15] proposed Electron Beam Melting (EBM), a printing method that creates 3D objects by employing an electron beam to melt metallic or alloyed powders layer after layer. Over the past decades, a mass of metal 3D printing methods have been emerging in the market. American Society for Testing Material (ASTM) defined 3D printing as 'a process of joining materials to make objects from 3D model data, usually layer upon layer, as opposed to subtractive manufacturing methodologies' [16-19]. This definition summarized the basic principle of all 3D printing methods: fabricating 3D solid objects layer by layer. Although sharing the same basic principle, different metal 3D printing methods have different manufacturing processes, working environments, materials feeding systems and layer binding mechanisms. In engineering applications, the reasonable choice of metal 3D printing methods depends on an overall understanding of their developing histories and characteristics.

EBM was proposed by Seagle in 1962 and identified as one of the earliest metal 3D printing methods, which employs the focused electron beam to melt metallic powders in a vacuum environment [15].

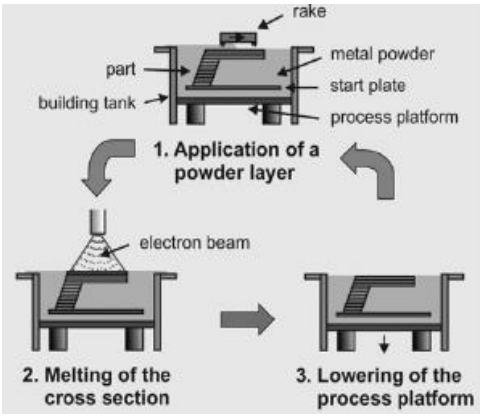

Figure 2.1. Flow process of fabricating objects by Electron Beam Melting [15]

In 1992, Deckard invented the Selective Laser Sintering (SLS) system to fabricate complex parts and freeform solid articles from heat-fusible powders [20]. Figure 2.2 shows the schematic diagram of it. Different from the electron beam fixed in the EBM system, a focused laser beam is selected as the energy source in the SLS system to melt metallic powders partially. The partial melting cannot provide enough wettability for powders to bind together, therefore binder materials are indispensable in SLS manufacturing process [21]. Due to use of binder materials, the SLS manufacturing cost increases, and the partial melting also results in the poor density of final parts.

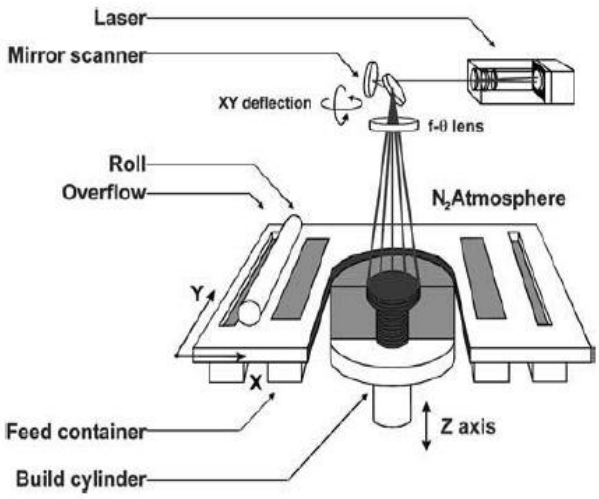

Figure 2.2. Schematic diagram of Selective Laser Sintering [22]

The EBM and SLS system are usually employed to produce parts by one kind of metals. Laser Engineering Net Shaping (LENS) is a useful method when manufacturing new geometric features by different metal materials. The concept of LENS was firstly proposed by Atwood in 1998 [23], and the corresponding schematic diagram is shown in Figure 2.3. In the LENS system, the material delivery system is composed of two nozzles whose heads are coaxially with the laser beam along the *z* direction. These two nozzles can spray two different kinds of metallic powders onto the substrate or deposition layers. In the *x*-*y* plane, the building table is able to move in parallel and rotate about the *x* or *y* axis. Compared with EBM and SLS system, the LENS system has a building table with more freedom, therefore it is capable of creating intricate geometric features on existing parts.

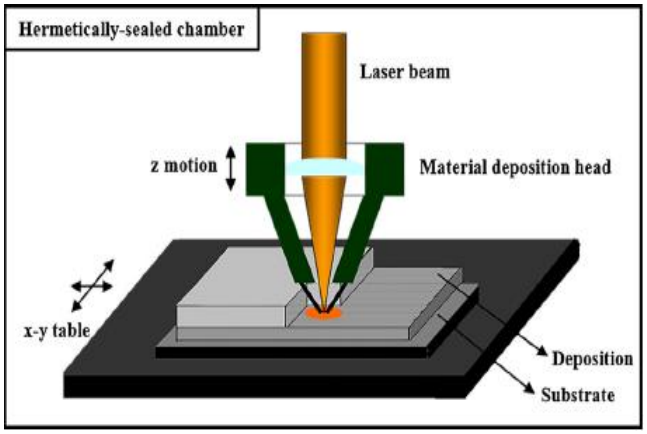

Figure 2.3. Schematic diagram of Laser Engineering Net Shaping [24]

In the chronological order, after EBM, SLS and LENS had been introduced to the manufacturing market, the first commercialized Selective Laser Melting (SLM) system was invented by SLM Solutions Company in 2000. The principle and process of SLM are very similar to SLS. The most distinct difference is that SLM uses a higher power focused laser beam to melt powered materials totally into liquid phase. The details of SLM will be discussed in the next section.

The Ultrasonic Consolidation (UC) system was proposed by White in 2003 [25], and its schematic diagram is shown in Figure 2.4. In the UC system, feedstock materials are metal foils. In the manufacturing process, a high frequency ultrasonic energy source induces combined static and oscillating shear forces within metal foils to generate solid-state bonds [26]. After realizing the interlayer bonding by ultrasonic welding, a computer numerically controlled (CNC) milling machine creates the geometric profile of each layer by contour milling. The UC system takes advantages of additive and subtractive techniques allowing metal parts to be formed with the adequate dimensional accuracy. In the UC manufacturing process, there are no phase changes of raw materials, so less power is consumed than other metal 3D printing methods.

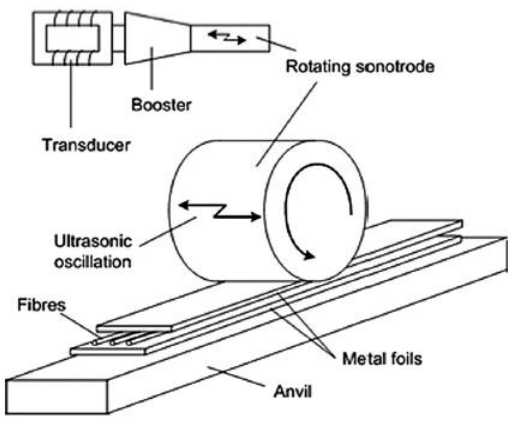

Figure 2.4. Schematic diagram of Ultrasonic Consolidation [27]

At present, the five metal 3D printing methods narrated above are the most popular ones used in the manufacturing industry. In order to distinguish and investigate applications of different metal 3D printing methods, it is necessary to categorize them in certain rules. Based on the phase state of raw materials, all 3D printing methods can be sorted into three types: liquid-based methods, solid-based methods, and powder-based methods [28]. Considering no liquid phase feedstock materials have been used in commercial metal 3D printers till now, metal 3D printing methods could be classified into two kinds: solid-based methods and powder-based methods. Table 2.1. categorizes and summarizes characteristics of EBM, SLS, LENS, SLM and UC in detail.

The development of metal 3D printing improves the ability of manufacturers to fabricate more complex 3D structures within less lead time. In addition, compared with the traditional subtractive manufacturing, the cost can be saved by metal 3D printing because unprocessed materials are qualified for the next use. The selection of 3D printing methods based on their own characteristics is beneficial for manufacturers to make full use of metal 3D printing.

Table 2.1. Characteristics of typical metal 3D printing methods [28]

	Methods	Energy source	Binding mechanism	Working environment	Materials delivery system
Solid-based	UC	Sonotrode	Ultrasonic welding	Normal	Roller
Powder-based	LENS	Laser beam	Melting	Hermetically-sealed	Nozzles
	SLS	Laser beam	Partial melting	Inert gas	Roller
	SLM	Laser beam	Melting	Inert gas	Recoater
	EBM	Electron beam	Melting	Vacuum	Rake

2.2. Selective laser melting

2.2.1 Introduction

In the term of the performance to price ratio, SLM is the best method for fabricating intricate metal 3D structures, same as its transformed version of DMLS, which shares the same manufacturing principle with it and just developed by the other company. Nowadays, SLM and DMLS have become the latest developed 3D printing technologies employed to manufacture high-quality, complex, and reliable alloy parts with relatively high resolutions and good dimensional accuracy controls.

In the manufacturing process of them, the 3D parts were created following two principles: one is fabricating designed 3D structures layer by layer, and the other one is bonding adjacent layers by the total melting.

In the condition that neither the SLM nor DMLS system is able to process 3D CAD drawings, a specific software MAGICS is used to slice the 3D CAD model into a stack of 2D layers which describe detailed geometric characteristics of the part. Then, each layer of metallic powders is scanned and melted by a high-power focused laser beam on

the required 2D cross-section area. After finishing processing one layer, a further layer of powders is spread on top of the previous one. By repeating laser scanning and feeding processes, subsequent layers are created and simultaneously bonded to existing deposition layers until the entire stack of 2D layers has been processed and bonded together to form the original 3D CAD solid model (see Figure 2.5).

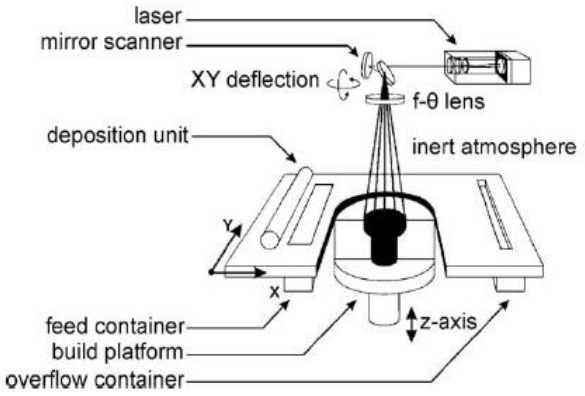

Figure 2.5 Schematic diagram of Selective Laser Melting [29]

2.2.2 Laser System Parameters

As the laser system is the most important composition part in the SLM system, parameters of it have significant effects on phase changes of powders and the density of finished parts. Olakanmi et al. [30] studied relationships between the density of SLM processed AlSi12 parts and laser power, scan rate, layer thickness, and scan spacing in attempt to obtain the highest density via one-by-one variables tests.

In order to attain a more accurate analysis, Ghosh et al. [31] employed the analysis of variance (ANOVA) to statistically study effects of different laser system parameters on the density of final parts. As their conclusion showed, the contribution percentages of laser power, layer thickness, scan rate, and scan spacing on the density of final parts were 5.98%, 13.55%, 3.64%, and 72.81% separately.

Laser energy density is the most important parameter influencing the densification of SLM processed parts. Moreover, it is also a comprehensive parameter determined by laser power, layer thickness, scan rate, and scan spacing. The corresponding relationship is shown in Eq. (2.1).

$$\Psi = \frac{E}{uhd} \tag{2.1}$$

where ψ = laser energy density (J/mm^3), E = laser power (W), u = scan rate (mm/s), h = scan spacing (mm), and d = layer thickness (mm). The conception of laser energy density summarizes all laser system parameters influencing the density of final parts into one, which simplifies the investigation of laser system in the SLM or DMLS system.

Furthermore, Simchi et al. [32] found out there is a direct relationship between the fractional density of SLM processed parts and input laser energy density. They concluded that the fractional density ϑ is an exponential function of input laser energy density (ψ), as shown in Eq. (2.2).

$$\vartheta = C_1 - C_2 e^{-K\psi} \tag{2.2}$$

where C_1, C_2 and K are material constants of feedstock powders.

In order to validate Eq. (2.2), Cochrane et al. [30] fabricated aluminum alloyed AlSi12 parts by SLS. As shown in Figure 2.6, with the increment of input laser energy density, the density of parts increases continuously until reaches a peak value. This phenomenon matches Eq. (2.2). However, beyond a certain value of input laser energy density, the part density almost remains unchanged even decreases when the input laser energy density still increases. It indicates that the input laser energy density over the saturation value will result in excessive fluid phase materials which lead to agglomeration and layer delamination of final parts.

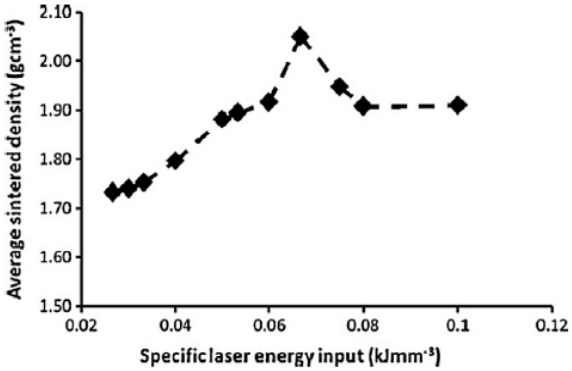

Figure 2.6. Relationship between the density of SLS processed part and input laser energy density [30]

2.2.3 Feedstock Materials

It was noted that the satisfying setting of laser system parameters is insufficient to facilitate the densification mechanism. The choice of materials affects the densification significantly and determines mechanical and thermal properties of final parts. Many researchers have been trying to employ different kinds of metallic powders in the SLM system. Table 2.2 summarizes properties of the most popular raw materials after being processed by SLM.

Table 2.2. Properties of SLM processed materials [33]

Material	Density (g/cm^3)	Thermal conductivity (W/m·K)	Specific heat (J/kg·°C)	Ultimate tensile strength (MPa)	Yield Strength (MPa)	Manufacturer
AlSi10Mg	2.67	119±5	910±50	460±20	240±10	EOS GmbH
Stainless steel 316L	7.99	16.2	N.A.	624±17	494±14	Renishaw
TiAl6V4	4.41	N.A	N.A.	970	930	Arcam AB
Inconel 625	N.A.	9.8	N.A.	1034	N.A.	American Elements

Note: N.A.: Not Available

Based on specific properties, each SLM raw material has certain applications. Considering AlSi10Mg parts have the excellent strength to weight ratio, Ferro et al. [33] employed the SLM system to fabricate AlSi10Mg impact absorbers embedded in aircraft wings. TiAl6V4 powders with high tensile and yield strength were used as SLM raw materials to process cortical bones for medical purposes [34]. Stainless steel 316L has high corrosion resistance and biocompatibility properties, Prihandana et al. [35] made full use of its advantages for the manufacture of micro-filters. The most extraordinary property of inconel-625 is that the outstanding strength and toughness could be maintained within a wide temperature range, so that typical applications of Inconel 625 were heat shields, furnace hardware, gas turbine engine ducting, combustion liners, etc. [36].

No matter which materials are used in the SLM system, all of them could be recycled for the next use as long as they have not experienced phase changes during the manufacturing process. Ardila et al. [37] and Seyda et al. [38] conducted a series of experiments to test qualities of recycled powders and final parts, they concluded that even after 13 recycling cycles of metallic powders, there were almost no significant changes in powder properties and finished parts qualities (see Figure 2.7). In their studies, the quality of final parts was represented by porosity, the larger the porosity, the poorer quality final parts have.

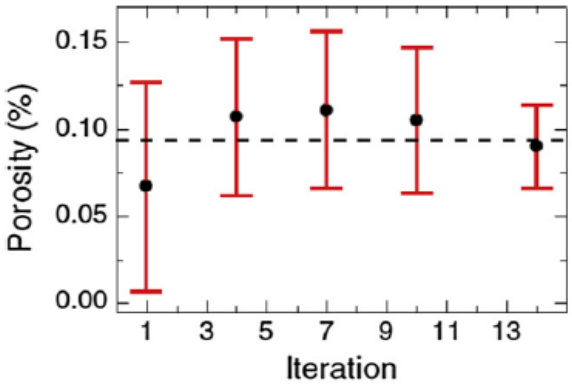

Figure 2.7. The relationship between recycling times and porosity (%) of finished parts [37]

The development of SLM creates a new opportunity to fabricate complicated structures beyond capabilities of traditional manufacturing methods efficiently and effectively, and it also achieves a perfect balance between the finished parts quality and cost. At present, more and more companies are trying to make full use of it. As a result, evaluating and predicting properties of SLM processed samples are meaningful and beneficial before batch productions.

2.3. Lattice Structures

The stiffness and strength to weight ratio of sandwich panels are much higher than conventional structural sections, so that the application of sandwich structures was increasing in various fields including aerospace, automotive, marine, and defense industries [39]. Figure 2.8 shows the structural compositions of a typical truss-core sandwich panel. A sandwich panel is a three-layer element, made up of two flat facing plates and a thick core of low average strength and density is attached between them [40]. The main function of the core is to improve energy absorption capacity of the whole structure. Over the past decades, cellular structures have been the most popular ones selected as cores of sandwich panels for their excellent mechanical properties.

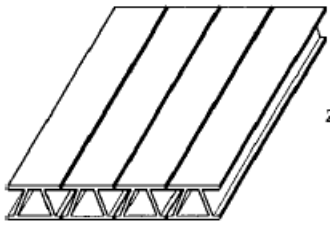

Figure 2.8. Truss-core sandwich panel [40]

In order to explore and compare properties of different cellular structures, Bhate et al. [41] classified them into four types: honeycomb, lattice, open-cell foam, and closed-cell foam, as shown in Figure 2.9. In the term of materials reduction, open-cell foams and lattice structures are better owing to their relative high porosity values.

Lattice structures are similar to open-cell foams in appearance , both of them are composed of regular cell units, and several struts with highly hierarchically orientations make up the unit cell. The difference between open-cell foams and lattices are their different mechanical deformation mechanisms. Typically, the open-cell foams were considered as bending-dominated structures, which were used to absorb the impact energy under dynamic loading conditions [42]. Whereas, metal lattice structures fabricated by SLM had more topology types than open-cell foams, and stretch-dominated lattices were manufactured besides bending-dominated ones [43]. Compared to bending-dominated structures, the stretch-dominated ones have the lager stiffness in tension or compression conditions.

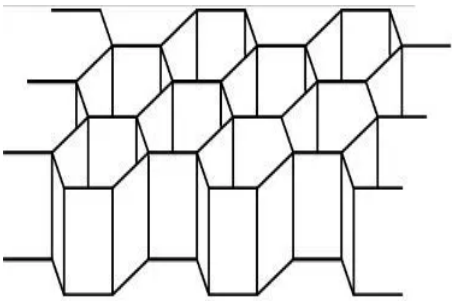

(a)

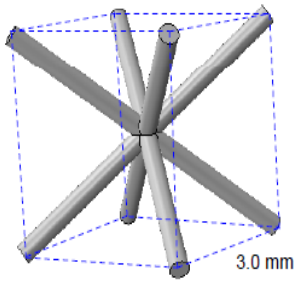

(b)

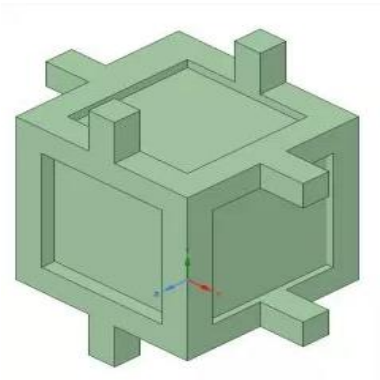

(c)

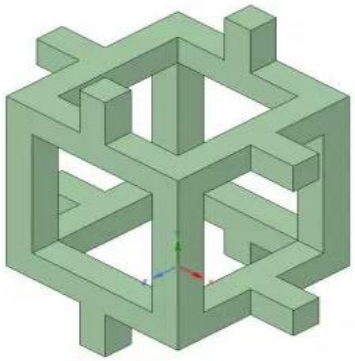

(d)

Figure 2.9. (a) Prismatic honeycomb structure [41], (b) a representative lattice structure: BCC unit cell [42], (c) closed-cell foam unit cell [41], and (4) open-cell foam unit cell [41]

Since the birth of metal 3D printing, the availability of fabricating complex lattice structures has attracted much attention, and more and more different kinds of lattice structures have been designed and manufactured by metal 3D printing. Ullah et al. [44] employed the SLM system to fabricate bio-inspired Kagome truss core sandwich structures. The design of Kagome lattice was inspired from the rod-like internal structure of cancellous bones. The corresponding CAD drawings of a Kagome lattice unit cell is shown in Figure 2.10. Compared to conventional honeycomb core structures, the Kagome lattice core structures show the larger compression and shear strength. The distinct drawback of Kagome lattice structure is that it can only be used to manufacture

sandwich panels with single-layered cores, and the unit cell keeps a certain distance between each other in a layer owing to its specific spatial distribution of struts.

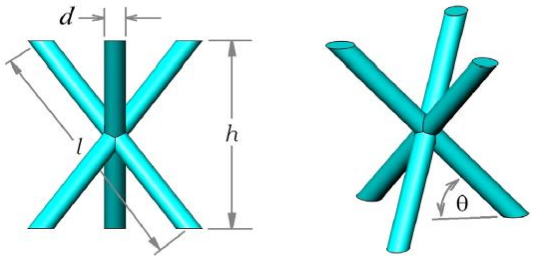

Figure 2.10. A Kagome lattice unit cell with design parameters of diameter, strut length, cell height and internal angle [44]

Smith et al. [45] designed two simple lattice structures: a BCC structure and a similar structure with vertical pillars (BCC-Z), their unit cells are as shown in Figure 2.11. Smith used Finite element (FE) models to predict compressive responses of BCC and BCC-Z structures under quasi-static compressive loads. After the numerical modelling and experimental validation, he concluded that BCC and BCC-Z are outstanding lightweight energy-absorbing structures, and the stiffness and yield strength of them could be improved by optimizing the unit cell dimensions.

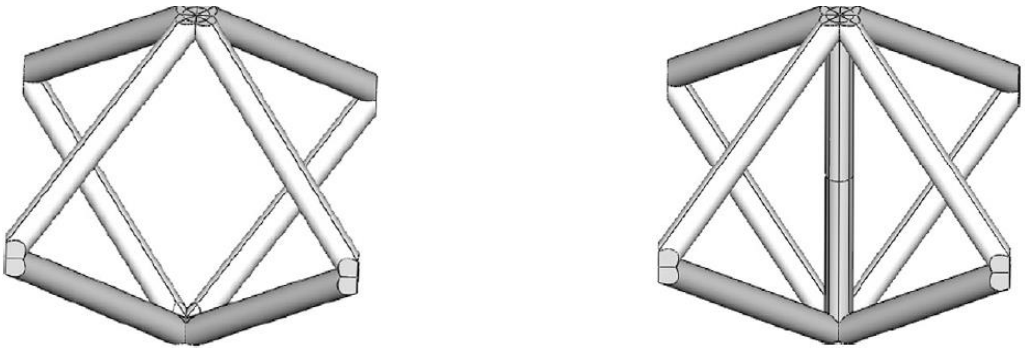

(a) (b)

Figure 2.11. Unit cell topologies: (a) the BCC unit cell, and (b) the BCC-Z unit cell [45]

Leary et al. [43] designed and fabricated a FCC structure to compare its collapse mode with BCC structure. Although the ultimate compression strength of BCC structure was larger than that of FCC structure, FCC structure showed the stable crushing behavior and excellent energy absorption characteristics. The FCC unit cell is shown in Figure 2.12, Leary distinguished BCC structure with FCC structure by strut inclination angles: 35.3° in the BCC structure, and 45° in the FCC structure.

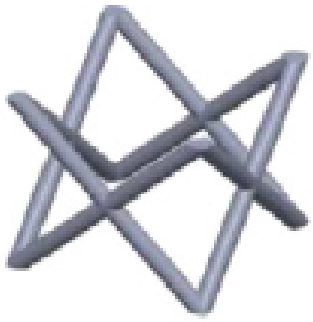

Figure 2.12. Schematic of FCC unit cell [43]

Queheillalt et al. [46] fabricated a one-layer cored sandwich panel by SLM, and the topology of the core was a pyramidal lattice structure. Figure 2.13 shows the schematic of a pyramidal lattice core sandwich structure. As the name suggests, the pyramidal lattice unit cell consisting of four struts looks like a pyramid. The biggest advantage of pyramidal lattice structures is that there are no nodal failures being generated in static and dynamic tests.

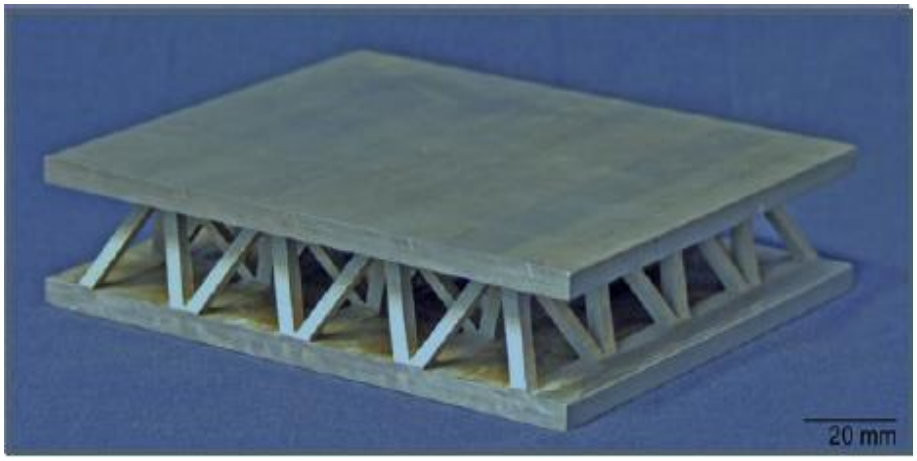

Figure 2.13. Schematic of a pyramidal lattice sandwich panel [46]

Fuller et al. [47] proposed the framework of an octet-truss lattice structure in 1961, and he found out the strength of octet-truss lattice structure was far greater than any materials according to conventional force and strength formulae. Fuller focused on the applications of octet-truss lattice in the construction industry, he suggested octet-truss lattice structures could be used as roof-wall, wall-floor, and roof-wall-floor combination frameworks. Dong et al. [48] described the framework of octet-truss lattice structure in detail. As shown in Figure 2.14, the nodes of octet-truss lattice unit cell form a face centered cubic structure, and the structure has a high nodal connectivity of 12, which defines it as a stretch-dominated structure.

At present, lattice structures are widely manufactured by commercial SLM systems as cores of sandwich structures in aircraft, defense, and construction industries. As their mechanical properties have been well documented, it is necessary to investigate their thermal performance under different working environments.

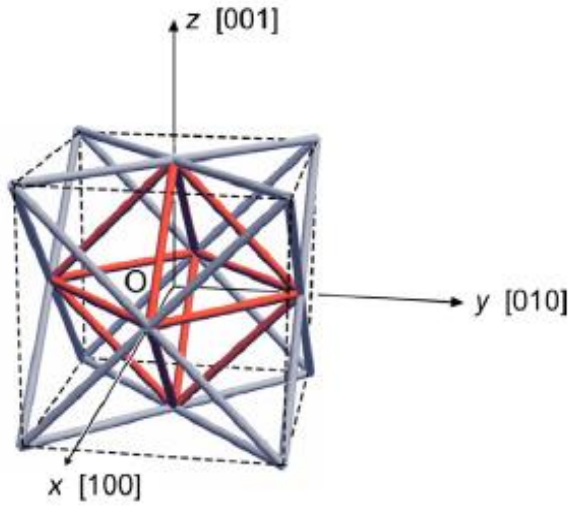

Figure 2.14. Schematic of octet-truss lattice unit cell [48]

2.4. Heat Transfer of Cellular Structures

High porosity, ultra-lightweight, metal cellular structures with the open cell topology emerged in the past decades as attractive heat exchange media for a wide range of applications [49]. As one kind of cellular structures, it can be inferred that some types of lattice structures are also able to be employed as heat exchangers. However, there are few studies related to investigate thermal performances of lattice structures. In this condition, this section will summarize the past research studies exploring heat transfer of cellular structures. They will be used as references for further studies to investigate thermal properties of different lattice structures.

2.4.1 Parameter Study of Cellular Structures

Different from the classification method proposed by Bhate, Evans et al. [50] classified cellular structures into two types according to the regularity and repeatability of the unit cell: one with periodic cells, and the other one with stochastic cellular metals. In the past decades, many researchers have designed and conducted a series experiments to study

thermal properties of different cellular structures and to find out factors having impacts on thermal performances.

Tian et al. [51] used the sandwich panels with two different periodic textile cores as shown in Figure 2.15. to study their thermal performances in forced convection experiments. Finally, he concluded that the amount of heat transferred was determined by the solid conductivity, porosity and surface area density. Moreover, he found out the flow friction factor of wire-screen meshed structure was mainly affected by the open area ratio in flow direction.

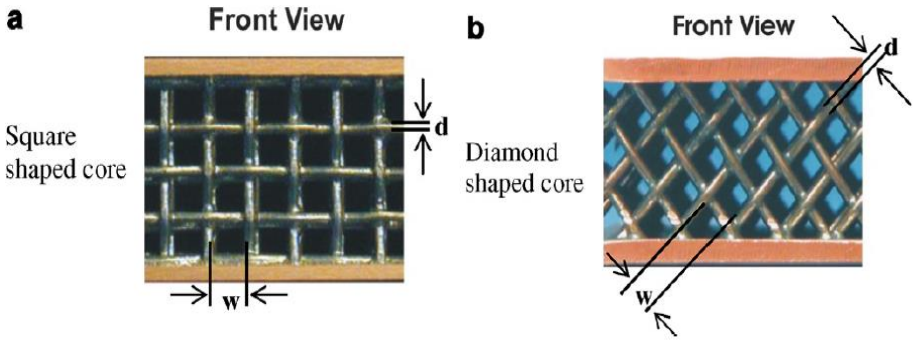

Figure 2.15. Images of two textile laminate heat exchangers: (a) square-shaped pores, and (b) diamond-shaped pores [51]

Gu et al. [52] explored the heat transfer in honeycomb core sandwich panels by varying cell morphologies and cell arrangements. In their studies, two dimensionless indices were introduced to identify the optimal cell shape and arrangement in convective cooling: the first one depends on the ratio of overall heat transfer coefficient to pumping power, and the other one was used to combine thermal performances with shear stiffness. Their research was beneficial for getting a trade-off between heat dissipation and load capacity.

Kim and Lu [49] compared several commonly-used periodic cellular structures as shown in Figure 2.16 to identify the preferable strut orientations for maximizing the heat

dissipation capability. In their investigations, the overall heat transferred was tested under steady-state forced air convection conditions. According to a series of experiments, they demonstrated the heat transfer across cores of sandwich panels was controlled by the porosity and surface area density if Reynolds number was given. In addition, the thermal efficiency of regular textile structures was as good as stochastic metal foams at a lower pumping power.

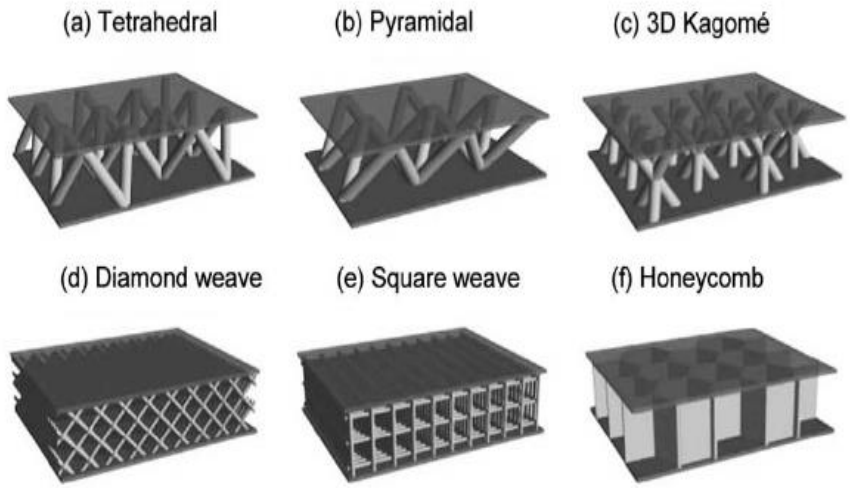

Figure 2.16. Topologies of several periodic structures [49]

Jiang et al. [53] used air and water as coolants to investigate the effect of plate-channel contacts sintering conditions (sintered or non-sintered) on the convection heat transfer. They found out the intensity of convection heat transfer in the sintered porous plate channel was much larger than that in non-sintered one due to reduced thermal resistances at nodes. Their studies showed that sintering could significantly increase transfer coefficient: up to 15 times for water and 30 times for air.

The review above discussed thermal characteristics of cellular structures with periodic cells, foamed metals are also popular in a wide range of thermal applications. Boomsma et al. [54] manufactured heat exchangers by compressing and fashioning open-celled

aluminum foams, then he conducted water forced convection experiments to validate that the generated thermal resistance of open-celled aluminum foamed heat exchangers was about three times lower than the best commercially available heat exchanger tested, when the same pumping power was given, as shown in Figure 2.17.

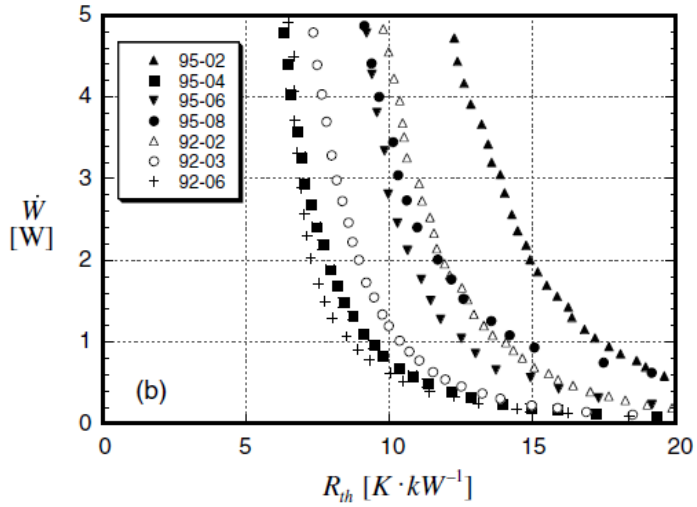

Figure 2.17. Plot of the required pumping power against thermal resistance [54]

Hwang et al. [55] investigated the combining effect of porosity and flow Reynolds number in a duct filled with aluminum metal foams as subjected to air forced convection. The focus of their research was to measure the interstitial heat transfer by applying a transient single-blow technique with a thermal non-equilibrium two-equation model. According to the coincident volumetric heat transfer coefficient achieved by experiments and numerical simulation, the foams-filling duct of 80% porosity appeared the best thermal performance under a constant pumping power because it accomplished a relative high level heat transfer and was accompanied by a moderate pressure drop at the same time.

Hutter et al. [56] investigated the effect of pore size on pseudo-convective heat transfer by varying the ligament diameters of metal foams inserting to empty tubes, and they ascribed the changing of heat transfer to turbulent kinetic energy induced.

It is noticeable that forced convection experiments were usually employed for studying thermal properties of metal cellular structures. In this condition, it is important to investigate properties of flow fluids. Hunt et al. [57] found out that the dispersive transport would generate when fluid moved past the solid particles in fibrous media, and this non-Darcian phenomenon strengthened the heat transfer significantly. They concluded that the thermal dispersion could be ignored when air was chosen as the flow media. However, it was necessary to consider additional contributions when the coolant was water or other fluids due to their higher thermal capacities. As numerical models and experimental data showed, the dispersion conductivity was strongly related to the coolant properties, local flow velocity and porosity [51].

2.4.2 Thermal Conductivity Predictions

Analytical models were effective to predict thermal conductivity values of multi-phase materials [58]. Moreover, the analytical modelling can be used as the preliminary step for the further numerical modelling.

The multi-phase material can be seen as a mixture of solid-phase and fluid-phase materials, and it is always used the classic analytical model for predicting the effective thermal conductivity of cellular structures immersed with fluid. In these analytical models, the porosity of and the thermal conductivity of composition materials determine the effective thermal conductivity of the composite multi-phase materials.

Series model and parallel model were introduced by Gu et al. [59] to simplify the internal structure of the porous graphite foam. Figure 2.18 shows the schematics of

series model and parallel model. In these models, the multi-phase material is considered made up of transversally equally placed solid and fluid layers, the solid and fluid layers are placed alternatively along the heat conduction direction. Eq. (2.3) shows the effective thermal conductivity of the multi-phase materials in the series model.

(a) (b)

Figure 2.18. (a) Series model, and (b) Parallel model [60]

$$\lambda_{eff} = \frac{\lambda_s}{(1-\varepsilon)\frac{\lambda_s}{\lambda_f}+\varepsilon} = \frac{1}{\frac{1-\varepsilon}{\lambda_f}+\frac{\varepsilon}{\lambda_s}} \tag{2.3}$$

where λ_{eff} is the effective thermal conductivity, ε is the porosity, λ_f is the thermal conductivity of the fluid phase materials, and λ_s is the thermal conductivity of the solid phase materials.The series model is used to estimate the minimum value of the possible effective thermal conductivity values of the multi-phase materials.

Contrast to the series model, the parallel model is used to calculate the maximum value of the possible effective thermal conductivity values, in which the solid or fluid layers were considered parallel to the main heat conduction. Eq. (2.4) shows the effective thermal conductivity of the multi-phase materials in the parallel model.

$$\lambda_{eff} = \varepsilon\lambda_f + (1-\varepsilon)\lambda_s \tag{2.4}$$

Yu et al. [61] proposed a square bar model, as shown in Figure 2.19, which a combines the series model and parallel model. In the model, The fluid phase materials were used to fill in the space between cubic cell shaped solid phase materials. In the square bar model, the effective thermal conductivity of the composite multi-phase materials is shown in Eq. (2.5).

$$\lambda_{eff} = (1 - 2t - 2t^2)\left(\frac{\left(\frac{1}{t}-1\right)^2+\sigma}{\left(\frac{1}{t}-1\right)^2+1}\right)\lambda_f + \frac{2t(1-t)}{(1-t)\sigma+t}\lambda_s \qquad (2.5)$$

where

$t = \frac{a}{H/2}$, $\sigma = \lambda_s / \lambda_f$, a is the square bar size, and H is the unit cell length.

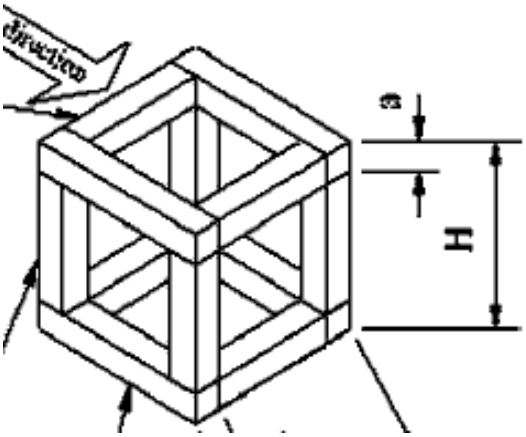

Figure 2.19. Square bar model [61]

In order to calculate the conductivity of an isotropic foam accurately, Leach et al. [62] proposed cubic cell models including cubic-series-parallel (CSP) model and cubic-parallel-series (CPS) model. Figure 2.20 shows the schematics of them respectively.

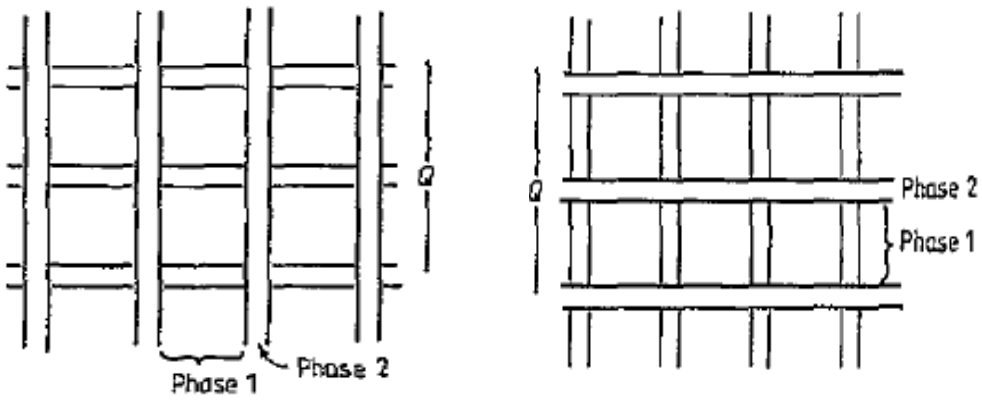

(a) (b)

Figure 2.20.(a) CSP model, and (b) CPS model [62]

The thermal conductivity values predicted by CSP and CPS models are shown in Eq. (2.6) and Eq. (2.7) separately.

$$\lambda_{eff} = \lambda_s \left(1 - \varepsilon^{\frac{2}{3}}\right) + \frac{\lambda_s \varepsilon^{\frac{2}{3}}}{\lambda_f + (\lambda_s - \lambda_f)\varepsilon^{\frac{1}{3}}} \tag{2.6}$$

$$\lambda_{eff} = \lambda_s \frac{\lambda_s - (\lambda_s - \lambda_f)\varepsilon^{\frac{2}{3}}}{\lambda_s - (\lambda_s - \lambda_f)\left(\varepsilon^{\frac{2}{3}} - \varepsilon\right)} \tag{2.7}$$

The analytical models summarized above focus on investigating the relationship between the effective thermal conductivity and porosity regardless of structure topology. In reality, the thermal conductivity values of different structures should be investigated for better control ad utilization of porous structure as heat exchange media.

2.4.3 Convective heat transfer models of cellular structures

In order to evaluate convective heat transfer performance of different cellular structures, the flow friction factor, Nusselt number and heat transfer rate are the main indices. For easier attaining the thermal properties without trouble work, a lot of researchers have been trying to build up suitable analytical and numerical models to predict evaluation

the relevant indices and simulate the convective heat transfer processes. When being applied to study the forced air convection, a fin analogy model was demonstrated effective to characterize heat transfer performance of different cellular structures, such as textile laminates [51], open-celled metal foams [63], metal honeycombs [64], and lattice-frame materials [65], as shown in Figure 2.21.

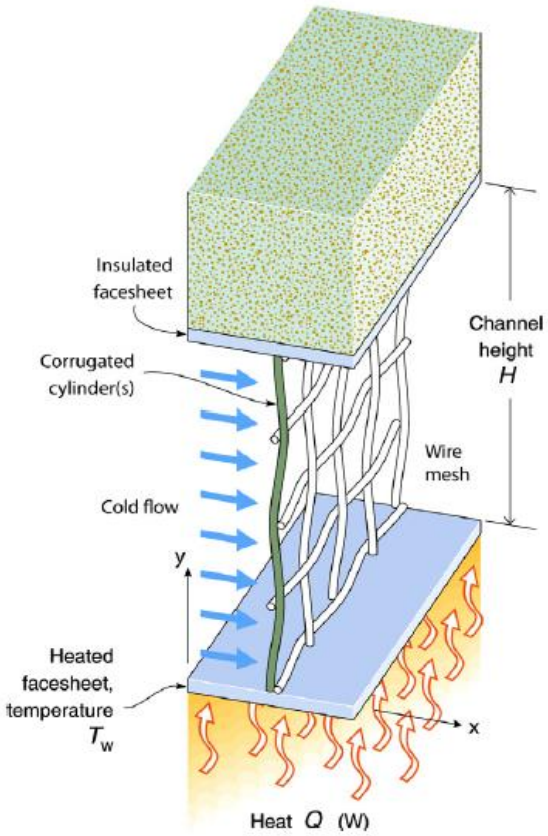

Figure 2.21. Single corrugated cylinder of a single mesh [51]

Based on the fin analogy model theory, Kim et al. [66] applied the square root of Darcy number (*Da*) to obtain a Nusselt number (*Nu*) correlation of aluminum foams. As shown in Figure 2.22, the data of Nusselt number have been converted to dimensionless parameters, so that the data merge to a single line in log-log plot. According to their research, an empirical Nusselt number correlation could be used to predict convective heat transfer characteristics of aluminum foams.

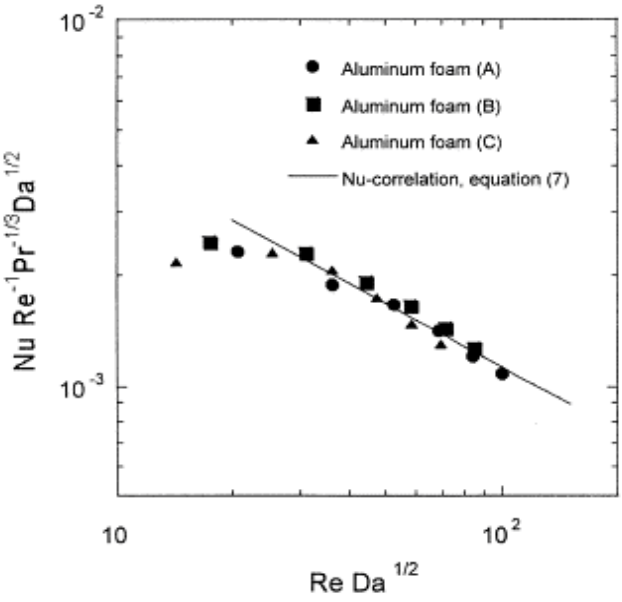

Figure 2.22. Modified Nusselt numbers of aluminum foams [66]

Yan et al. [67] conducted a series of experiments to obtain a function of the mean velocity over the channel height when studying the convective heat transfer in a metallic X-lattice cored sandwich panel, then applied it to calculate the local bulk mean fluid temperature over flow direction in energy balance equation. Figure 2.23 shows the details of fluid flow characteristics of X-lattice structures when subjected to air convective cooling.

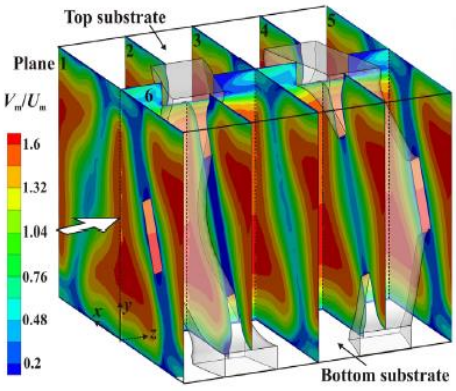

Figure 2.23. Velocity contours in several representative cross-sections respectively [67]

Lin et al. [68] compared two major simulation models to analyze thermal performances of porous media when subjected to fluid convection: local thermal equilibrium (LTE)

model and local thermal non-equilibrium (LTNE) model, finally he concluded LTE model was also useful when applied at high flow velocities.

In all, convective heat transfer characteristics of cellular structures are strongly affected by the structure topology. Topology is a very broad concept which consists of types and dimensions of the structure. Using previous studies as references, the most important parameters of cellular structures should be considered in thermal analysis are relative density, pore fraction, surface area density, and open ratio. As one kind of cellular structures, these reference resources are beneficial to further study convective performances of lattice structures.

2.5. The development of conformal cooling channels

Plastic injection is one of the most affordable and broad processes for mass production purposes in the industry [69,70]. It has four main steps that are (in a sequence) i) melt plastic injection, ii) packing in the mold, iii) cooling process and iv) ejection from the mold [71]. The total consumed time during these steps is called total cyclic time whilst the cooling step shares 70% to 80% of the total cyclic time [72]. As insufficient or low-quality cooling can result in negative impacts on the product quality like unwanted warpage and shrinkage, two critical parameters including cooling time and temperature uniformity on the mold surface are used to manage the cooling process well: The decrease of cooling time is the desired point for performance improvement, however, the uneven cooling contributes to the different residual stress distribution among the plastic surface, then resulted in warpage. Therefore, the decrease of cooling time should be controlled with the temperature distribution on the mold surface that is called temperature uniformity.

The cooling performance can be improved via two factors that are the mold material properties and the cooling application [73]. Between these two factors, the cooling application is preferable because the mold material properties are mostly decided according to the mechanical properties like strength, weight, etc. rather than considering the thermal conductivity value. Traditional mold cooling involves drilling straight channels in the mold geometry. They are easy-to-fabricate, economically feasible, but also very basic that can result in an insufficient cooling process, especially for the complex plastic product geometries. To improve the cooling performance of traditional straight-drilled channels, optimum cooling parameters like channel spacing, channel diameter, flow rate, and thermal properties of the circulated coolant through the channel can be used [74,75]. Nevertheless, the mentioned improvement approaches can be still insufficient for the complex plastic products due to the design limitations of the channels and traditional machining.

Differently from the traditional machining tools, 3D printing technology can be effectively used in the plastic injection mold processes to improve the cooling performance significantly [76]. By means of the design and manufacturing flexibility of 3D printing tools [77,78], cooling channels can follow the complex contours of the plastic product in the mold geometry; hereby, they are named conformal cooling channels (CCCs). Compared to traditional channels, CCCs achieve a shorter cooling time that was found in the wide range of 15%-50% with reference to Refs. [79-81]. Beard [82] approximately calculated the profit income increment in the range of 27%-55% corresponding to the decrement of cooling time by 20%-40%. Dimla et al. [83] found that the product improvement rate can reach up to 70% when the CCCs are considered in the injection molding process. However, as mentioned above, temperature uniformity is also a crucial factor and these two factors (cooling time and temperature

uniformity) do not always go in parallel with each other because uncontrolled short cooling time may result in temperature non-uniformity. Also, due to the complex channel pathways in the mold, the pressure drop values of the circulated coolant becomes higher than the obtained pressure drops in traditional channels, which cause extra pump consumption and decrease the energy efficiency of the plastic injection molding process. Thus, the design and optimization of CCCs are crucial steps before implementing in a real environment.

Up to now, there have been various CCC applications for the plastic injection molding process. Different cross-sectional profiles are popular research motivations in the CCC development studies. Among different cross-sectional profiles, circular CCCs are generally the first-considered ones due to their simplicity. In Ref. [84], the CCC design was presented with the cross-sectional profile alternatives of circular, trapezoid, and rectangular for liquid cooling purposes in a battery pack. Besides the profile type, number of CCCs, the diameter of CCCs, the distance between CCC and mold surface were investigated. The use of CCCs improved the cooling performance up to 39% while the product performance (shrinkage, warpage, etc.) was enhanced by nearly 5%. Saifullah and Masood [85] focused on the decrease of the total cyclic time of a plastic canister model in the plastic injection molding process. Comparing the traditional and conformal cooling channels, which both had circular cross-sectional profiles, it was seen that the CCCs reduced the totally cyclic time by up to 35% whilst the maximum temperature on the mold surface was decreased by nearly 30%. Following that study, Saifullah et al. [86] considered the same plastic model and improved the cooling time by 37.5% using the high-conductive copper-supported bi-metallic conformal cooling channels. Mazur et al. [87] performed a spiral pathway for the CCC design, which was not possible with traditional machining. The comparative study inferred that the spiral

CCC provided 5 K lower ejection temperature that is an improvement sign from the standpoints of shrinkage and warpage. Schmidt et al. [88] conducted the CCC solution in two different mold material types: P-20 steel and 420 SS/bronze. The use of CCCs improved the cooling time by 32.7 and 19.8% whilst the corresponding shrinkage was decreased by 28.2% and 15.1% for P-20 steel and 420 SS/bronze, respectively. For more detailed examples of CCC applications and comparative analyses between traditional channels and CCCs, previously published review works [71,72,89] can be referred to.

The aforementioned studies emphasize the importance of CCCs in the cooling step of the plastic injection mold process. It is also seen that each plastic product model has its own limitations so that the CCC design should be considered unique for each plastic product model. According to the product properties (e.g. polymer material properties, contours of plastic product-which affect the mold geometry-, injection & ejection temperature), CCCs may have different constraints. That is, the CCC application is a complex procedure from the initial design to the final printing process of the mold geometry. Even though the above-given literature works and relevant review papers present useful insights, there are still research gaps for a better understanding of CCC applications.

2.6. Summary

This chapter first introduces the metal 3D printing technology in detail. Then, the flow process and process parameters of the best performance to cost ratio methods SLM and its transformed version DMLS are narrated clearly. In addition, the potential of SLM for manufacturing complex-shaped lattice structures is previewed.

Lattice structures are promising for thermal management as heat exchange media due to their porous and controllable geometric characteristics, while the potential of 3D

printing for manufacturing thermally used lattice structures has not been explored. Therefore, for investigating lattice structure properties, too much attention was paid on the mechanical properties, but few researchers studied their thermal properties. In this condition, the corresponding studies on porous structures are summarized in this chapter for investigating the conductive and forced convective heat transfer performance of lattice structures. Firstly, analytical models used to predict the effective thermal conductivity are listed for further studying the heat conduction properties of lattice structure-fluid composites. Subsequently, heat transfer models used to study fluid and thermal characteristics of cellular structures under the forced convection conditions are reviewed.

At the end, the development of CCCs in the plastic injection molding industry is studied. In the past, the integration of lattice structures aimed at increasing the mechanical performance of CCCs, while the advantage of lattice structures used as heat exchange media has not been utilized. It can be seen that the effect of channel topology design affects the cooling performance of CCCs significantly, which provides the opportunities for the lattice structure to enhance the cooling performance in CCCs. Besides, it is also summarized that the best CCCs design should meet three requirements of minimum cooling time, minimum surface temperature nonuniformity, and minimum pressure drop through the channel. In industry, the satisfying design should be a compromise between these requirements.

Chapter 3. Design and Fabrication of Test Samples for Conduction and Forced Convection Investigations

3.1. Introduction

In the study of heat conduction and forced convection, SLM methodology was used to fabricate aluminum alloyed AlSi10Mg multi-layered lattice structures, in which component struts form identical, repeated, and continuous cubic unit cells. Sandwich panels with BCC, FCC-XY, FCC-Z, and octet-truss lattice structure cores were designed and fabricated for studying the effect of structure geometry, porosity, specific surface area, and the cross-section area of the solid phase material along the main heat conduction direction, on the heat conduction performance. Four long sandwich panels composed of the same porosity BCC, FCC-XY, FCC-Z, and octet-truss lattice structures were also manufactured by the same SLM process parameters, which were used for studying the hydraulic and heat transfer characteristics of different lattice structures in forced convection investigations.

3.2. Geometric characteristics of lattice structure unit cell

As lattice structure is always made up of several repeated unit cells, its geometric features depend on the unit cell topology. The unit cell performs the porous structure characteristics, in which the topology is determined by porosity, pore density, and component strut location. Porosity is defined as the ratio of void volume to the unit cell total volume. For a specific lattice structure, the porosity is controlled by the strut size and unit cell length. Either enlarging the strut size or decreasing the unit cell length contributes to the larger volume of solid-phase materials and the smaller porosity. Pore

density indicates the number of pores along a random two-dimensional (2D) line and is always quantified by pores per inch (PPI). In the present study, the number of pores along a 2D scaled length equals the number of unit cells under the same space. In a given length, the pore density is inversely proportional to unit cell length. The component strut location is the largest topology difference between different types of lattice structures and also determines the physical properties.

Figure 3.1 shows a group of unit cells used in this study, and they share the same unit cell length of 6 mm. In the BCC unit cell, the central axis of each cylindrical strut is the diagonal of the cubic cell. In the FCC unit cell, the strut centre axes are the diagonals of middle planes parallel to Plane *YZ* and Plane *XZ*. The octet-truss lattice structure unit cell is an enhanced version of FCC, in which the struts are generated in the planes parallel to Plane *YZ*, Plane *XZ*, and Plane *XY*, therefore its nodal connectivity increases from eight to 12 when compared to BCC or FCC.

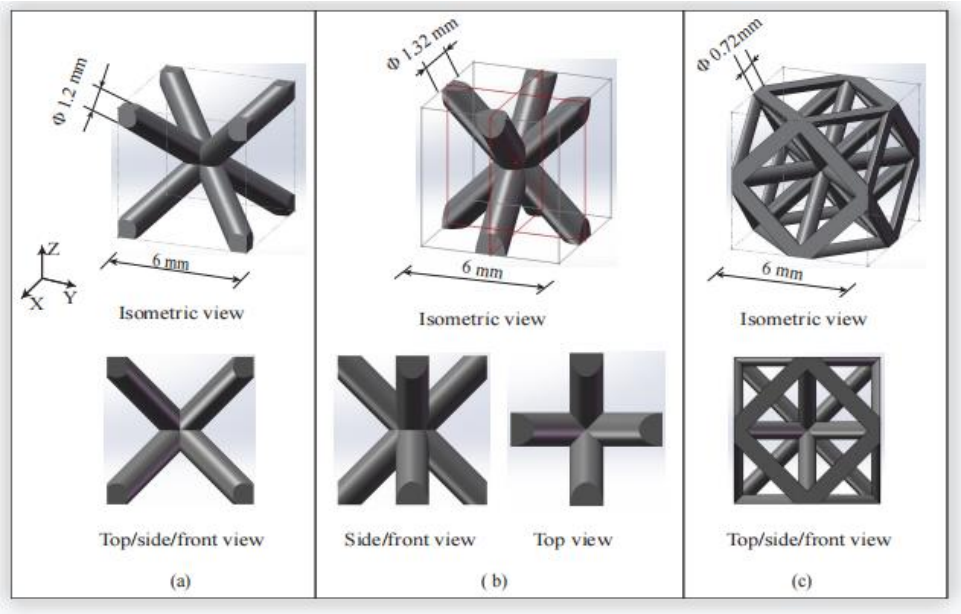

Figure 3.1. Unit cell geometry of (a) BCC, (b) FCC, and (c) octet-truss lattice structure

It is also found that for BCC and octet-truss lattice structure unit cells, 2D geometries from the top view, side view, and front view are the same, therefore the heat transfer and hydraulic performance both perform the same from the axis of *x*, *y*, and *z*. For FCC unit cell, the top view geometry is different from the ones from the side view and front view, which contributes to two different patterns of thermal and hydraulic properties. In this study, the FCC lattice structure is defined as FCC-Z when investigating the properties along the axis of z and defined as FCC-XY when the properties along the axis of *x* or *y* are studied.

3.3 Test samples for investigations

In the present study, the commercial SLM system SLM 250HL (SLM Solutions GmbH) at SC3DP was used to fabricate test samples for conduction and forced convection investigations. The SLM manufacturing process follows up two principles: fabricating samples layer by layer, and employing a high-power focused laser to melt metallic powders. The laser used in the SLM 250HL machine is a Gaussian distributed YLR-Faser laser with the maximum power of 400 W. As the densification of feedstock powders is mainly affected by the laser system setting, it is important to set the corresponding parameters appropriately based on raw material properties. In this study, spherical aluminum alloyed AlSi10Mg powders (EOS GmbH) ranging from 20 μm to 63 μm were used as raw materials for the lightweight characteristic and relatively high thermal conductivity of 103-183 W/m·K [78], which meet the industrial requirement of manufacturing porous structures with the satisfying heat transfer capability. Table 3.1 shows specific chemical compositions of AlSi10Mg powders used in this study. Except for aluminum, the silicone takes up around 10% weight for decreasing the general thermo-coefficient [90]. For fabricating AlSi10Mg test samples used in conduction and

forced convection investigations, the laser system parameters including the power of 280 W, the scan rate of 1150 mm/s, the scan spacing of 170 μm, and the layer thickness of 50 μm were set in this study.

Table 3.1. Alloying elements in AlSi10Mg powders [90]

Composition	Al	Si	Mg	Fe	Mn	Ti	Zn	Etc.
Weight percentage (%)	balance	9-11	0.2-0.45	≤ 0.55	≤ 0.45	≤ 0.15	≤ 0.1	

Laser scanning pattern also needs to be determined in the laser system setting. Dewidar et al. [92] discovered that standard and diagonal scan strategies contribute to better densification results than others. These two scan patterns both employ a high-power focused laser beam to scan the perimeter of the required cross-section area first. As illustrated in Figure 3.2, the difference between standard and diagonal strategies is the way they follow to scan the internal area. In the standard scanning pattern, all scan paths are parallel to the *x* or *y* axis of building platform. In the diagonal scanning pattern, each path keeps a constant angle of 45° to the axis of *x* or *y*. In this study, the diagonal scanning pattern was employed to fabricate test samples for conduction and forced convection investigations. In order to minimize combustion and oxidation of powders during the laser scanning, The SLM manufacturing process was conducted in a sealed building chamber where the oxygen percentage was always smaller than 0.2% by keeping flushing inert argon gas into it until the construction job ended.

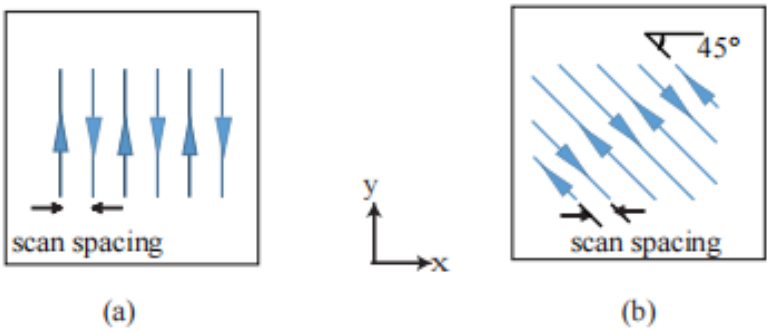

Figure 3.2. (a) The standard scan strategy, and (b) the diagonal scan strategy

The inter-solid porosity is the most important indicator to check whether the setting of laser system parameters results in satisfying densification. In this study, the confocal microscopy DCM8 (Leica Microsystems GmbH) was used to scan the slice cut from the solid AlSi10Mg block fabricated by the above-listed laser system parameters. As shown in Figure 3.3, the area of pores is smaller than 5% of the view, which demonstrates the effectiveness of laser system parameter setting.

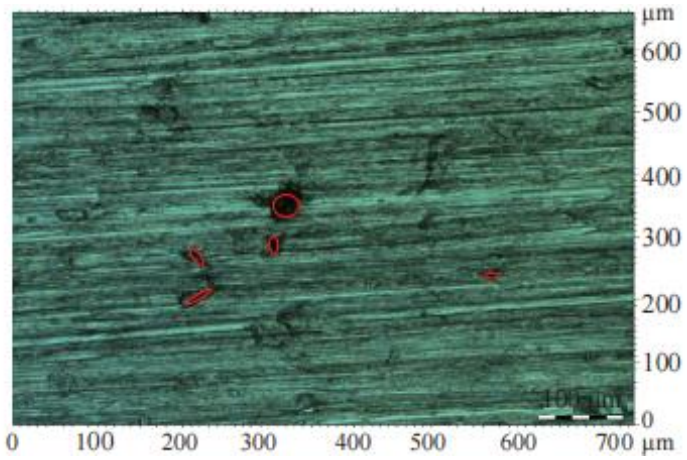

Figure 3.3. Micrograph of AlSi10Mg slice

3.3.1 Test samples for conduction investigations

For the heat conduction investigations, sandwich panels containing BCC, FCC-Z, FCC-XY, or octet-truss lattice structure cores were fabricated, as shown in Figure *3.4*. The

bulk dimension of the sandwich panel is 24×24×44 mm^3, in which the core is made up of 64 (4×4×4) lattice structure unit cells with 6 mm unit cell length. The two solid panels adjacent lattice structure core were manufactured for inserting thermocouples along the main heat conduction direction in experiments, to further determine the effective thermal conductivity of multi-layered lattice structure core.

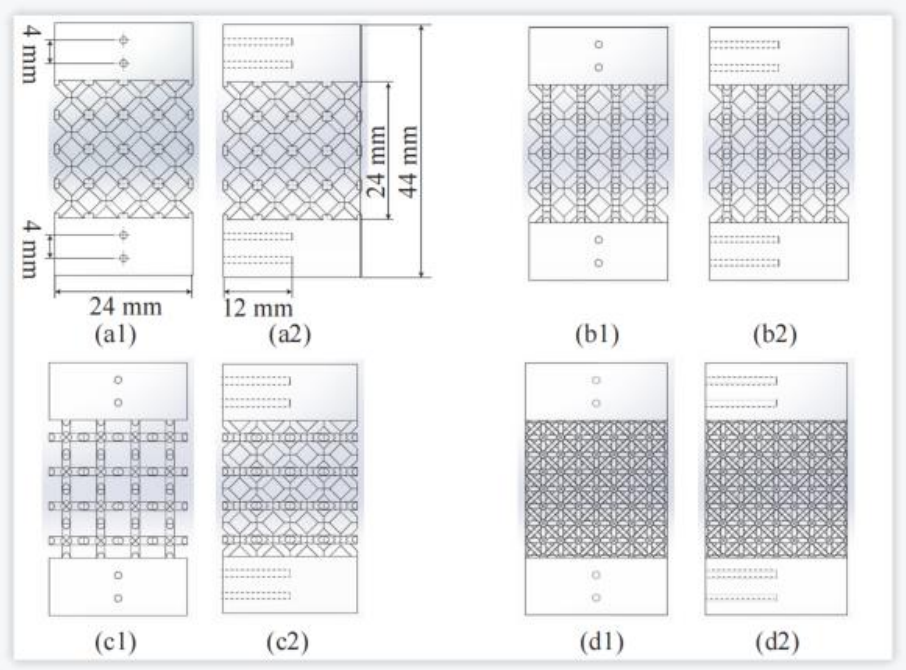

Figure 3.4. 2D views of designed sandwich panels containing: (a1, a2) BCC; (b1, b2) FCC-Z; (c1, c2) FCC-XY; (d1, d2) octet-truss lattice structure.

At the stage of characterizing unit cell geometries, since the unit cell length was fixed as the constant of 6 mm, the component strut size and location were changed to further and fully investigate the conductive heat transfer mechanisms of different lattice structures. The geometric parameters of the SLM fabricated multi-layered lattice structure cores are summarized in Table 3.2. Herein, the specific surface area is defined as the total surface area of lattice structure core divided by the core volume. It can be

seen that this batch of samples was categorized into four groups based on the porosity value. In each group, the heat conduction experiments were conducted on the test samples sharing the same porosity lattice structure cores to investigate the effects of unit cell topology and specific surface area on the conductive heat transfer performance. Besides, for each kind of lattice structure, the porosity decreased at the increment of strut radius value. Therefore, the experimental results also demonstrated the effect of porosity on the heat conduction properties. Figure 3.5 shows the SLM fabricated test samples for the heat conduction investigations, in which the core geometric parameters are consistent with the ones listed in Table 3.2.

In addition to fabricating lattice structures composed of regular cylindrical struts, another three BCC lattice structures consisting of tapered cylindrical struts were designed and manufactured by the SLM 250HL machine. The cross-section of the tapered strut is still a circle, but the radius value varies along the strut centre axis. In this study, the unit cell designs of BCC lattice structures containing tapered struts referred to the geometric parameters of the BCC lattice structure unit cell with 6 mm unit cell length and 0.6 mm strut radius. Table *3.3*. summarizes the detailed core geometric parameters of them. Figure 3.6. shows the topologies of single tapered struts, unit cells, and SLM fabricated samples containing BCC lattice structure cores with tapered struts. It is found that the cores listed in Table 3.3. have the same porosity and very similar specific surface area. The purpose of conducting experiments on them is to validate the effectiveness of a first proposed conception of effective conduction area, which will be elaborated on in the next chapter.

Table 3.2. Geometric parameters of multi-layered lattice structure cores in the heat conduction test samples

Test sample name	Unit cell type	Strut radius (mm)	Specific surface area (mm^2/mm^3)	Porosity
A1	BCC	0.20	10.04	0.98
B1	FCC-Z	0.22	9.13	0.98
C1	FCC-XY	0.22	9.13	0.98
D1	Octet-truss	0.12	21.62	0.98
A2	BCC	0.40	5.04	0.91
B2	FCC-Z	0.45	4.49	0.91
C2	FCC-XY	0.45	4.49	0.91
D2	Octet-truss	0.26	9.77	0.91
A3	BCC	0.60	3.37	0.82
B3	FCC-Z	0.67	3.03	0.82
C3	FCC-XY	0.67	3.03	0.82
D3	Octet-truss	0.36	6.93	0.83
A4	BCC	0.80	2.54	0.71
B4	FCC-Z	0.90	2.28	0.71
C4	FCC-XY	0.90	2.28	0.71
D4	Octet-truss	0.50	4.84	0.72

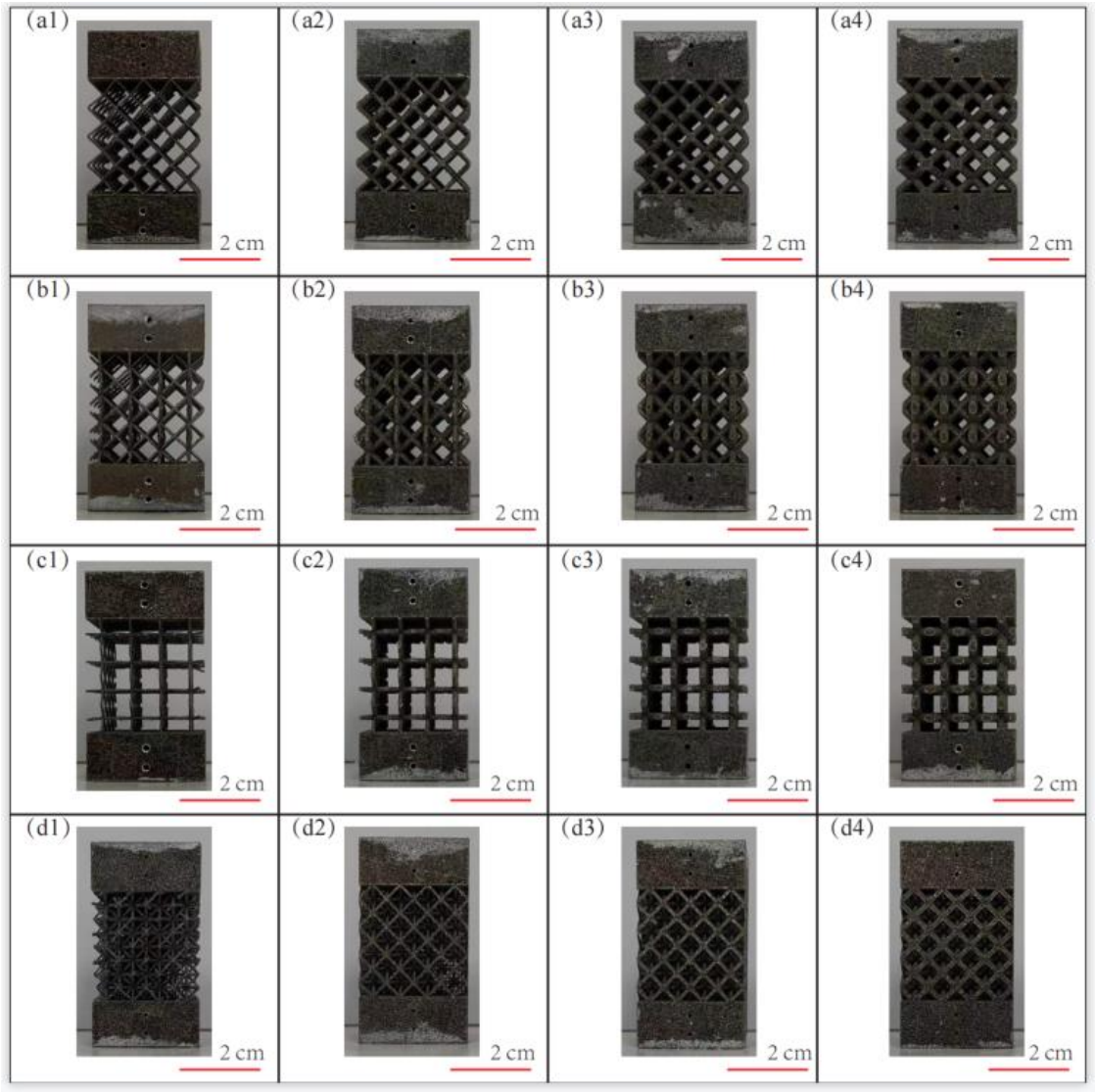

Figure 3.5. SLM processed sandwich panels with multi-layered lattice structure cores (a1-a4) BCC; (b1-b4) FCC-Z; (c1-c4) FCC-XY; (d1-d4) octet-truss. (a1, b1, c1, d1) porosity= 0.98; (a2, b2, c2, d2) porosity= 0.91; (a3, b3, c3, d3) porosity= 0.82; (a4, b4, c4, d4) porosity= 0.71.

Table 3.3. Geometric parameters of BCC lattice structures containing tapered struts

Test sample name	Maximum strut radius (mm)	Minimum strut radius (mm)	Specific surface area (mm^2/mm^3)	Porosity
A3	0.6	0.6	3.37	0.82
A5	0.95	0.2	3.47	0.83
A6	0.8	0.4	3.45	0.82
A7	0.7	0.5	3.47	0.82

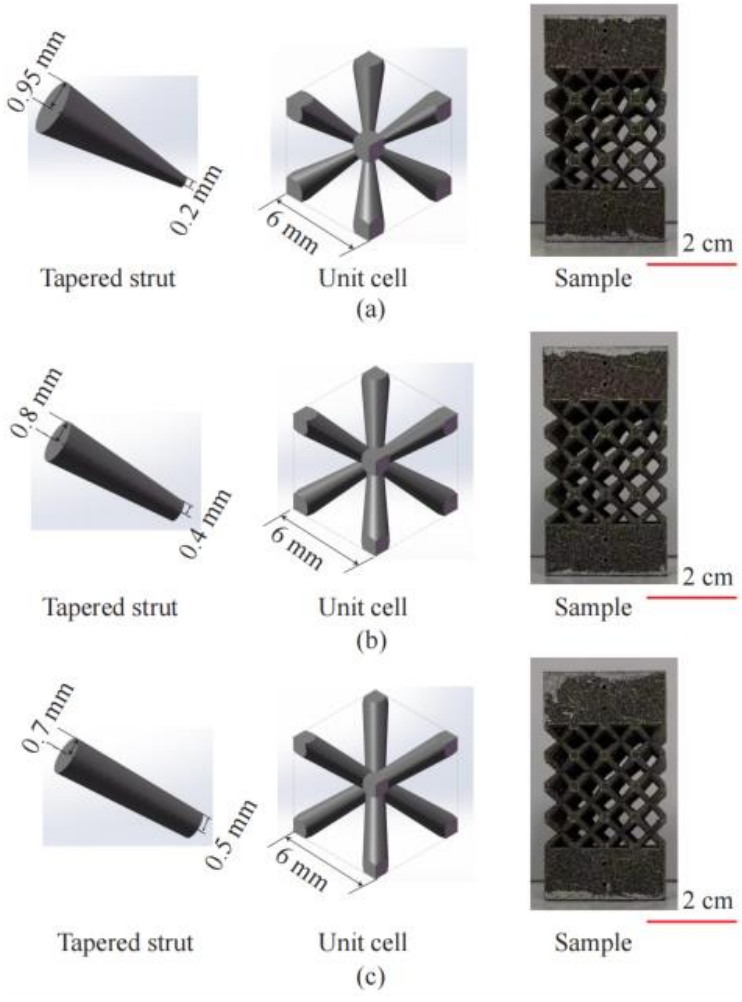

Figure 3.6. Sandwich panels with tapered struts composed BCC lattice structure cores. (a)A5, (b)A6, and (c)A7

3.3.2 Test Samples for Forced Convection Investigations

Four pieces of AlSi10Mg sandwich panels containing the same porosity BCC, FCC-Z, FCC-XY, or octet-truss lattice structure cores were fabricated by the SLM 250HL machine and used as test samples for the forced convection investigations, as shown in Figure 3.7. The bulk dimension of the test sample is $70\times20\times28$ mm^3, and that of the multi-layered lattice structure core is $70\times20\times20$ mm^3. As the unit cell length of the fabricated lattice structures was set as 5 mm, there are 224 ($14\times4\times4$) lattice structure unit cells in the core. As Figure 3.7 shows, four holes with the equal spacing of 14 mm to each other were preserved in the bottom solid panel during the SLM process, used to insert thermocouples for measuring the temperature values along the flow direction in experiments.

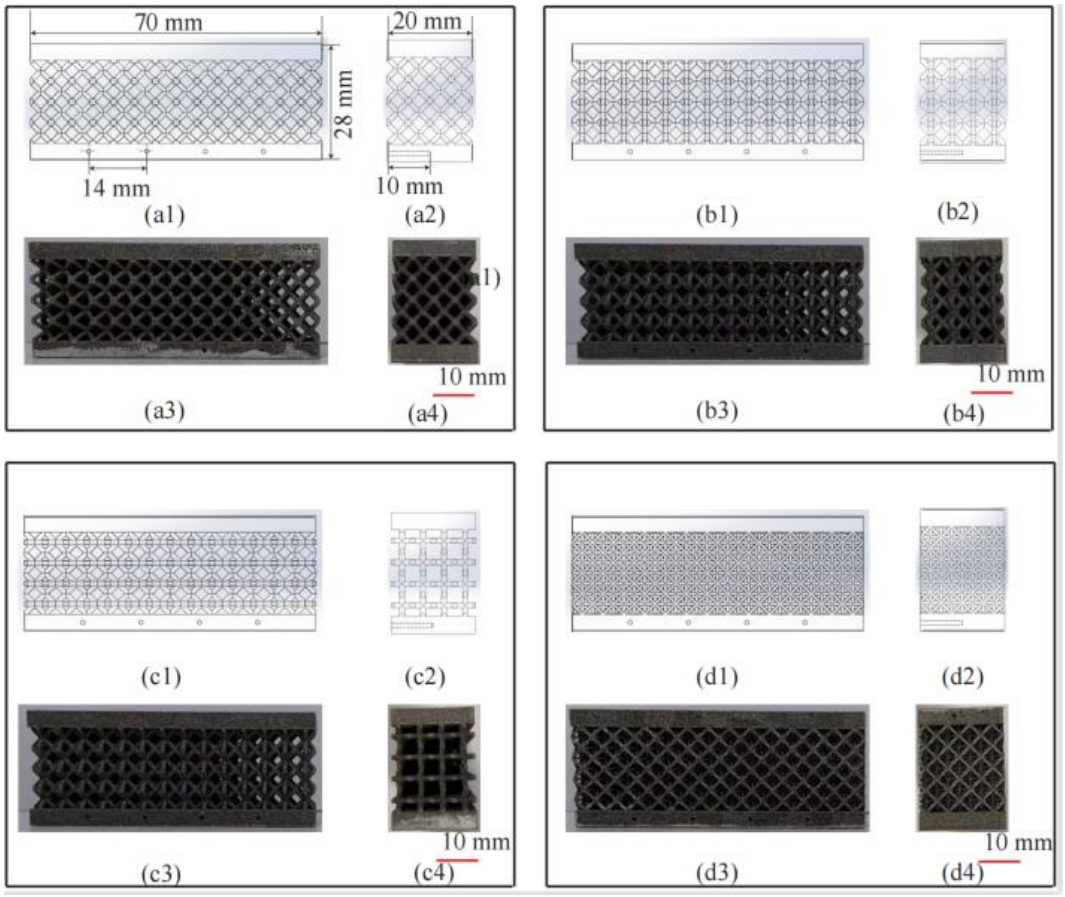

Figure 3.7. Cross-sections of designed and SLM processed samples for forced convection investigations (a1-a4) sample with BCC lattice structure core; (b1-b4) sample with FCC-Z lattice structure core; (c1-c4) sample with FCC-XY lattice structure core; (d1-d4) sample with octet-truss lattice structure core.

Table *3.4*. summarizes geometric parameters of the multi-layered lattice structure cores in the forced convection test samples. Except for porosity and specific surface area, the open area ratio of the core was also summarized, which is defined as the void area in the plane perpendicular to the flow divided by the frontal area of the sample viewed in the direction of flow [37]. The air forced convection experiments were then conducted to these samples for determining hydraulic and convective heat transfer properties of different lattice structures under different air velocity values.

Table 3.4. Geometric parameters of lattice structure cores in convection test samples

Core type	Strut radius (mm)	Specific surface area (mm^2/mm^3)	Porosity	Open area ratio
BCC	0.50	4.05	0.82	0.55
FCC-Z	0.55	3.70	0.83	0.51
FCC-XY	0.55	3.70	0.83	0.61
Octet-truss	0.33	7.63	0.82	0.46

3.4 Summary

This chapter shows the geometry designs and fabrication of test samples for heat conduction and air forced convection experimental investigations. In the SLM process, the laser system parameters were set well to ensure the satisfying densification of aluminum alloyed AlSi10Mg powders. For heat conduction experiments, 16 test samples containing regular cylindrical struts were fabricated and classified into four groups based on the porosity value of the lattice structure core. Besides, another three samples containing tapered struts, and sharing the same porosity and specific surface area of lattice structure core were designed and fabricated. For air forced convection experiments, four long sandwich panels with same porosity but different typed lattice structure cores were manufactured. After the preparation of test samples, the experimental studies on the steady-state heat conduction and the forced convection process of different lattice structures were conducted immediately.

Chapter 4. Conductive heat transfer in selective laser melting processed lattice structures

4.1. Introduction

Effective thermal conductivity is always used to evaluate the structure's conductive heat transfer performance. In this chapter, both experimental and numerical investigations were conducted on the SLM processed sandwich panels containing either BCC, FCC, or octet-truss lattice structure cores, to study the effects of structure geometry, porosity, specific surface area, and the minimum cross-section area perpendicular to the main heat conduction direction, on the effective thermal conductivity. The experimentally validated 3D conjugated heat transfer model illustrated the detailed temperature distributions of different lattice structures under the steady-state conductive heat transfer condition. The model was also used for deriving the value of specific thermal conductivity, a firstly proposed conception for evaluating whether the lattice structure meets the industrial requirements of lightweight characteristic and relatively high effective thermal conductivity at the same time.

4.2. Experiments

4.2.1. Experimental Setup and procedures

A novel experimental setup was designed and assembled to measure the temperature values at specific locations, which were used for deriving the effective thermal conductivity value of the multi-layered lattice structure core. As Figure 4.1 (a) shows, three modules make up the experimental setup, including the heating system, the test

module, and the cooling system. The heating system contains a ceramic heater (Xinnuo Industrial Controls Pte. Ltd.) and a thin copper block with 3 mm thickness. In experiments, the heat was generated from the heater in which the heat flux can be adjusted by changing the output voltage or current value of the power supplier. The purpose of placing a thin copper block on the heater is to guarantee the generated heat was totally and evenly being transferred to the test sample bottom surface. The heat was then transferred throughout the whole test sample in the test module. The test module contains the test sample, the calibrated thermocouples, and the data acquisition (DAQ) system. Figure 4.1 (b) shows the locations of five K-type thermocouples used in the experimental investigations, as well as the locations of the interfaces between panels and the core. The thermocouples were all inserted to the midpoint of the planes perpendicular to the main heat direction, and the measured temperature values (T_1-T_5) were considered as the average temperature value of correspondent planes. The temperature values (T_1 and T_2) measured by the thermocouples inserted into the lower panel were used to determine the temperature value (T_l). of the core lower surface. Similarly, the measured values of T_3 and T_4 were used for deriving the temperature value (T_u) of the core upper surface along the main heat conduction direction. The T_5 value shows the real-time surface temperature value of the copper exchanger in the cooling system. The cooling system consists of a copper exchanger having internal cooling channels, a chiller (Model AP 15R-40, Polyscience Solutions Co., Inc.), and thermally insulated Teflon connecting tubes. In the cooling system, the constant temperature cold water flushed from the chiller into the exchanger, which formed a circulated cooling loop in the internal channels. Hence, the surface temperature value (T_5) of the exchanger was also kept as constant. In experiments, the thermocouple measured values were instantly recorded by the DAQ system unit the test sample reached the thermally steady

state. For minimizing the heat loss in experiments, the test sample was placed in a conformal Teflon (thermal conductivity: 0.25 W/m K) chamber with 2 cm thickness, and the heating system was wrapped by the aerogel whose thermal conductivity is smaller than 0.02 W/m K.

The heat conduction experiments were conducted after assembling all setup modules well in the room temperature of 300 K. In each experiment, the input heat flux on the sample bottom surface was kept as the constant of 3819.44 W/m^2 by fixing the input voltage and current values of the ceramic heater as 4.4 V and 0.5 A separately. Besides, the top surface temperature value was set as 295 K, same as the surface temperature value of the copper exchanger. Throughout the whole experiment process, thermocouple measured instant temperature values were recorded by the DAQ system, and the sampling interval was set as once per second. The experiment ended until the test sample reached the thermally steady state over three minutes. In this study, the steady state was defined as either temperature variation of T_1 to T_5 in one minute is smaller than 0.1 K. In order to eliminate the experiment error, three repeated experiments were conducted on the same sample and under the same operating conditions.

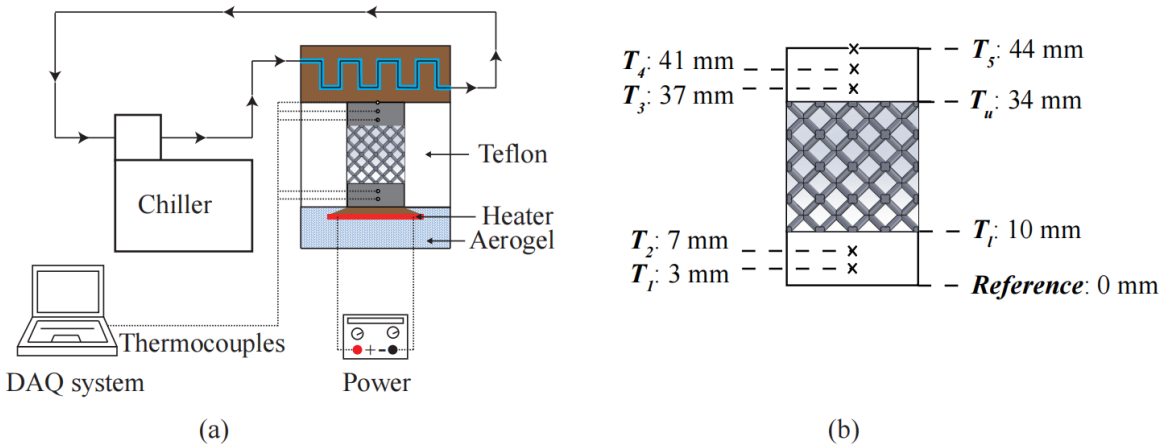

Figure 4.1. (a) Schematic of the heat conduction experimental setup, and (b) Specific locations in which the temperature values were measured or derived

4.2.2. Calculation of effective thermal conductivity

In the experimental investigation of heat conduction, the temperature values of the planes perpendicular to the main heat conduction direction were represented by the thermocouple measured point temperature values (T_1-T_5). In this condition, the conductive heat transfer process in the test sample can be simplified as a one-dimensional (1D) problem, and the transformed 1D Fourier's law of heat conduction was used to calculate effective thermal conductivity values of different multi-layered lattice structure cores in the test samples.

Eq. (4.1) describes the relationship between input heat flux and temperature gradient along the main heat conduction direction.

$$q = -\lambda \frac{\Delta T}{\Delta x} \tag{4.1}$$

where q is the heat flux, λ is the thermal conductivity, and $\frac{\Delta T}{\Delta x}$ is the temperature gradient along the main heat conduction direction. Three repeated experiments were conducted on the solid block before the experiments on sandwich panels containing lattice structure cores. Using Eq. (4.1) to calculate its thermal conductivity, and the average value of 127 W/mK was used as the solid thermal conductivity of this batch fabricated AlSi10Mg solids.

Based on Eq. (4.1), the effective thermal conductivity of the lattice structure core is determined by the temperature difference between its lower (T_l) and upper surface (T_u). It was also assumed there were no heat losses to the ambient, namely the heat flux (q) generated from the heating system was all transferred throughout the tested sample from bottom up. The calculations of T_l and T_u are then shown in Eq. (4.2).

$$
\begin{aligned}
q &= -\lambda_s \frac{T_2 - T_1}{L_{12}} = -\lambda_s \frac{T_l - T_2}{L_{2l}} = -\lambda_s \frac{T_3 - T_u}{L_{3u}} = -\lambda_s \frac{T_4 - T_3}{L_{34}} \\
T_l &= T_2 - \frac{L_{2l}}{L_{12}} \cdot (T_1 - T_2) \\
T_u &= T_3 + \frac{L_{3u}}{L_{34}} \cdot (T_3 - T_4)
\end{aligned}
\tag{4.2}
$$

where λ_s is the thermal conductivity of the same batch SLM processed AlSi10Mg solid block, and L is the distance along the main heat conduction.

Applying Eq. (4.2) to Eq. (4.1), the effective thermal conductivity (λ_{eff}) of the lattice structure core was determined by Eq. (4.3).

$$
\begin{aligned}
q &= -\lambda_{eff} \frac{T_u - T_l}{L_{ul}} \\
\lambda_{eff} &= \frac{q \cdot L_{ul}}{T_l - T_u}
\end{aligned}
\tag{4.3}
$$

The uncertainty analysis of experimentally derived value of λ_{eff} referred to the method proposed by Moffat [93], as shown in Eq. (4.4). In the heat conduction experiments, the heat flux is determined by the heat rate of ceramic heater, which is the product of input current (I) and voltage (U). In the present study, the input current and voltage of ceramic heater was set as 0.50 A and 4.4 V respectively. The measurement accuracies of ammeter and voltmeter are ± 0.01 A and ± 0.1 V separately, and the accuracy of thermocouples reached up to 0.5 K after the calibration. As Figure 4.1(b) shows, $\frac{L_{2l}}{L_{12}} = \frac{L_{3u}}{L_{34}} = 0.75$. Applying the summarized parameter values into Eq. (4.4), the calculated maximum uncertainty of λ_{eff} was found within 5%.

$$\frac{\delta\lambda_{eff}}{\lambda_{eff}}=\sqrt{\left(\frac{\delta I}{I}\right)^2+\left(\frac{\delta U}{U}\right)^2+\left[\frac{\delta\left(T_l-T_u\right)}{T_l-T_u}\right]^2}$$
$$\frac{\delta\left(T_l-T_u\right)}{T_l-T_u}=\sqrt{(\frac{L_{2l}}{L_{12}}\cdot\frac{\delta T_1}{T_1})^2+\left[(1+\frac{L_{2l}}{L_{12}})\cdot\frac{\delta T_2}{T_2}\right]^2+\left[\left(\frac{L_{3u}}{L_{34}}-1\right)\cdot\frac{\delta T_3}{T_3}\right]^2+\left(\frac{L_{3u}}{L_{34}}\cdot\frac{\delta T_4}{T_4}\right)^2} \quad (4.4)$$

4.3. Numerical simulations

4.3.1 Background

Aiming at studying the detailed temperature distributions in different lattice structures, and validating the experimental results, the numerical model consistent with the test sample geometry and related experimental settings was built up for simulating the steady-state heat conduction process. The commercial computational fluid dynamics (CFD) software ANSYS FLUENT 20.1 was used in the numerical study, which provides stable solutions to the 3D steady-state heat conduction problem instead of using the simplified 1D theory to determine the conductive heat transfer characteristics in experiments. For the experiment on each test sample, the corresponding numerical model was built and validated by the experimental data, to guarantee the reliability and effectiveness of experimental and numerical results in the steady-state heat conduction investigation.

4.3.2 Simulation model

The test sample containing multi-layered lattice structure core is symmetric about the middle planes perpendicular to the bottom heating surface. Besides, the constant heat flux thermal boundary condition of the bottom and the constant temperature thermal boundary condition of the top are also symmetric about the main heat conduction direction. Hence, a quarter of the test sample and the coupled air were sufficient and

good enough for modelling the thermal conditions in the whole test sample, as shown in Figure 4.2. The quarter of the test sample was defined as the solid domain in the numerical model, and the dry air between the struts was defined as the fluid domain and coupled with the solid domain, their properties for being used in the simulations were summarized in Table 4.1. In the numerical model, the setting of boundary conditions was totally same as the ones in experiments. The constant heat flux of 3819.44 W/mK was set on the bottom surface of the test sample, and the constant temperature of 295 K was set on the top surface of the test sample. The symmetric planes were also defined for further showing the simulated temperature distributions of the whole test sample in the CFD post process software CFD-POST 20.1. The rest walls were set as adiabatic walls.

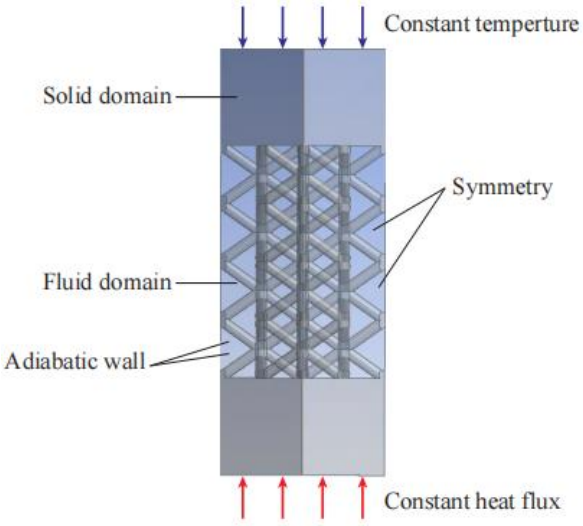

Figure 4.2. Geometry built for the 3D steady-state heat conduction simulation

Table 4.1 Material properties of AlSi10Mg and dry air [94]

Material/properties	AlSi10Mg	Air
Density (kg/m^3)	2670	$9.55 \times 10^{-6}T^2$ - $0.0044T+1.2912$
Specific heat (J/kgK)	900	1006.43
Thermal conductivity (W/mK)	127	$7.07 \times 10^{-5}T+0.0242$
Dynamic viscosity (Pa·s)	—	$4.62 \times 10^{-8}T+1.79\times 10^{-5}$

In the numerical model, the single-phase natural convection in air and thermal conduction in solid structure were simulated simultaneously for predicting steady state thermal performance of different lattice structures. In the present study, AlSi10Mg was used as raw materials for fabricating solid structures, the most important parameter thermal conductivity was measured in experiments. In the fluid domain, the movement of dry air was driven by the buoyance force which was induced by the uneven air density in the domain. The laminar flow was assumed the dominant fluid motion in the movement of the natural convection. The solvers of ANSYS FLUENT 20.1 were used to solve the mass, momentum, and energy governing equations in the steady state convective heat transfer, which occurred in the fluid domain. Eq. (4.5) to Eq. (4.7) shows the correspondent governing equations.

$$\nabla \cdot \vec{V} = 0 \tag{4.5}$$

$$\rho V \cdot \nabla \vec{V} = -\nabla p + \mu \nabla^2 \vec{V} \tag{4.6}$$

$$\rho C_p \vec{V} \cdot \nabla T + \nabla \cdot \left(-\lambda_f \nabla T\right) = 0 \tag{4.7}$$

where ρ is the density of air, $\vec{V}$ is the velocity vector of air, λ_f is the thermal conductivity of air, and μ is the dynamic viscosity. In the solid domain, as the heat conduction process is 3D steady-state, and there is no existence of internal heat source, the governing equation for the energy can be simplified to Eq. (4.8).

$$\nabla^2 T = 0 \tag{4.8}$$

As there are no phase changes of materials at the fluid-solid interface, and ignoring the thermal radiation, the interface should also follow the conservation of energy. The corresponding boundary conditions are set as follows:

$$T_f = T_s \tag{4.9}$$

$$q_f = -\lambda_f \frac{\partial T_f}{\partial n} = -\lambda_s \frac{\partial T_s}{\partial n} = q_s \tag{4.10}$$

where T_f is the fluid temperature at the interface, T_s is the solid temperature at the interface, λ_f, λ_s are thermal conductivities of fluid and solid materials separately, and q_f, q_s are the heat fluxes on the fluid and solid side of the fluid-solid interface correspondingly.

In the numerical model, the gravity value of -9.8 m/s^2 along the main heat conduction direction was set for generating the buoyance force in the simulated fluid domain. The coupled scheme was used for the pressure-velocity coupling, the gradient equation was discretized by least squares cell-based scheme, and the PRESTO! scheme was selected for pressure correction equations. The momentum and energy equations were discretized by the second order upwind scheme. The convergence criterion of 10^{-5} for velocity components, and 10^{-8} for continuity and energy equations was used for each calculation.

4.3.3 Mesh independency study

In the numerical simulations, the unstructured tetrahedral meshes were generated in the solid and fluid domain, and the meshes near the struts were refined for the better coupled heat transfer at fluid-solid interface. Four sets of meshes were separately tested on the test sample containing BCC, FCC-Z, FCC-XY, or octet-truss lattice structure cores (ε=0.82) for checking whether the solutions are independent from the number of

meshing elements. The simulated temperature values of the lattice structure core lower surface (T_l) under different mesh densities were plotted for monitoring the mesh independency, as shown in Figure 4.3. It was found that for each test sample, the T_l value almost didn't change at the second set of meshes. Thus, the correspondent meshes with 2.6 million, 1.8 million, 1.7 million, and 10.5 million elements were respectively used in the test samples with BCC, FCC-Z, FCC-XY, and octet-truss lattice structure cores, to spend reasonable computation resources and result in simulation results with the convincing accuracy, the applied meshes were shown in Figure 4.4.

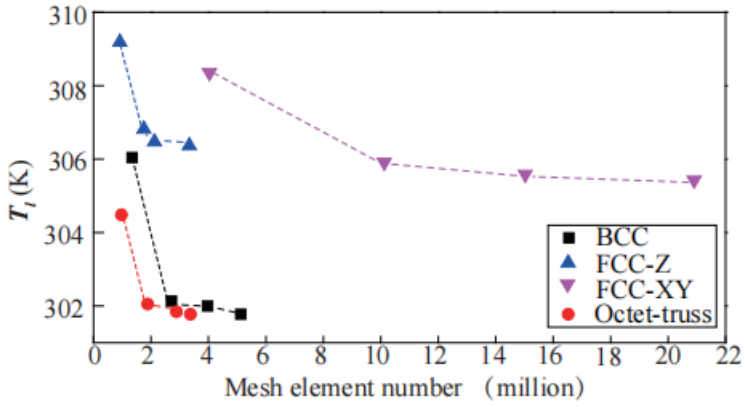

Figure 4.3. Mesh independence study for temperature value of the test sample bottom surface

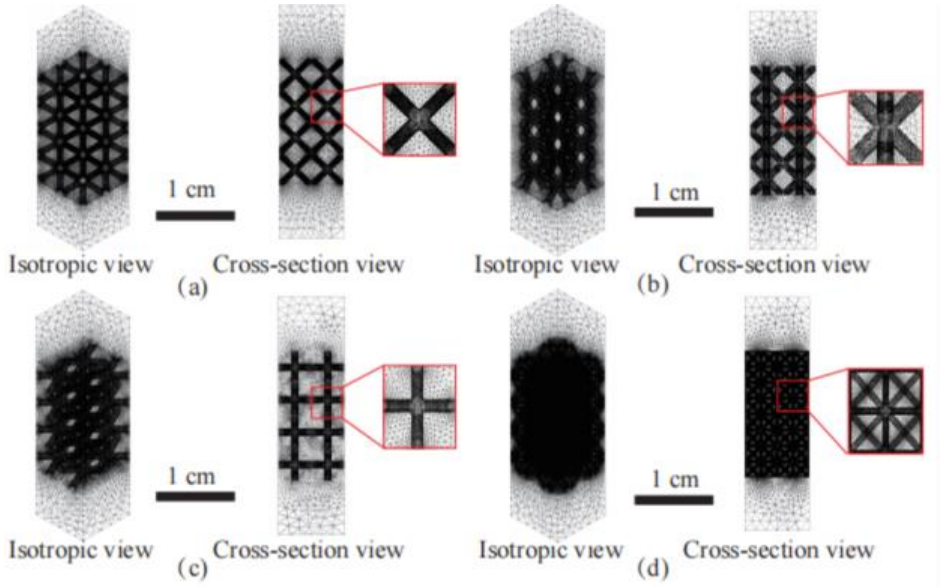

Figure 4.4. Meshes used in the models (a) sample with BCC core, (b) sample with FCC-Z core, (c) sample with FCC-XY core, and (d) sample with octet-truss core.

4.3.4 Model validation

Figure 4.5 shows the comparisons between experimentally and numerically derived effective thermal conductivity of lattice structures used in the heat conduction investigation. It was found that the experimental data fit very well with the simulation results, the maximum difference between them was around 1.2 W/mK. The comparison validated the effectiveness of the numerical model, as well as supported the accuracy of the experimental data.

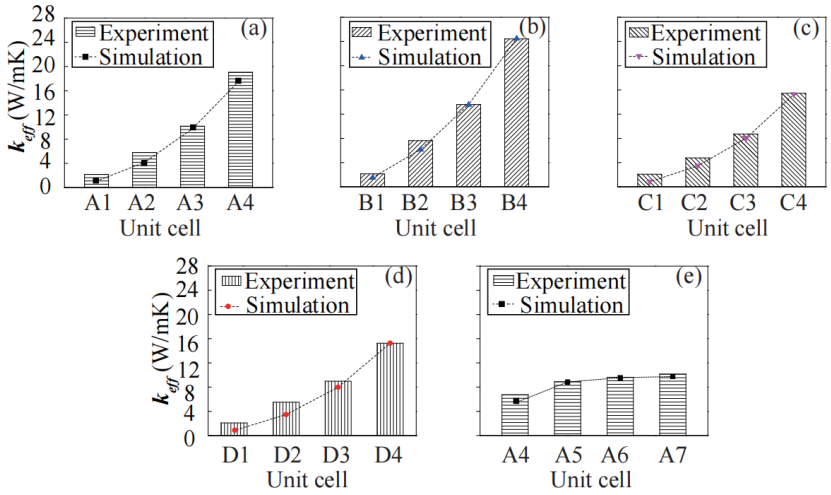

Figure 4.5. Comparisons between experimentally and numerically derived effective thermal conductivity values of: (a) BCC, (b) FCC, (c) octet-truss, and (d) tapered strut composed BCC.

4.4 Results and discussion

4.4.1 Effects of structural parameters on the effective thermal conductivity

4.4.1.1 Effect of porosity

Figure 4.6 shows one group experimental data, the slope of the line located from 10 to 34 mm shows the thermal conduction performance of lattice structure, which is inversely proportional to the effective thermal conductivity.

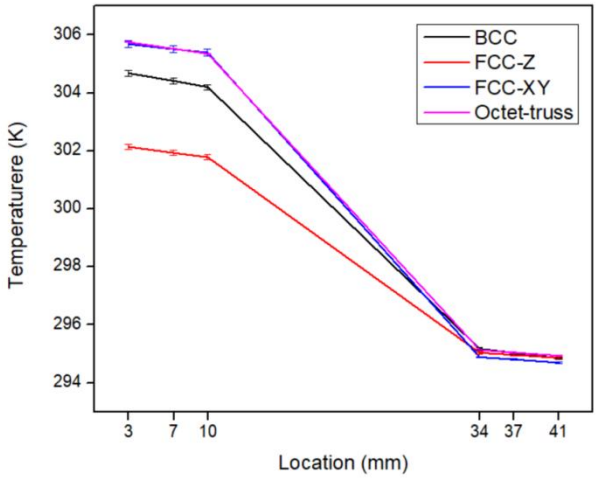

Figure 4.6. Experimental data of T_1, T_2, T_3, T_4, T_l, and T_u in different lattice structures at the porosity of 0.82

As three repeated experiments were conducted on each sample, the effective thermal conductivity was described by its average and standard deviation values. In this experimental study, the ratio of standard deviation to the average was controlled within 1.15%, which demonstrated the excellent reliability and repeatability of the experiments. In this condition, the value of experimentally derived effective thermal conductivity can be directly expressed by its average value. In the numerical investigations, the average plane temperature values of lattice structure core lower and upper surface (T_l and T_u) were used to calculate the effective thermal conductivity, rather than the ones derived from point temperature values. Figure 4.7 shows the comparisons between the experimental and numerical effective thermal conductivity values, as well as the relationship between the effective thermal conductivity and the porosity. It was found that the experimental data fit very well with the simulation results, the maximum difference between them was around 1.2 W/mK. The comparison validated the effectiveness of the numerical model and also supported the accuracy of the experimental data.

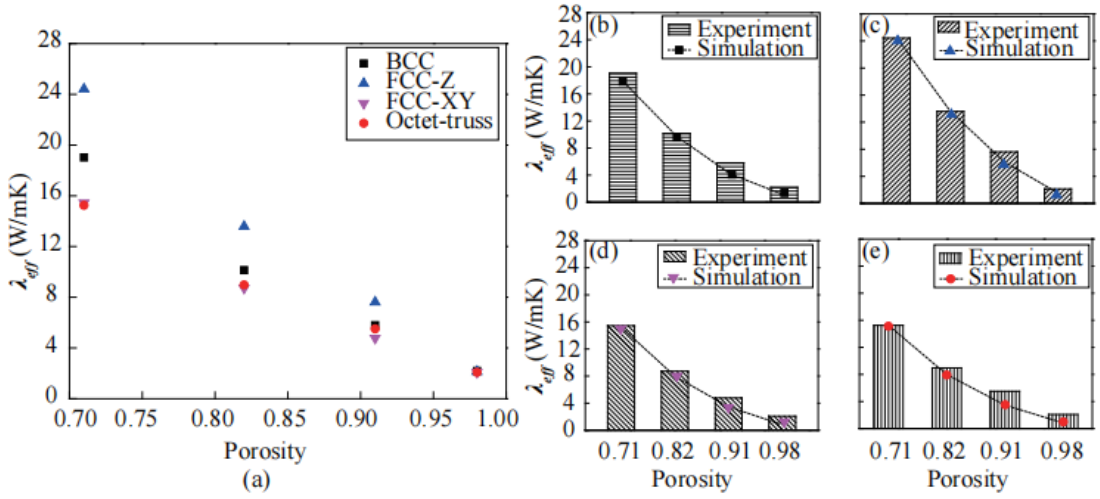

Figure 4.7. (a) the effect of porosity on experimentally derived effective thermal conductivity, and the relationship between porosity and effective thermal conductivity on (b) BCC, (c) FCC-Z, (d) FCC-XY, and (e) octet-truss lattice structures

Figure 4.8 shows the simulated temperature contours of all test samples. It can be seen that for one type of lattice structure, the temperature range decreased as the porosity value decreased, which demonstrated the better heat conduction performance. Whilst for different types of lattice structures, their temperature ranges were very different even at the same porosity value.

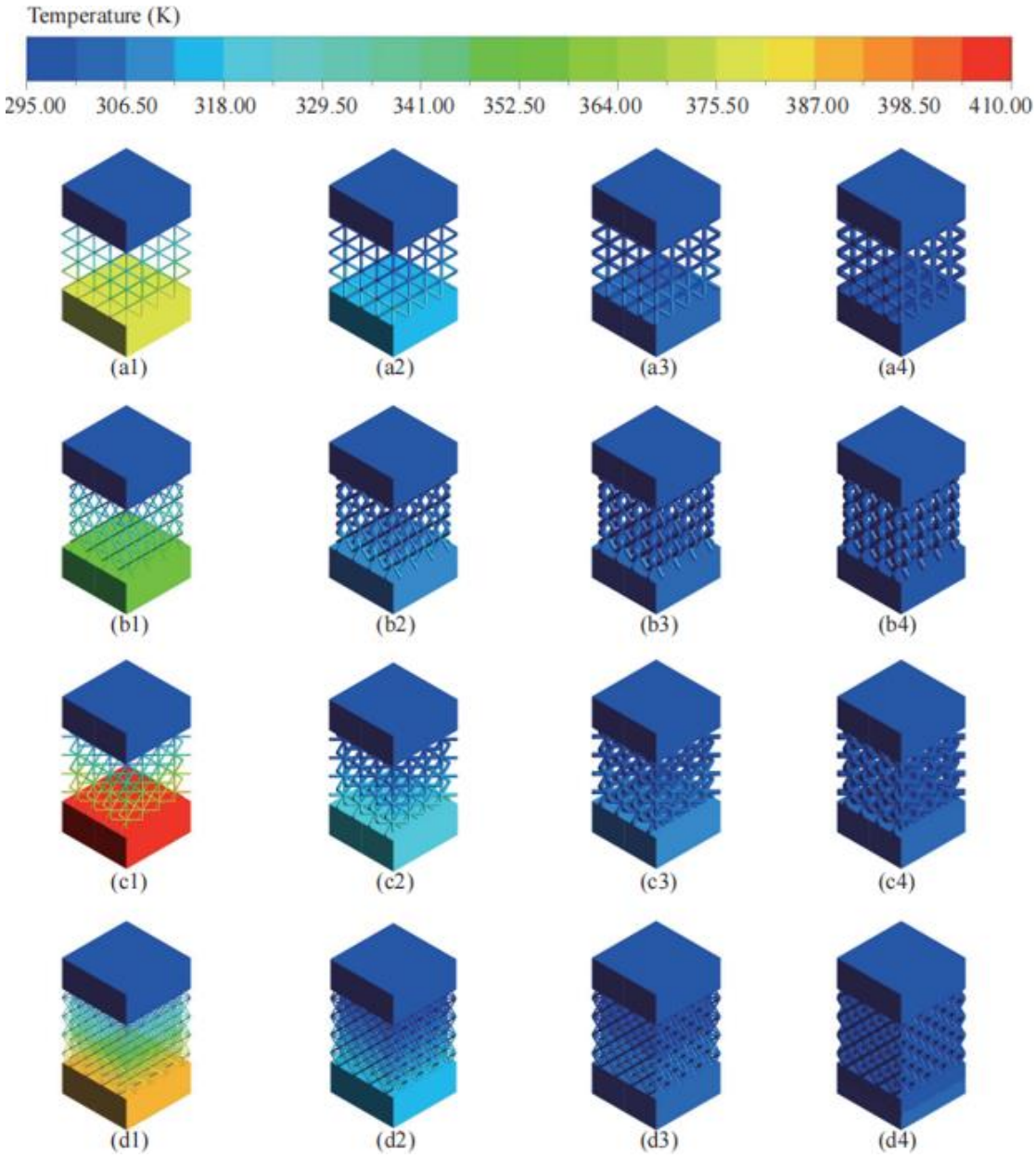

Figure 4.8. Simulated temperature contours of all test samples (a1-a4) BCC; (b1-b4) FCC-Z; (c1-c4) FCC-XY; (d1-d4) octet-truss. (a1, b1, c1, d1) porosity= 0.98; (a2, b2, c2, d2) porosity= 0.91; (a3, b3, c3, d3) porosity= 0.82; (a4, b4, c4, d4) porosity= 0.71.

As Figure 4.7 shows, for a specific type of lattice structure, the effective thermal conductivity increased with the incremental of strut radius value. The strut radius value determined the structure porosity when the structure type and unit cell length are fixed. The larger radius value contributes to the larger volume of solid-phase materials and

smaller porosity, then further increased the effective thermal conductivity of the specific lattice structure. It was also found that the FCC-Z lattice structure always performed the highest thermal conductivity at different values of porosity, followed by the BCC lattice structure. The effective thermal conductivities of FCC-XY and octet-truss lattice structure were very similar when the porosity was same, and both performed worse conductive heat transfer characteristics than FCC-Z and BCC lattice structures. The most significant finding in this section is that for different types of lattice structures, their effective thermal conductivities varied with each other even at the same porosity value. The finding is not in accordance with the past studies, which use porosity value to derive the formula of effective thermal conductivity.

4.4.1.2 Effect of specific surface area

As the specific surface area is the ratio of surface area to the volume of solid, it reflects the surface density of the solid-phase material in the lattice structure. Figure 4.9 shows the effect of specific surface area on the effective thermal conductivity. It was found that for a specific lattice structure, the effective thermal conductivity decreased as the specific surface area increased. When the lattice structure type was fixed, as the component strut radius increased, the solid volume definitely increased, while the surface area decreased or increased slower than solid volume, this resulted in the lower specific surface area but higher effective thermal conductivity. In another word, the solid volume plays more important role than the contact surface area on the effective thermal conductivity.

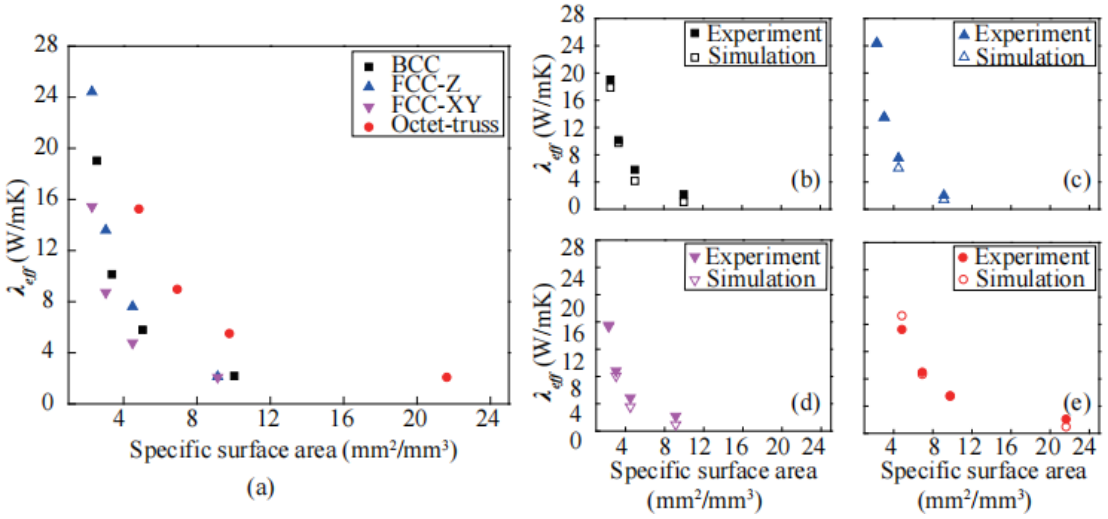

Figure 4.9. (a) the effect of specific surface area on experimentally derived effective thermal conductivity, and the relationship between specific surface area and effective thermal conductivity on (b) BCC, (c) FCC-Z, (d) FCC-XY, and (e) octet-truss lattice structures

4.4.1.3 Effect of minimum cross-section area

Based on the results from the effect study of porosity and specific surface area, it was found that neither the same porosity value nor the same specific surface area value contributes to the same effective thermal conductivity. Especially for the FCC-Z and FCC-XY lattice structures, they share the same porosity and specific surface area at the same time, while the FCC-Z always has the better conductive heat transfer performance than FCC-XY.

In this section, the effect of cross-section area (A_c) along the main heat conduction direction was firstly investigated. As Figure 4.10 (a) and (b) shows the cross-section areas along the heat conduction direction in FCC-Z and FCC-XY lattice structures respectively. At the same strut radius value (r), the minimum cross-section area (min. A_c) of FCC-Z is always larger than that of FCC-XY. Then Figure 4.10 (c) summarizes the relationship between the minimum cross-section area and effective thermal

conductivity. It was found with the same porosity and specific surface area, and the larger minimum cross-section area contributes to the larger effective thermal conductivity. The effect of the minimum cross-section area looks very similar to the cask effect, namely the effective thermal conductivity was determined by the smallest cross-section area along the main heat conduction direction.

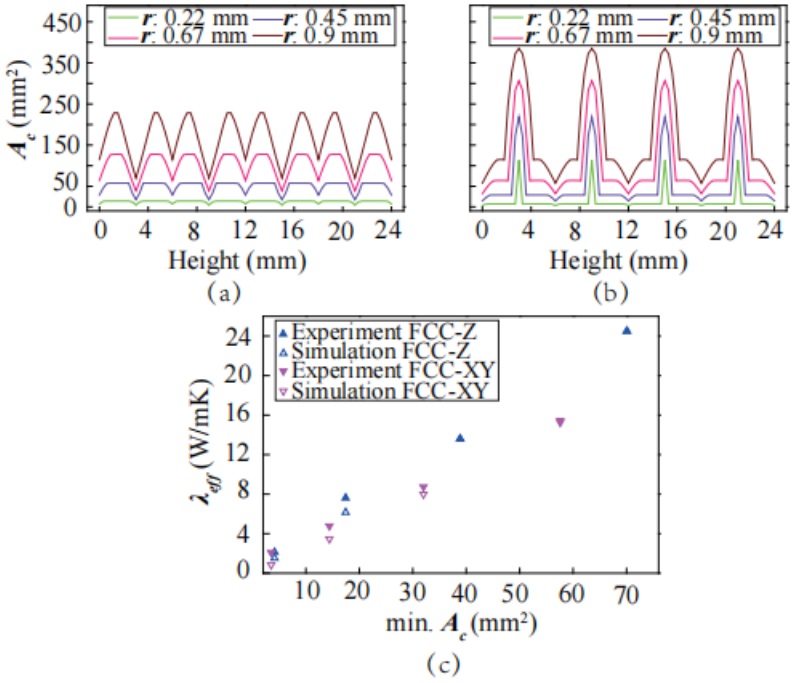

Figure 4.10. (a) cross-section area of FCC-Z along the main heat conduction direction, (b) cross-section area of FCC-XY along the main heat conduction direction, and (c) the effect of minimum cross-section area on the effective thermal conductivity

For better validating the conception of minimum cross-section area, the test samples with BCC lattice structure cores containing tapered struts (sample A5, A6, A7), as well as the sample containing BCC lattice structure with 6 mm unit cell length and 0.6 mm strut radius (sample A3) were experimentally and numerically tested in the term of effective thermal conductivity. Figure 4.11 shows the detailed cross-section area distribution of them and the effect of minimum cross-section area on the effective

thermal conductivity. The results also claimed that the larger minimum conduction cross-section area contributes to the better conductive heat transfer performance. Figure 4.12 shows the simulated temperature contours, which demonstrates the effect of minimum cross-section area visually. It can be seen that as long with the decrease of the minimum conduction cross-section area, the temperature value range enlarges, which is in accordance with the smaller effective thermal conductivity.

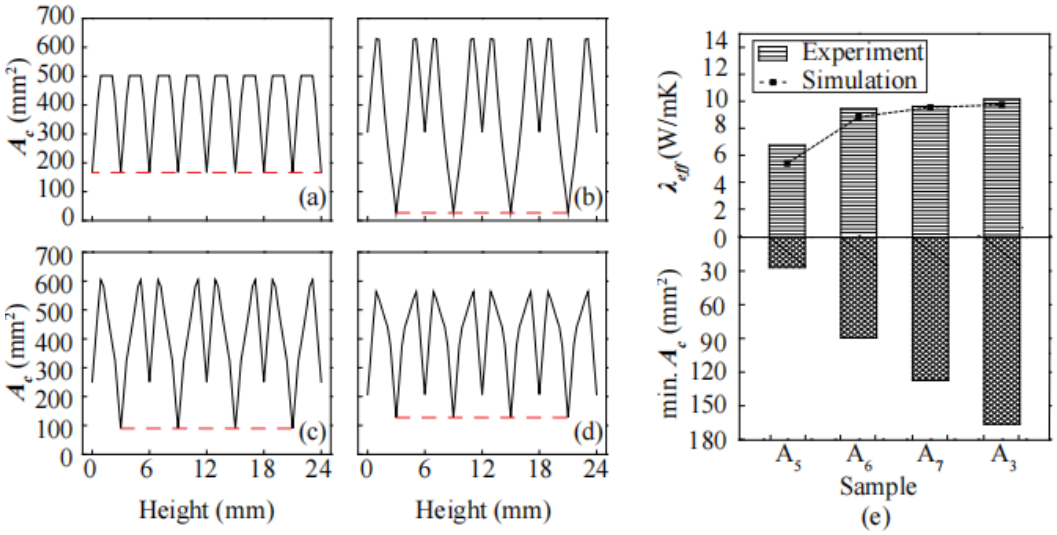

Figure 4.11 (a-d) cross-section of sample A3, A5, A6, A7 along the main heat conduction direction, (e) the effect of minimum cross-section area on the effective thermal conductivity

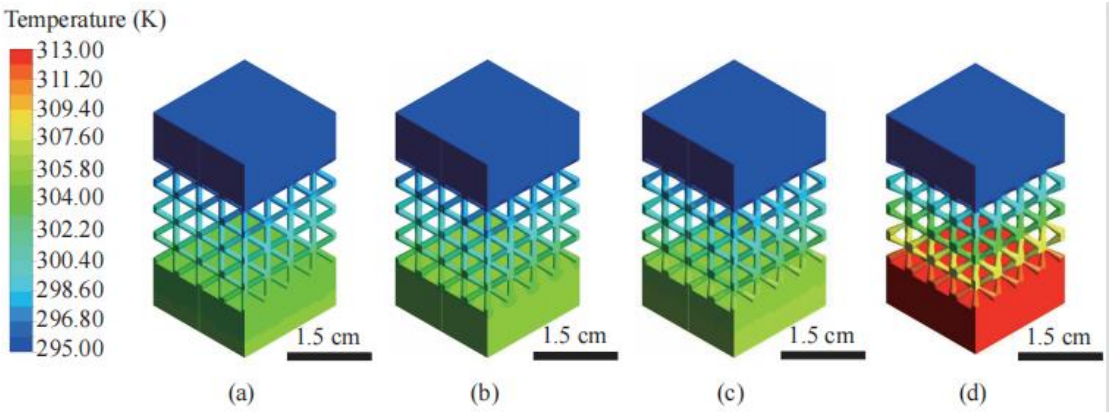

Figure 4.12. The temperature contours of test samples containing BCC lattice structure cores with tapered struts

4.4.2 Specific thermal conductivity

Based on the previous studies, it was found that the increment of solid phase material volume contributes to the increment of effective thermal conductivity. However, lightweight multi-layered lattice structures with excellent conductive heat transfer capabilities are expected in engineering. For comparing weight and steady state heat conduction performance of multi-layered BCC, FCC, and octet-truss lattice structures at the same time, a new concept of specific thermal conductivity (λ_{eff}) was proposed, which was referred to the definition of the specific strength in the mechanical analysis. The specific strength which is defined as the ratio of compressive strength to the relative density, and the firstly proposed conception of specific thermal conductivity was defined as the ratio of effective thermal conductivity to the relative density (λ_{eff}/ρ_r). Based on the definition, it can be concluded that the lattice structure with the larger specific thermal conductivity will be more popular in industry than others, as it meets the engineering requirements of lightweight and excellent conduction performance at the same time.

$$\rho_r = \frac{V_S}{V_T} \tag{4.11}$$

where ρ_r is the relative density, V_s and V_T are solid volume and total volume separately. Figure 4.13 summarized the numerical derived specific thermal conductivity values of different lattice structures. It can be found at the smaller radius range, there is a transition at the specific thermal conductivity value. From 0.2 mm to 0.7 mm, FCC-Z performs best in the term of specific thermal conductivity. Over 0.7 mm, octet-truss performs better. At the end of the specific thermal conductivity plot, the value approaches the thermal conductivity of the solid AlSi10Mg of 127 W/mK.

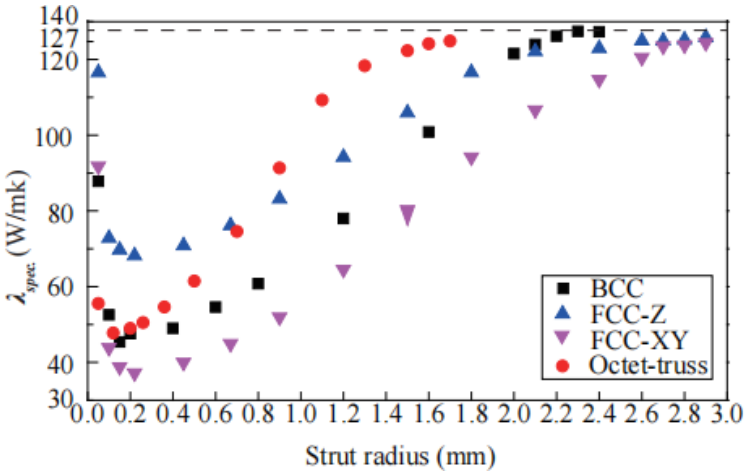

Figure 4.13 Specific thermal conductivity

4.5 Summary

This chapter fully investigated the steady-state heat conduction performance of BCC, FCC-Z, FCC-XY, and octet-truss lattice structures from experimental and numerical approaches. It was found that for the specific lattice structure, decreasing the porosity or the specific surface area would increase the effective thermal conductivity. However, for different lattice structures, the effects of porosity and specific surface area on the heat conduction performance was not that remarkable. Then, the effect of the minimum cross-section area along the main heat conduction direction was studied, it was found at the same porosity and specific surface area, the effective thermal conductivity was

determined by the minimum cross-section area, similar to the cask effect. At the end of this chapter, a new conception of specific thermal conductivity was firstly proposed and used to evaluate the lightweight characteristic and heat conduction performance of the lattice structure at the same time. Subsequent to the investigation of lattice structure heat conduction performance, the forced convective characteristics were determined for fully studying the heat transfer properties in lattice structures.

Chapter 5. Forced convective heat transfer in a channel filled with lattice structures

5.1 Introduction

The air forced convection in a channel filled with lattice structures were experimentally investigated in this chapter to compare the heat transfer and hydraulic characteristics among different SLM processed test samples. In this study, the sandwich panels sharing the same porosity multi-layered BCC, FCC-Z, FCC-XY, and octet-truss lattice structure cores were used as test samples, and the forced air flow with different velocity values passed through the channel filled with the lattice structure cores. The hydraulic characteristics including pressure drop gradient, permeability, and Forchheimer coefficient were derived from the measured pressure drop values. Besides, the convective heat transfer characteristics including heat transfer coefficient, Nusselt number, and convective heat transfer coefficient were also summarized and compared between different structures. After experiments, the numerical models were used to support the experimental data and visually exhibited the temperature contours of lattice structure and velocity contours in the air domain, for better analyzing and comparing heat transfer and hydraulic properties of different lattice structures.

5.2 Experiments

5.2.1. Experimental setup

The experimental setup used in this study consists of the compressed air supply system and the test module, as shown in Figure *5.1*. In the compressed air supply system, the compressed dry air flowed from the air tank, and the velocity value of it was controlled

by the rotation valve. As the cross-section area of air supplying channel is smaller than the internal cross-section area of the Teflon channel, an expansion section with 1:4 expansion ratio was used to connect the air supplying tube and Teflon channel in the test module. After flowing into the Teflon channel, the air was straightened by honeycombs and wire mesh, a probe anemometer mounted at the center of the channel cross-section was then used to test the inlet air velocity. There are three sections in the Teflon channel, namely the inlet section, the middle section for mounting the test sample, and the outlet section. In this study, the length of inlet channel was set as 700 mm, which is 35 times of the sample height (20 mm), so as to make sure the air flowed into the lattice structure was developed straightened flow. The lattice structure core was used to fill in the middle section of the Teflon channel, for getting the more accurate experimental data showing the properties of lattice structures without the effect of gaps. The test sample, namely the sandwich panel was mounted at the Teflon middle section, as well as placed on the upper surface of the heating system. The heating system was a copper whose upper surface has the same dimensions as the bottom surface of the sandwich panel. In the copper, four cartridge heaters were inserted with an equal distance of 14 mm to each other along the flow direction, the minimum distance between the heater and the copper block upper surface was set as 10 mm and the length of cartridge heater was set same as the width of the copper block and test sample, for guaranteeing the even heat flux was transferred to the bottom of the test sample. The cartridge heaters were parallel connected to the power supplier, and their input current and voltage values were kept similar to each other, which was also set to make sure every point at the test sample bottom surface has the same input heat flux value during experiments.

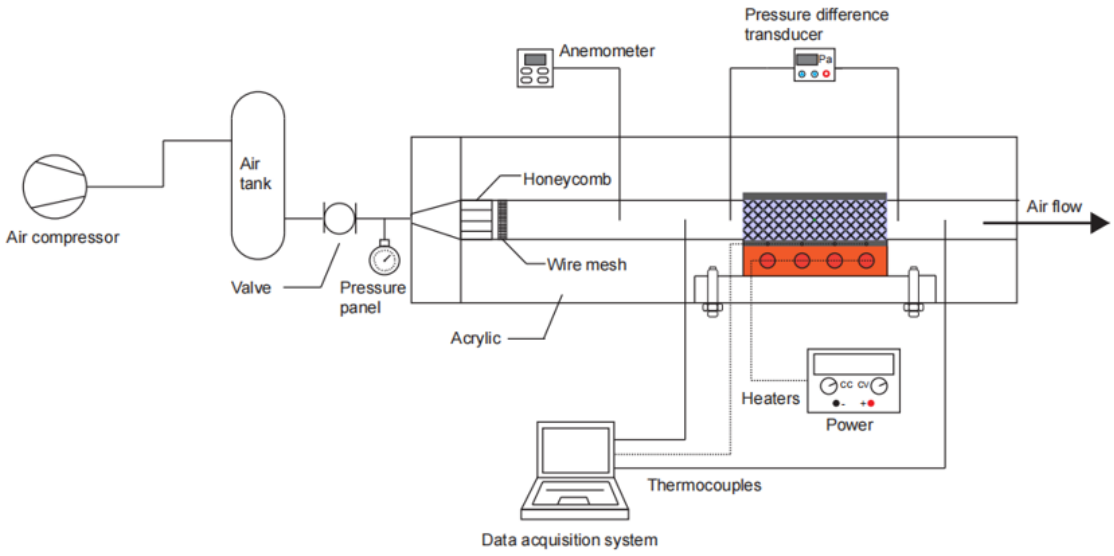

Figure 5.1. The schematic of air forced convection experimental setup

In total, six K-type thermocouples were used in this experimental setup, four of them were inserted into the lower panel of the test samples with 14 mm equal distance to each other, and these four thermocouples were placed along the flow direction, the insertion depth was set as 10 mm, the half length of the sample width. These four thermocouples were used to test the wall temperature values in the test sample (T_1-T_4). Another two K-type thermocouples were inserted into the inlet and outlet channel separately, their positions were kept as the centre points of the planes perpendicular to the air flow direction, so as to measure the inlet and outlet temperature values (T_{in} and T_{out}). A digital pressure transducer was used to test the pressure drop value between the ends of the test sample mounted in the setup. In order to make sure the consistency of measured parameter values, the two taps of the pressure transducer were placed at the same positions of the thermocouples used to measure inlet and outlet temperature values.

5.2.2. Experimental procedures

The steady-state heat convection experiments were conducted on test samples to derive the parameter values of hydraulic and heat transfer performance. The experiments were conducted at the room temperature of 300 K and the standard gas pressure of 101325 Pa. The purpose of the combined use of rotation valve and digital anemometer was to keep the inlet velocity as a constant. The details were: opening the rotation valve first, then using the display of the anemometer as a feedback value to adjust the rotation valve, so as to adjust the velocity value of the inlet air to the lattice structure. In each experiment, the inlet air velocity was kept as a constant till the whole system reached a steady state over 10 minutes. For comparing the hydraulic and heat transfer characteristics of different lattice structures more adequately, the inlet air velocity was adjusted from 2 m/s to 8 m/s with the interval of 1 m/s.

In the test module, for checking the conductive heat transfer capability of lattice structure, the cartridge heaters were used to generate even heat flux to the lattice structure, and then the heat was mostly dissipated by the heat convection. In experiments, the constant heat flux of 2857.14 W/m^2 was generated and placed on the test sample bottom surface.

As long with the constant velocity air supplied to the inlet section of the Teflon channel and the heaters started heating the test sample, the thermocouples including T_1-T_4 for measuring the wall temperature values, and T_{in} and T_{out} used for measuring inlet and outlet air velocities, were employed to measure the instant temperature values at the specific locations. At the same time, the digital pressure difference transducer started recording the pressure drop through the lattice structure. The recording processes by thermocouples and pressures transducer would end till the system reached a steady stated. In this study, the steady state was defined as the variation of thermocouple

measured temperature value was smaller than 0.1 K, and the variation of measured pressure drop value was smaller than 1 Pa over three minutes.

For collecting the accurate and reliable experimental data without the effect of experiment error, three repeated experiments were conducted on each test sample under the same air flow velocity. In the experiments, all thermocouples were calibrated with an accuracy of 0.1 K, the measurement accuracy of the digital anemometer reached up to 0.01 m/s, and the accuracy of the pressure transducer was 1 Pa.

5.2.3. Hydraulic parameters calculation

The pressure drop value (ΔP) is proportional to the pumping power needed in the thermal system, and proportional to the energy absorbed by the media, that's why it's a significant parameter used for evaluation hydraulic performance of porous structures. For easier comparing the pressure drop values of different scaled porous structures, the pressure drop gradient $\Delta P/L$ was always used, where L is the length that the fluid passes through. Typically, the pressure drop gradient value can be seen as a function of the average velocity, as shown in Eq. (5.1). The values of constant a and b are determined by the physical properties of the fluid flow, as shown in Eq. (5.2). Herein the permeability (K) and Forchheimer coefficient (C_F) are the other two significant parameters used to evaluate the hydraulic characteristic of porous structures. In this study, the magnitude of permeability (K) reflects the porous structure capability of diffusing the air, and Forchheimer coefficient (C_F) is a parameter used to evaluate the magnitude of the flow resistance induced by the fluid drag force. The values of K and C_F were always experimentally determined by the Darcy's law.

$$\frac{\Delta P}{L} = aV_{avg.} + bV_{avg.}^2 \tag{5.1}$$

where

$$a = \frac{\mu_f}{K}$$
$$b = \frac{\rho_f C_F}{\sqrt{K}} \tag{5.2}$$

a and b are the constants to be determined, μ_f, ρ_f , and V_{avg} are the dynamic viscosity, density, and average velocity of the fluid. In this study, the experiments were conducted at the room temperature of 300 K, so the values of μ_f and ρ_f can be determined. Then based on the inlet air velocity value in experiments and data in the figure indicating the relationship between the pressure drop gradient and velocity, the values of permeability (K) and Forchheimer coefficient (C_F) can be experimentally determined. The Darcy's number (Da) is defined as a dimensionless parameter to evaluate the permeability of porous structure, and the value of it is the ratio of permeability to the square of characteristic length, as shown in Eq. (5.3) In this study, the characteristic length was represented as the hydraulic diameter (D_h) of the Teflon channel, which was defined as the four times of the channel cross-section area (A) divided by perimeter ($P_{er.}$). Applying Eq. (5.3) to Eq. (5.1), the function of the dimensionless parameter friction factor (f) was shown in Eq. (5.4). The introduction of the friction factor (f) creates a link between the pressure drop through the specific lattice structure and the hydraulic diameter (D_h).

$$D_a = \frac{K}{D_h^2} \tag{5.3}$$

$$f = \left(\frac{\Delta P}{L} \cdot D_h \right) \cdot \left(\frac{1}{\rho_f \, V_{avg.}^2 / 2} \right) \tag{5.4}$$

Combining Eq. (5.3) with Eq. (5.4), the product of friction factor and square root value of Darcy's number was shown in Eq. (5.5). In addition, employing the conception of modified Reynolds number (Re_k), the Eq. (5.5) was transformed into Eq. (5.6).

$$\frac{fD_a^{1/2}}{2} = \frac{\Delta P}{L}\frac{\sqrt{K}}{\rho_f V_{avg.}^2} \tag{5.5}$$

$$fD_a^{1/2} = \frac{2}{\mathrm{Re}_K} + 2C_F \tag{5.6}$$

where $\mathrm{Re}_K = \frac{\rho_f V_{avg.}\sqrt{K}}{\mu_f}$, defined as the modified and permeability (K) based Reynolds number *Re*.

5.2.4. Heat transfer parameters calculation

In the forced convective heat transfer process, the flow channel heat transfer coefficient (h_c) was determined by the input heat flux and the temperature difference between the test sample base and the fluid temperature. In this study, the four K-type thermocouple measured temperature values (T_1-T_4) were averaged and used as the wall or base temperature of the sample, as shown in Eq. (5.7).

$$T_b = \frac{1}{4}\sum_{i=1}^{4} T_i \tag{5.7}$$

$$h_c = \frac{q}{\Delta T} = \frac{q}{T_b - T_{in}} \tag{5.8}$$

Based on Eq. (5.7) and Eq. (5.8), the calculations of Reynolds number (Re_c) and Nusselt number (Nu_c) were derived, as shown in Eq. (5.9) and Eq. (5.10). Their plots were used to investigate the effects of velocity value on the convective heat transfer efficiency. Besides, the plot can also be used to compare the heat convection performance of different lattice structures.

$$Nu_c = \frac{h_c \cdot D_h}{\lambda_f} \tag{5.9}$$

$$\mathrm{Re}_c = \frac{\rho_f \mathrm{V}_{\mathrm{avg}.} D_h}{\mu_f} \tag{5.10}$$

In experiments, the heat generated by the cartridge heaters was transferred in three ways: the heat loss to the surrounding environment, the conducive heat transfer to the Teflon channel, and the air forced convective heat transfer. The conception of convective heat transfer rate (η) was introduced to study the percentage of heat transferred by the heat convection. The value of η equals the ratio of the heat transferred by the convection to the total heat generated from the heaters. Eq. (5.11) shows the definition of η.

$$\eta = \frac{Q_{convec.}}{Q_{input}} = \frac{\dot{M} C_p (T_{out} - T_{in})}{UI} \tag{5.11}$$

where $\dot{M}$ is the mass flow rate, can be calculated by the product of air velocity ($V_{avg.}$), channel cross-section area, and air density. In addition, *U* and *I* are total input voltage and current values of the heaters separately. In this study, the heat generated from the heaters was 4 W by setting the voltage and current values as 2 V and 2 A respectively.

5.3 Results and discussion

5.3.1. Hydraulic characteristics

5.3.1.1. Pressure drop

Figure *5.2* shows the experimentally derived values of pressure drop gradient through BCC, FCC-Z, FCC-XY, and octet-truss lattice structures at different air velocity values.

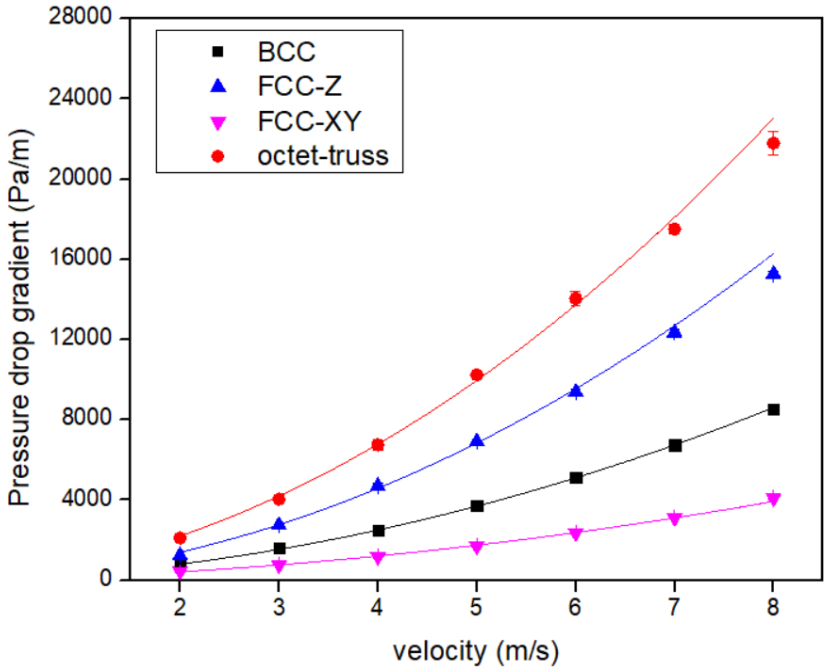

Figure 5.2. Comparisons of pressure drop gradient in different typed lattice structures

It can be found that the octet-truss lattice structure performed the largest pressure drop value at different air velocity values, but the pumping power needed for the air to flow through the FCC-XY lattice structure was always the lowest. As these four types of lattice structures share the same porosity, it was concluded that the pressure drop through the lattice structure is irrelevant to the porosity. Except for the porosity, the FCC-XY and FCC-Z lattice structures also share the same interfacial surface area and specific surface area, the only difference between them is that the FCC-XY lattice structure has the larger open area ratio. It was also found the lattice structures can be ordered as the sequency of octet-truss, FCC-Z, BCC, and FCC-XY lattice structures based on the magnitude of the open area ration, which is consistent with the magnitude of the pressure drop gradient. The most remarkable difference is between FCC-XY and FCC-Z lattice structures. It can be seen that the FCC-XY lattice structure performed the much lower pressure drop than FCC-Z lattice structure. At the velocity value of 8 m/s,

the pressure drop value of FCC-Z lattice structure is almost four times of that of FCC-XY lattice structure.

For calculating the values of permeability (K) and Forchheimer coefficient (C_F), least square methods were used to fit Eq. (5.1) with the data in Figure *5.2*. For each lattice structure, the regression coefficient of R^2 was set larger than 99.6, then the correspondent values of permeability (K) and Forchheimer coefficient (C_F) can be obtained according to their definitions shown in Eq. (5.2). The calculated values of permeability (K) and Forchheimer coefficient (C_F) are shown in Table 5.1. It was found that the FCC-XY lattice structure has the largest permeability value, followed by BCC and FCC-Z lattice structures, while the octet-truss lattice structure has the smallest permeability, which means it has the worst capability of transferring the fluid media. It was also found that the structure with the larger permeability value has the smaller Forchheimer coefficient, which illustrates that in this kind of structure, the fluid drag force induced flow resistance is relatively small. The experimental results also demonstrated that the open area ratio plays a more important role than porosity and interfacial surface area on the permeability and Forchheimer coefficient.

Table 5.1. The summary of permeability and Forchheimer coefficient

	BCC	FCC-Z	FCC-XY	Octet-truss
Permeability K (m^2)	1.65×10^{-7}	6.07×10^{-8}	2.20×10^{-7}	2.85×10^{-8}
Forchheimer coefficient C_F	0.026	0.036	0.020	0.038

5.3.1.2. Prediction models for the modified friction factor

As Eq. (5.6) shows, the modified friction factor ($fD_a^{1/2}$) of different lattice structures can be predicted by the values of permeability based Reynolds number Re_K and Forchheimer coefficient (C_F). The analytical prediction models for BCC, FCC-Z, FCC-XY, and octet-truss lattice structures were summarized as Eq. (5.12).

$$\begin{aligned} fD_a^{1/2} &= \frac{2}{\mathrm{Re}_K} + 0.052 \\ fD_a^{1/2} &= \frac{2}{\mathrm{Re}_K} + 0.072 \\ fD_a^{1/2} &= \frac{2}{\mathrm{Re}_K} + 0.04 \\ fD_a^{1/2} &= \frac{2}{\mathrm{Re}_K} + 0.076 \end{aligned} \tag{5.12}$$

Figure *5.3* visually shows the relationship between the value of $fD_a^{1/2}$ and the value of Re_K. It was found that as the increase of Re_K, namely either permeability or air velocity increased (the definition of Re_K), the value of $fD_a^{1/2}$ decreased, which illustrated the more fluid can be transmitted by the lattice structure. The value twice as the value of Forchheimer coefficient was the lower bound of the modified friction factor.

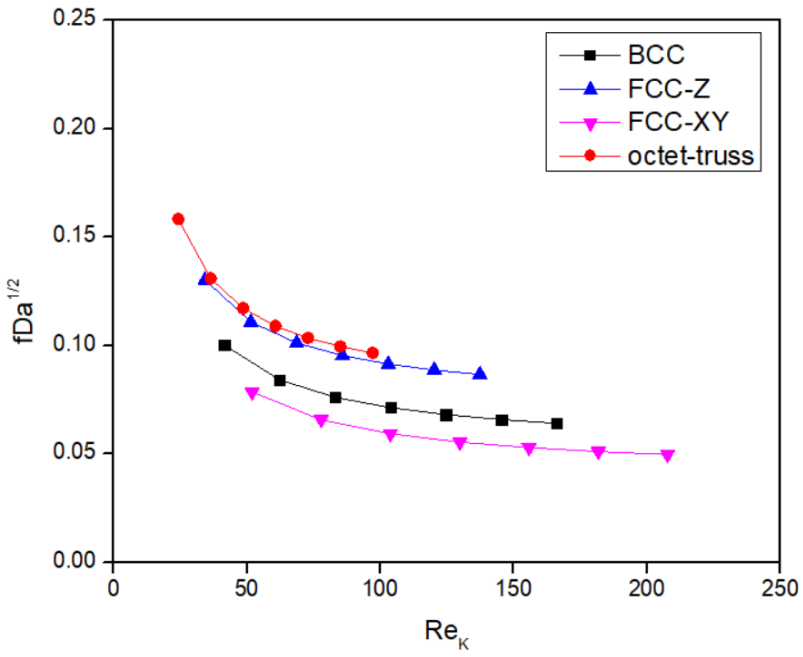

Figure 5.3. The relationship of $fDa^{1/2}$ over modified Reynolds number Re_K

5.3.2. Thermal characteristics

5.3.2.1. Channel hydraulic diameter based Nusselt number

In Eq. (5.7), The flow channel hydraulic diameter based heat transfer coefficient (h_c) can be considered as the average heat transfer coefficient. The h_c value and its related Nusselt number (Nu_c) can be taken as the general heat transfer coefficient and Nusselt number to evaluate and compare the heat convection capability of different lattice structures. Figure *5.4* shows the change of channel hydraulic height based Nusselt number (Nu_c) over different air flow velocities. It was found that as the velocity value increased, the Reynolds number (Re_c) and heat transfer coefficient (h_c) increased accordingly. Consequently, the convective heat transfer efficiency in the lattice structures was enhanced.

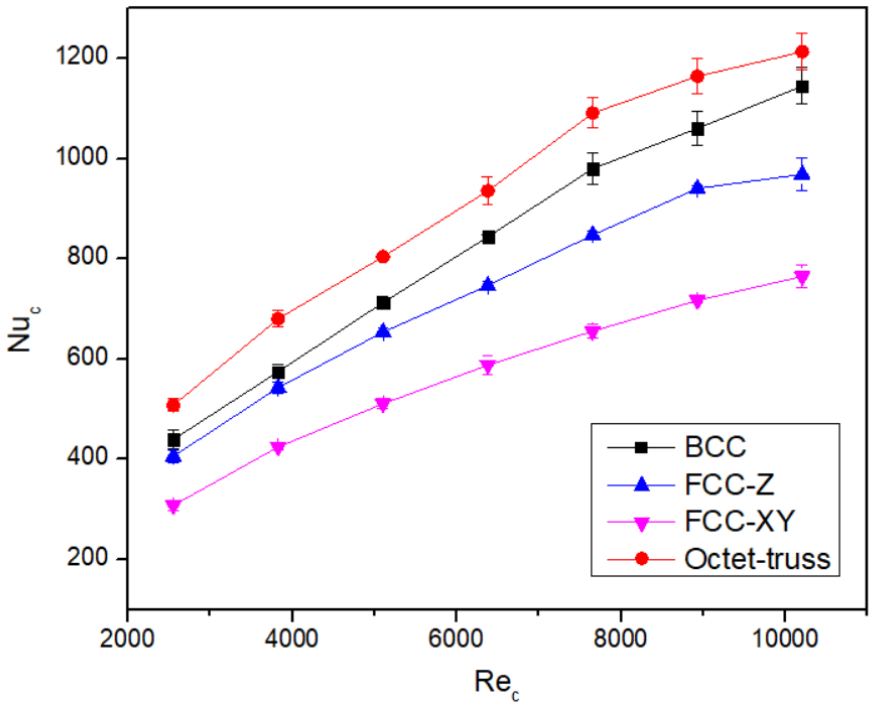

Figure 5.4. Channel hydraulic diameter based Nusselt number of different lattice structures

It was also found that for each kind of lattice structure, the channel hydraulic diameter based Nusselt number (Nu_c) increased with the incremental of the air velocity. Among different types of lattice structures, the octet-truss lattice structure always had the largest Nu_c value, followed by BCC and FCC-Z lattice structures, the FCC-XY lattice structure performed the worst convective heat transfer capability. It can be concluded that the convective heat transfer properties are affected by the combining effect of interfacial surface area and open area ratio. The air flow transmitted through the lattice structure with lager open area ratio easily, in which not too many local high speed turbulence flows were accelerated at the void volume along the flow direction. But for the structure has the smaller open area ratio, the relatively large induced flow resistance weakened the straightened flow entering from the lattice structure inlet end, the weakened flow also impinged, bounced, and diverged from the interfacial surface. In this condition, the larger interfacial surface area resulted in more flows with chaotic directions formed the

high speed turbulence flows around the nodes, which accelerated the flow passing through the void volume along the flow direction , and finally contributed to the higher convective heat transfer rate.

5.3.2.2. Convective heat transfer rate

As Eq. (5.11) shows, the convective heat transfer rate (η) was used to evaluate the utilization rate of the heat convection on the total heat. In this study, the total heat generated from the cartridge heaters was set as 4 W, therefore the magnitude of η was determined by the combined effect of air velocity value and the temperature difference between the inlet and outlet. Figure 5.5 summarized the convective heat transfer rate of different typed lattice structures under the air velocity ranging from 2 m/s to 8 m/s.

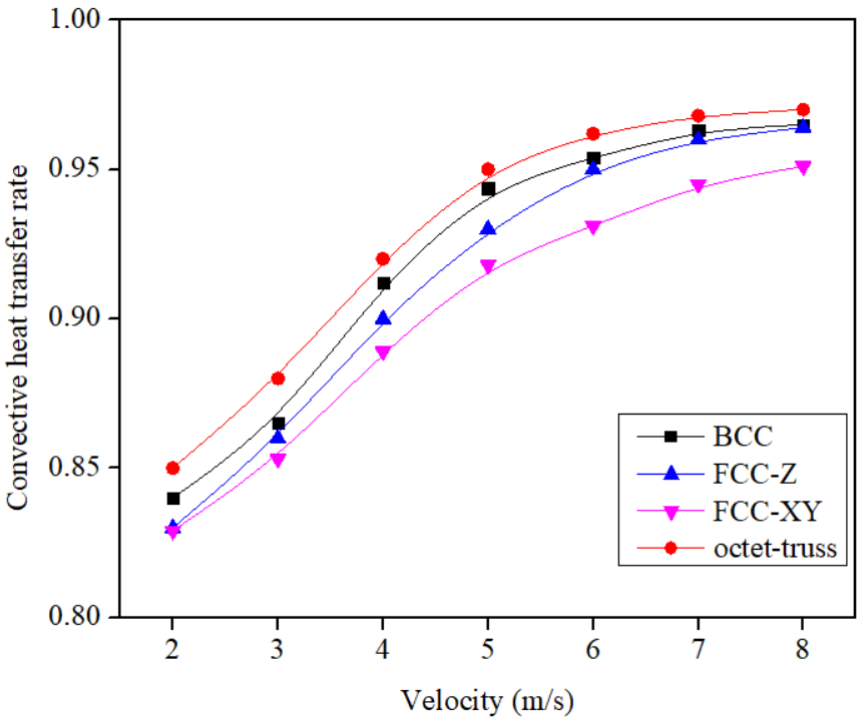

Figure 5.5. Comparisons of convective heat transfer rate of different lattice structures

As the η value expressed the percentage of heat transferred by the heat convection accounts for the total heat from the heater. It was found the air forced convection in the

octet-truss lattice structure utilized the largest percentage of total heat, then BCC lattice structure, then FCC-Z lattice structure, and FCC-XY still performed the worst. It was also found that the η value increased as the incremental of the air velocity increased. This phenomenon illustrated that as the air velocity increased, the larger volume of air was used for transmitting the heat during the unit time, which resulted in more heat was transferred by the convective heat transfer. Considering the total heat was transferred through the heat convection, heat conduction, and heat loss. It can be concluded that increasing the air flow velocity strengthened the heat convection process, meanwhile the heat loss to the ambient and the heat conduction processes were weakened.

5.3.3. Validation of experimental results

5.3.3.1. Numerical model

For validating the effectiveness of the experimental results and visually investigate the thermal and fluid motion in the lattice structure, a 3D numerical model was built in the software ANSYS FLUENT 20.1, the simulation domain and the coupled boundary conditions are shown in Figure 5.6. Considered the symmetry of the test sample, a half of the lattice structure core was defined as the solid domain. As the thickness of the lower and upper panel in the test sample was only 4 mm, they were neglected in the model. For the more stable simulation, besides the channel section fit the test sample, another two channel sections with a length of 25 mm were separately set and connected with the ends of lattice structure. In experiments, the air velocity value was set ranging from 2 m/s to 8 m/s, the range of corresponding Reynolds number was around 2500 to 10200. In this condition, the coupled air domain can be defined as the 3D, steady state, and incompressible turbulent flow.

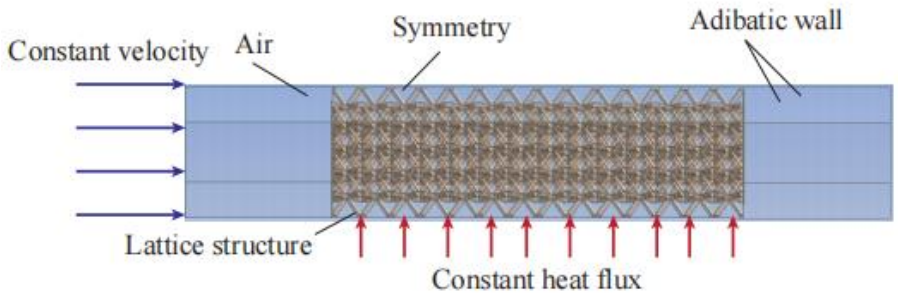

Figure 5.6. Simulation model for the steady-state convection process in lattice structure

The standard *k*- ε model was used to simulate the average flow characteristics under the turbulent flow conditions consistent with experiments. Except for the traditional conservation equations of mass, momentum, and energy, the standard *k*- ε model also solves the other two equations of turbulent kinetic energy (k) and dissipation rate (ε). Eq. (5.13) and Eq. (5.14) shows the simplified equations under the steady-state incompressible turbulence flow conditions.

$$\frac{\partial \rho \overline{V}_j k}{\partial x_j} = \frac{\partial}{\partial x_j}\left[\left(\mu + \frac{\mu_t}{\mathrm{Pr}_k}\right)\frac{\partial k}{\partial x_j}\right] + G_k - \rho\varepsilon \tag{5.13}$$

$$\frac{\partial \rho \overline{V}_j \varepsilon}{\partial x_j} = \frac{\partial}{\partial x_j}\left[\left(\mu + \frac{\mu_t}{\mathrm{Pr}_\varepsilon}\right)\frac{\partial \varepsilon}{\partial x_j}\right] + C_{\varepsilon 1}\frac{\varepsilon}{k}G_k - C_{\varepsilon 2}\rho\frac{\varepsilon^2}{K} \tag{5.14}$$

where μ_t is the viscosity, G_k is the product production of turbulence kinetic energy from the mean velocity gradients, $C_{\varepsilon 1}$ and $C_{\varepsilon 2}$ are constants, Pr_k and Pr_ε are the corresponding turbulent Prandtl numbers.

The unstructured polyhedral meshes were set on lattice structures, and the vicinity near the fluid-solid interface was refined for the better coupled fluid and heat transfer. Four sets of meshes were separately tested on the test sample containing BCC, FCC-Z, FCC-XY, or octet-truss lattice structure cores for checking whether the solutions are

independent from the number of meshing elements. The simulated pressure drop gradient values under different mesh densities were plotted for monitoring the mesh independency, as shown in Figure 5.7. It was found that for each test sample, the pressure drop gradient value almost didn't change at the second set of meshes. Thus, the correspondent meshes with 8 million, 6 million, 6 million, and 30 million elements were respectively used in the test samples with BCC, FCC-Z, FCC-XY, and octet-truss lattice structure cores, to spend reasonable computation resources and result in simulation results with the convincing accuracy, as shown in Figure 5.8.

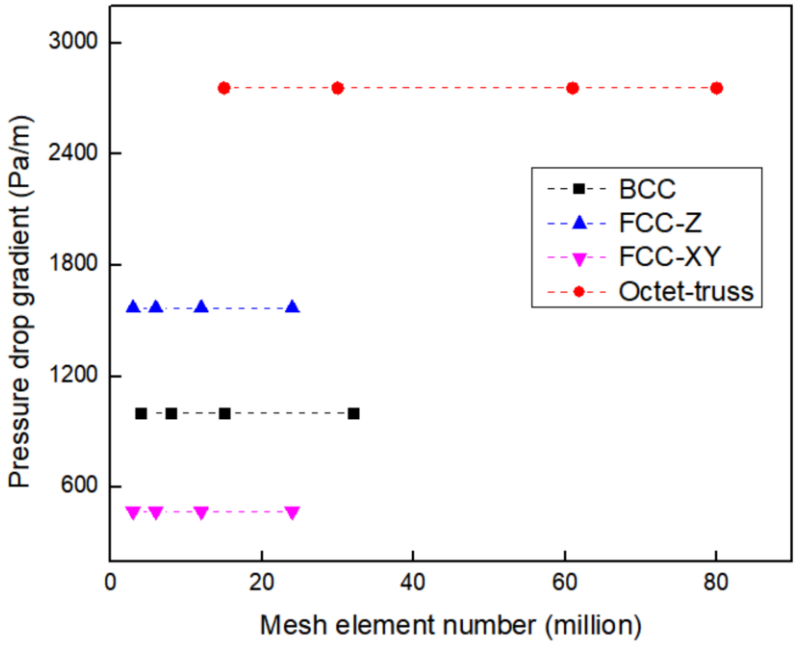

Figure 5.7. Mesh independence study for pressure drop gradient

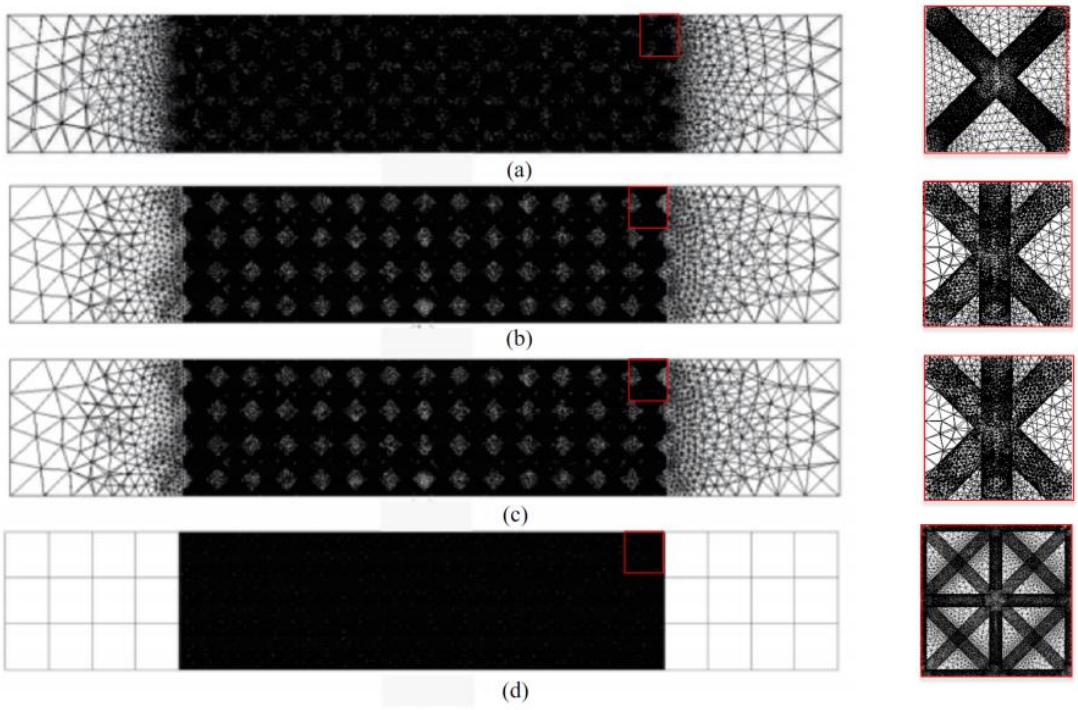

Figure 5.8. Cross-section view of meshes used in the heat convection simulation. (a) BCC, (b) FCC-Z, (c) FCC-XY, and (d) octet-truss lattice structure

5.3.3.2. Numerical results

Figure 5.9 shows the comparisons between the experimentally and numerically derived pressure drop gradient. It was found they fit well with each other, which supported the effectiveness of the repeated experiments. On the other side, the comparisons also validated the reliability of the numerical models, which can be used for further visually investigating the fluid motion and temperature distribution in different lattice structures and their coupled fluid domain.

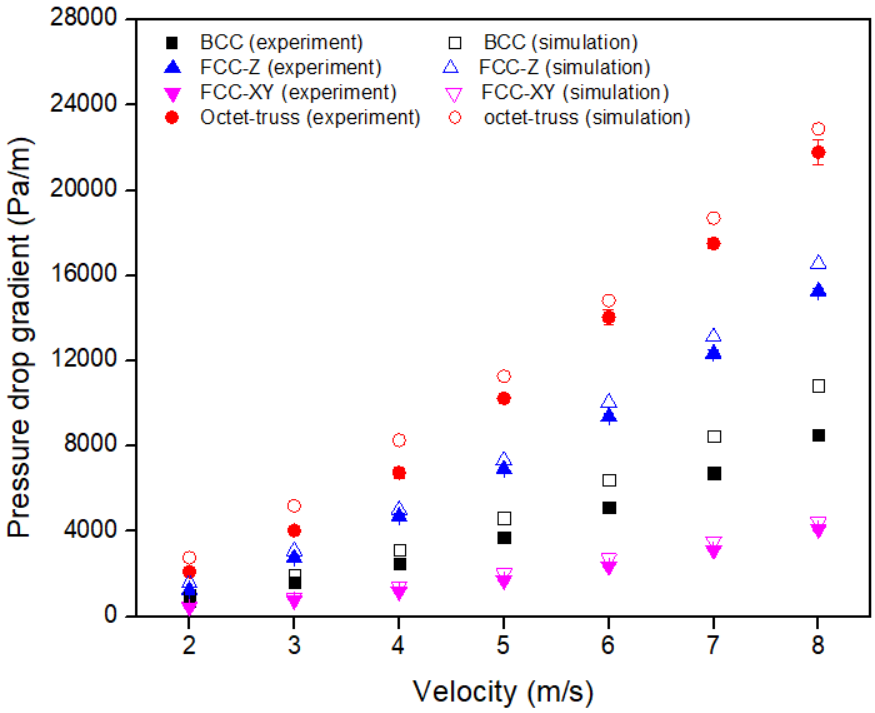

Figure 5.9. Comparisons of pressure drop gradients between experimental and numerical results

Figure 5.10 shows the temperature distributions in BCC, FCC-Z, and FCC-XY lattice structures under the air velocity value was set as 2 m/s. It can be found that the hot points always took place at the locations near the lattice bottom surface and the end of lattice structure near the outlet, which was caused by the combining effect of forced heat convection and conduction.

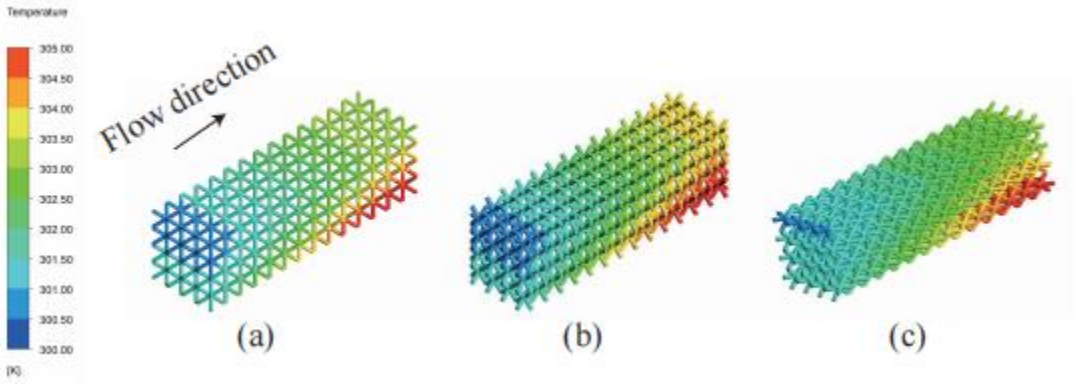

Figure 5.10. Simulated temperature contours of lattice structures. (a) BCC, (b) FCC-Z, (c) FCC-XY

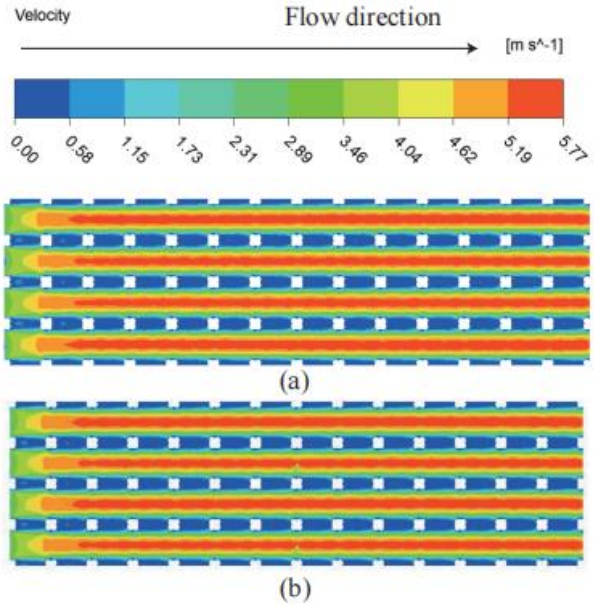

Figure 5.11. Velocity contours of BCC lattice structure coupled air under the velocity of 2 m/s. (a) symmetry plane, and (b) top view of the middle plane parallel to the lattice structure bottom surface

Figure 5.10 shows the velocity distributions on the symmetry plane and the middle plane parallel to the lattice structure bottom surface. It was found that although the existence of nodes and struts in the lattice structure generated the relatively large fluid resistance force, the air flow between the nodes was strengthened dramatically from 2 m/s to

around 6 m/s by the turbulence flows around the nodes and struts. This finding also supported the experimental results that the convective heat transfer capability was affected by the combing effect of open area ratio and interfacial surface area. The simulated velocity contours showed that lattice structure has the promising future in the application of heat exchangers in industry.

5.4 Summary

In this chapter, the air forced convection on the same porosity BCC, FCC-Z, FCC-XY, and octet-truss lattice structures was experimentally studied. Hydraulic and heat transfer characteristics were both investigated. In the hydraulic performance study, the pressure drop gradient, permeability, and Forchheimer coefficient. It was found that the FCC-XY lattice structure performed the best including the largest permeability, the smallest Forchheimer coefficient, and the lowest pressure drop gradient. Compared to porosity and interfacial surface area, the open area ratio was the dominant factor to determine the pressure drop and friction factor through the lattice structure. In the determination of heat transfer characteristics, the octet-truss lattice structure was expected to perform the best convective heat transfer capability due to its largest interfacial surface area and smallest open area ratio. It was also found as the incremental of the air velocity, the heat convection in the lattice structure was strengthened to dissipate more heat generated from the bottom heaters.

Chapter 6. Lattice structures in the conformal cooling channel design

6.1. Introduction

The overall requirement of cooling system design in the plastic injection molding is a compromise between short cooling time, uniform mold surface cooling, and lower pumping power needed [58]. Thanks to the development and application of metal three-dimensional printing (3D) printing, the optimization and fabrication of the conformal cooling channels (CCCs) in the plastic injection mold has been becoming the most effective solution to enhance cooling performance. In this chapter, for a specific plastic injection mold and its matched plastic product, three kinds of conformal cooling channels, namely the circular, tapered, and body-centred cubic (BCC) lattice structure filled tapered ones, were optimized separately for enhancing the cooling and hydraulic performance. The multi-criteria decision-making approach was employed to process the numerically derived parametric performance maps, then decided the optimized structural dimensions for different typed CCCs. The direct metal laser sintering (DMLS) method was then used to test the printability of the optimized designs. Finally, the thermal and hydraulic performance on the DMLS printed CCCs were experimentally studied for validating the effectiveness of numerical investigations.

6.2. Design of CCCs in the plastic injection mold

6.2.1. The mold with straight-drilled cooling channels

Figure 6.1 shows the components in the plastic injection molding machine, including the plastic part, runner, main and auxiliary cooling channels, as well as the mold with internal straight-drilled cooling channels. In this study, the location and structural dimensions of auxiliary channels were fixed during the design and optimization of the CCCs. The newly designed CCCs were placed at the location of the straight channels shown in in Figure 6.1 (b).

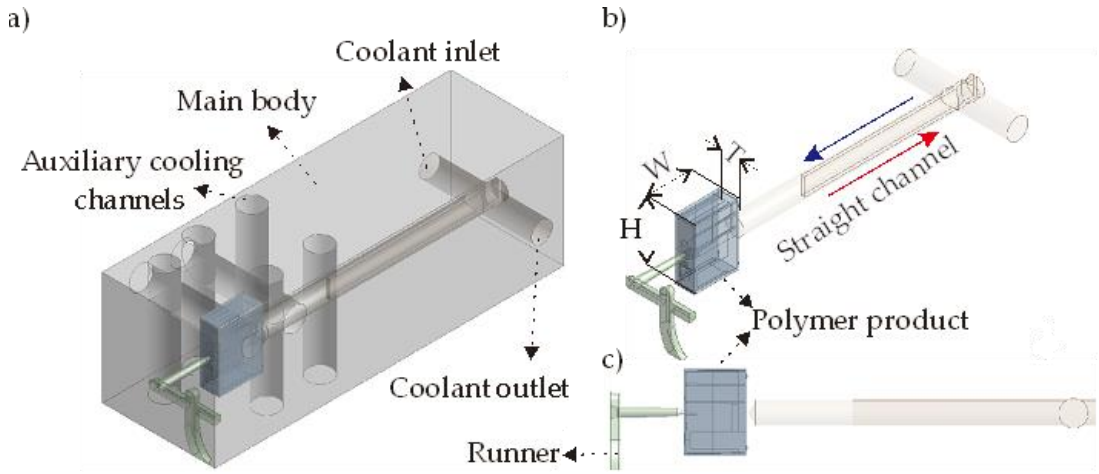

Figure 6.1. Design of the straight-drilled cooling channel. (a) isometric view of the plastic injection molding system, (b) isometric view of the straight channel, polymer product, and runner; and (c) side view of the straight channel, polymer product and runner.

The straight-drilled cooling channels were manufactured by the traditional method, which was used as a baseline design for comparing with the complicated structured conformal cooling channels fabricated by the DMLS technology. Based on the summarized data from the industrial partner, the bulk dimension of the polymer product is 14×20×6.5 mm^3, and it was made from polybutylene terephthalate (PBT) with the density of 1396 kg/m^3, the specific heat of 1363 J/kgK, and the thermal conductivity of 0.29 W/mK [93]. Besides, the raw material of the injection mold is steel with the density of 8030 kg/m3, the specific heat of 502.48 J/kgK, and the thermal conductivity of 16.27

W/mK [78]. The fluid-phase plastic was injected into the cavity near the mold with an initial temperature value of 543 K, and finally ejected from the plastic injection molding machine with a final temperature value of 323 K. The cooling time of 7s was tested by the industrial partner. This set of industrially measured data was used for determining the material properties and boundary conditions in the later computational simulations. The cooling time consumed by the straight-drilled channel design was also used as a reference value to check the cooling efficiency of the optimized CCCs.

6.2.2. The mold with circular shaped conformal cooling channels

Rather than straight-drilled channels, the pathways of CCCs were designed to follow the mold outer profiles as close as possible, which contribute to the more efficient heat dissipation. The focus of this study is to balance the circular CCCs hydraulic and cooling performance by enlarging the channel diameter and embedding lattice structures inside. In this study, the molds with CCCs share the same plastic injection molding system shown in Figure 6.1. Figure 6.2. shows the design of circular CCCs with a U-shaped pathway. The cross-section of the circular CCCs is a circle with the constant diameter value (D), and the smallest distances between the channels and mold outer surfaces were defined as wall thicknesses (k, l, and m). In this study, considering the manufacturing limitations of DMLS machine to fabricate the overhang structures and thin walls, the channel diameter (D) value was adjusted from 2.1-2.5 mm, and the wall thicknesses were set as: k=l=3 mm, and m=5 mm. The reason for the m value is larger than k and l values is that its correspondent channel section is close to the mold outer surface with the largest area. The largest surface area and the direction parallel to that of gravity contributes to the highest cooling efficiency on the mold surface corresponding to the m

value. Hence, the setting of larger valued m guarantees the better temperature uniformity among different mold surfaces.

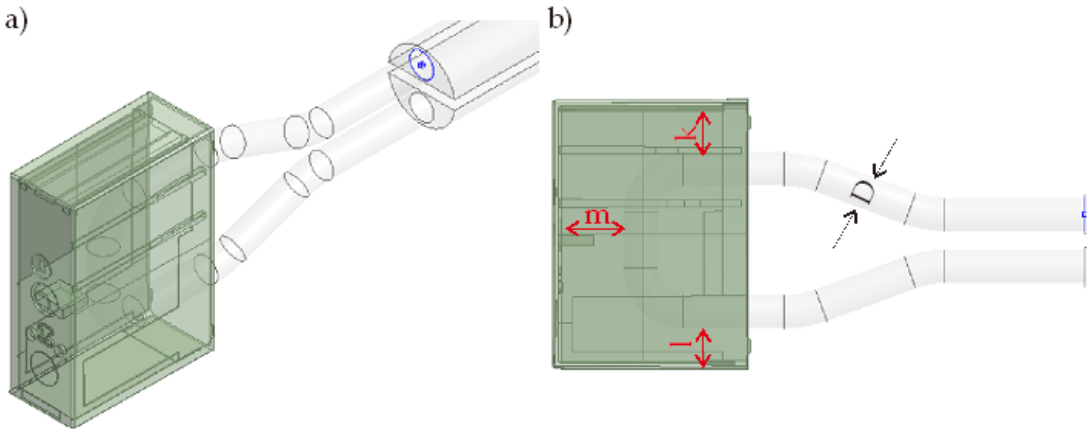

Figure 6.2. 3D view of the circular CCC. (a) isometric view and (b) side view.

6.2.3. The mold with tapered conformal cooling channels

Figure 6.3 (a) show the design of tapered CCCs. It can be seen that the cooling channel diameter was enlarged gradually from D_1 to D_2 along the center line of pathway. The advantages of the tapered CCCs designs are: the enlarged channel diameter result in larger contact surface area for the cooling water, and the pressure change in the tapered CCCs is much smaller than the step design which increases the channel diameter suddenly.

For easier comparisons between different CCCs designs, the pathways of tapered CCCs are the same as the ones in circular CCCs. Besides, the value of the channel inlet or outlet diameter (D_1) has a similar range of 2.1- 2.5 mm to the diameter (D) value of the circular CCCs. The largest channel diameter value (D_2) was adjusted from 3 to 4 mm in the computational simulation, so as for deriving the parameters contributing to the balanced minimum cooling time, minimum temperature nonuniformity, and minimum pressure drop via the multi-criteria decision-making approach.

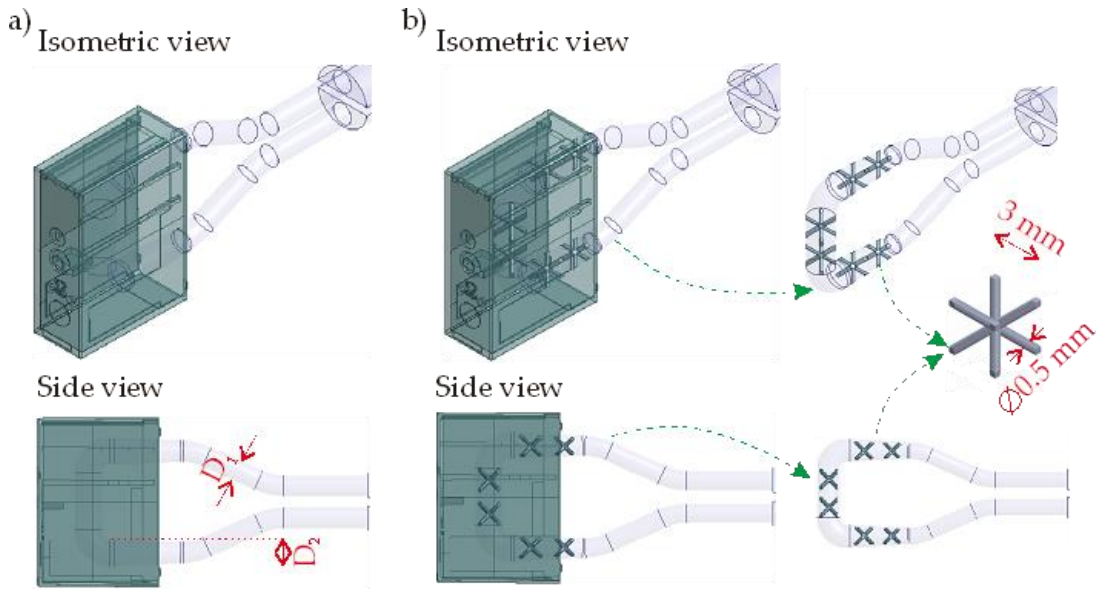

Figure 6.3. 3D views of the tapered CCCs. (a) tapered, and (b) BCC filled tapered ones

6.2.4. The mold with BCC filled tapered conformal cooling channels

The previous thermal studies were used to theoretically investigate the heat transfer characteristics of different lattice structures. In this study, the lattice structure was applied in the design of CCCs, so as to further investigate the feasibility of using the lattice structure to enhance the cooling efficiency of CCCs in industry. Figure 6.3 (b). shows the tapered CCCs embedded with six BCC lattice structures. Herein, the integrated BCC lattice structures increased the larger contact surface area for the convective heat transfer. Besides, the component struts linked the surfaces of CCCs laterally or transversely, which enhanced the heat conduction as well. However, the addition of BCC lattice structures would result in the protentional pressure drop increase. In this condition, the multi-criteria decision-making approach was fully utilized to find a trade-off point that can maximize the cooling efficiency and keep the pressure drop at a reasonable value at the same time.

6.3. Computational Model

The focus computational simulations was to simulate the cooling process of the polymer and its adjacent mold. A three-dimensional (3D) transient conjugated heat transfer model was employed, and the governing equations of mass, momentum, and energy were listed in Eq. (6.1)-Eq. (6.3).

$$\nabla \cdot \vec{\boldsymbol{V}} = 0 \tag{6.1}$$

$$\rho\left(\frac{\partial \vec{V}}{\partial t} + \vec{\boldsymbol{V}} \cdot \nabla \vec{\boldsymbol{V}}\right) = -\nabla p + \mu \nabla^2 \vec{\boldsymbol{V}} \tag{6.2}$$

$$\rho C_p \left(\frac{\partial T}{\partial t} + \vec{\boldsymbol{V}} \cdot \nabla \boldsymbol{T}\right) + \nabla \cdot (-\lambda_c \nabla T) = 0 \tag{6.3}$$

where $\vec{\boldsymbol{V}}$ and ρ is the velocity vector and the density of the coolant (water, *t* is time, *p* is pressure term, μ is the dynamic viscosity of the coolant (water), λ_c is is the thermal conductivity of the coolant, and C_p is the heat capacity. It is worth noting that the current model does not take the polymer flow into the account so that its control volume starts with the transferred heat from the polymer to the mold body. In the case of polymer flow considerations, viscoelasticity-related terms of relevant polymer flow must be added to the governing equations below. Besides the computational solution of the coolant in the mold, there is also a transient heat transfer inside the mold (stainless steel) body via conduction. Thus, it is solved using the energy equation given in Eq. (6.4).

$$\rho_s C_{p_s} \frac{\partial T}{\partial t} + \nabla \cdot (-\lambda_s \nabla T) = 0 \tag{6.4}$$

where ρ_s, Cp_s, and λ_s are the density, heat capacity, and thermal conductivity of the mold body. After defining the governing equations required for solutions of the computational model, the meshing process is completed via tetrahedral mesh that minimizes the number of mesh compared to other types. The mesh view of the solution model is shown in Figure 6.4.

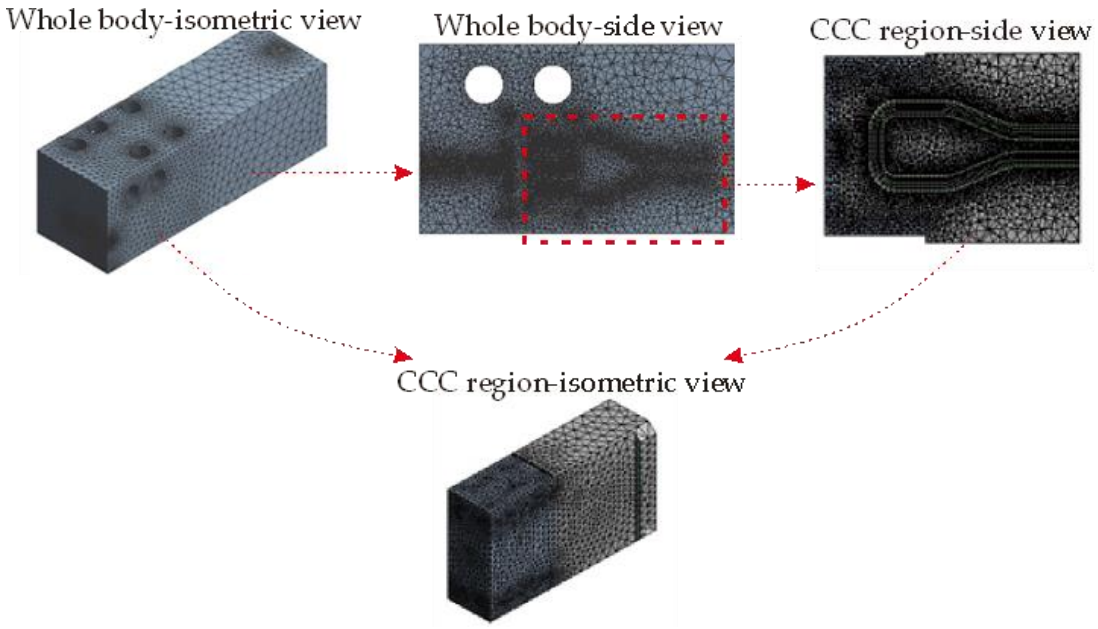

Figure 6.4. Mesh views of the conformal cooling channels via isometric and side views.

Even though the whole body is used in the meshing step, we focus on the CCC region. For mesh independence, seven different mesh sizes are investigated between 0.4 million to 2 million. Also, four different time-step values are compared for the time-step independence. Figure 6.5 projects the independence check for meshing and time-step.

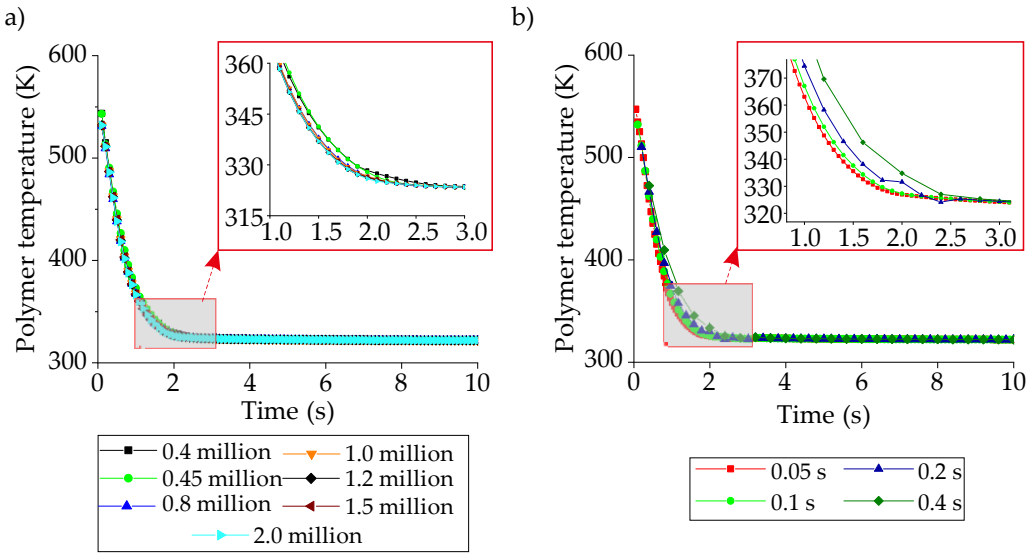

Figure 6.5. Independency of (a) mesh structure and (b) time-step.

The mesh independency results show that the mesh size of 1.2 million has very close trends with the mesh sizes of 1.5 and 2 million so that the independence is assumed to be achieved at the mesh size of 1.2 million. The time-step independence is provided with the time-step of 0.1 s as it coincides with the time-step of 0.05 s. Since all the boundary and initial conditions are the same for different types of CCCs, the same time-step value and similar mesh sizes are used in all simulations. The boundary conditions are; i) the coolant inlet and outlet conditions are velocity inlet and pressure outlet, respectively, ii) the mold surfaces contact with the plastic are defined with the coupled boundary conditions, iii) the walls of the CCCs inside the mold geometry are defined with the convective boundary conditions, iv) the SIMPLEC algorithm is used for the pressure-velocity coupling, and v) the energy and momentum equations are discretized using the second-order upwind scheme.

The thermal model aims to measure three objectives that are i) cooling time, ii) temperature non-uniformity, and iii) pressure drop. Using the computational simulations, the cooling time is determined as the time from the injection temperature (543 K) to the ejection temperature (323 K). The temperature non-uniformity is the standard deviation of the plastic temperature as the surface as defined in Eq. (6.5) and Eq. (6.6) below.

$$\sqrt{\frac{\sum_{i=1}^{n}(T_i - T_0)^2}{n}} \tag{6.5}$$

where T_i and T_0 are the cell temperature value (at each facet) and the mean temperature value, respectively, whilst the term n is the number of facets in the model;

$$T_0 = \frac{\sum_{i=1}^{n} T_i}{n} \tag{6.6}$$

Regarding Eq. (6.5) and Eq. (6.6), a smaller standard deviation means that the non-uniformity is smaller because the temperature distribution is better. Therefore, the main

purpose is minimizing the temperature non-uniformity whereas the minimizations of the cooling time and pressure drop are aimed as well. The pressure drop is calculated between the pressure values at the inlet and outlet regions.

The last step of the completion of the computational model is the experimental verification. The modelled cooling time of the straight-drilled channel was compared against experimental data of the straight-drilled channel obtained previously (as a cooling time of 7.0 s). An average relative difference of 7.14% was deemed acceptable for our 3D transient heat transfer studies. Apart from the computational thermal model, the mechanical strength can also be analyzed via computational mechanical simulations. Since the mechanical strengths were analyzed for the proposed mold geometry in our previous works [78,81,82], we do not mention them in this work.

6.4. Metamodel Development

Computational simulations provide numerical performance output for the objectives (cooling time, temperature non-uniformity, pressure drop). Each computational effort presents numerical results for a specific parameter set (e.g., a single value for each coolant temperature, volume flow rate, and diameter (or cross-sectional dimensions)). However, it is a fact that parameter sets create a design space for each CCC design so that a huge effort is required to define the general characteristics of the cooling performance (according to the defined objectives) between the lower and upper boundaries of the design space. Lower and upper boundaries can be defined as the minimum and maximum values of parameters, but multiple parametric sets should be defined with quantitative data using computational simulations. Hence, a designer (engineer, operator, etc.) who is fully or partially responsible for the entire process in Figure 1, should decide the number of computational solutions to define multiple

parametric set points in the design space. There is a trade-off at this point; a higher number of computational simulations provides more quantitative data in the design space while it also results in higher computational time, cost, and labor. To balance the pros and cons, metamodels are widely used in this step. That is to say, several numbers of computational simulations are performed and thereby sufficient number of quantitative data can be obtained in the design space. After that, metamodel approaches are used to generate the overall performance trends (characteristics) of the objectives in the design space. To this end, a performance map for each objective can be created in the design space and the numerical values of the performance map can be used as the initial solution matrix during the multi-criteria decision-making step. Figure 8 illustrates the development of the metamodel from the design step to the final performance map using an imaginary scenario with two parameters for an objective. It is worth noting that this study has 3D design spaces (via three parameters; coolant temperature, volume flow rate, diameter/cross-sectional dimensions) for three different objectives which are pressure drop, cooling time, and temperature non-uniformity.

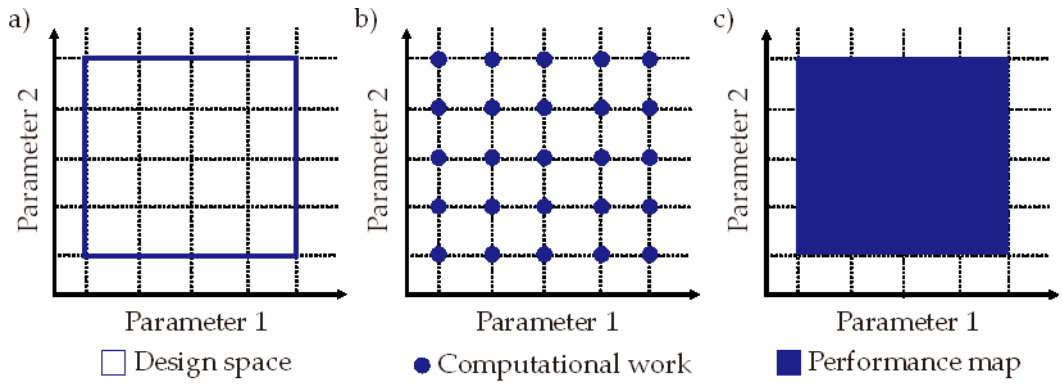

Figure 6.6. Illustrations of the metamodel development; a) design space, b) computational simulations, and c) performance map.

For the circular and serpentine CCC designs, the metamodel was developed using MATLAB traditional interpolation approach [34,38] whereas the metamodel of the tapered (and BCC-integrated tapered) CCCs was developed via both MATLAB traditional interpolation and the neural network [35].

6.5. Multi-criteria Decision Making

Multi-criteria decision making is a crucial step for selecting the most convenient option of the proposed CCCs as there are three different objectives. All objectives are aimed at their minimum values, but it is a fact that their performance maps generated by metamodels might not be in parallel to one another. That is, a continuous change in a target parametric set can provide decreasing trends for an objective while resulting in an increment for another objective. The multi-criteria decision making allows us to determine the most convenient case amongst different performance trends of the objectives. There are several approaches for multi-criteria decision making like using graphic tools, interpolative approaches, etc. Optimization is a preferred technique for decision making in the plastic injection industry [83,84], and its multiobjective procedure makes the decision making a multi-criteria framework. In this study, we prefer using the multi-objective optimization approach using the MATLAB Optimization Toolbox.

The multi-objective optimization procedure is solved via Pareto frontier plot that consists of all the objectives between their lower and upper bounds. After creating a performance map for each objective, the objectives are brought together to quantitatively define the feasible solution region, which simply means the accumulation region of the parametric sets according to the lower and upper bounds of the objectives. Regarding the purpose of optimization (minimization or maximization) and the defined

weightage values, the most convenient optimal point(s) can be found. In this study, we have three objectives so that the feasible solution region is a 3D region that is limited by the minimum and maximum values of the calculated objective values. As the main purpose is minimization for all objectives, we focus on the best trade-off point that is defined by aiming at the minimum values of objectives. It must be noted that the multiobjective optimization solution becomes easy to handle if the performance maps of objectives have parallel trends to one another. However, in the case of opposite performance trends (like in this study), the decreasing trends of objective results in an increasing trend for another objective so that the weightage value becomes critical during the decision-making step. Following this fundamental, the multiobjective optimization procedure is applied in three main steps. The first step is generating the borders of the feasible solution region via the Pareto frontier plot in the MATLAB toolbox. This is an automated process of the MATLAB after giving input of the objective functions, constraints, lower & upper bounds. The genetic algorithm recognizes the performance map of each objective as the initial population; and then, creates the feasible solution region via the Pareto frontier. The second step is normalizing the objective function values by using the utopia and pseudo-nadir points as shown in Eq. (6.7).

$$f^*(x) = \frac{f(x) - f^U(x)}{f^{PN}(x) - f^U(x)} \tag{6.7}$$

where $f(x)$ is the value of the objective in the Pareto frontier; $f^*(x)$ is the normalized value of $f(x)$; $f^U(x)$ and $f^{PN}(x)$ are the utopia and pseudo-nadir points of the Pareto frontier. The utopia point, $f^U(x)$, is the value point in the plot where all objectives have their minimum values. However, this point is not in the feasible solution region because there is no feasible solution for the optimization when all the values go to their minimum

values since they have opposite trends in one another in the current problem. Contrary, the pseudo-nadir point means the point of the most undesired values (maximum values in this problem) in the feasible solution region. It is noted that the $f^{PN}(x)$ stays in the feasible solution region unlike the $f^{U}(x)$. Also, the nadir point, $f^{N}(x)$, which is mentioned neither in Eq. (6.7) nor in the general solution, is the point where the maximum values of objectives outside of the feasible solution region. The normalization procedure is applied via $f^{U}(x)$ and $f^{PN}(x)$ in this work. However, in case of maximization purpose for all objectives, the term $f^{N}(x)$ could have been considered in the normalization step.

Since all objectives aim minimization in the solution procedure, the weightage of objectives is significant. Hereby, we are able to determine the best trade-off point using the Pareto frontier plot data. After completing the normalization, the weightage values are defined as ω_{ct}, ω_{tn}, and ω_{pd} for the objectives of cooling time, temperature non-uniformity, and pressure drop, respectively. The impact of weightage is calculated using the weighted-sum (WS) approach as shown in Eq. (6.8),

$$WS = f^{*}(x)_{ct} \cdot w_{ct} + f^{*}(x)_{tn} \cdot w_{tn} + f^{*}(x)_{pd} \cdot w_{pd} \tag{6.8}$$

The WS is one of the weightage analysis approaches and we prefer it in this study. However, other approaches like weighted-product (WP) can be applied as well. The choice of the weighting approach depends on the decision-maker.

6.6. Fabrication of molds with CCCs

6.6.1. DMLS process parameters

The commercial 3D printing system M100 (EOS GmbH) using the DMLS technology was employed to fabricate maraging steel MS1 injection molds in this study. The diagonal laser scanning method was used in the fabrication of injection molds. To

quantify the energy input per volume of melted powders, the comprehensive indicator of laser energy density was introduced. Laser energy density function is determined by all laser system parameters, as shown in Eq. (2.1) in Chapter 2. In this study, the energy density was varied to print the mold with BCC-filled tapered channel for determining the best combination of laser system parameters. The scan spacing and layer thickness were set as constants of 0.06 mm and 0.02 mm respectively. The power and scan rate of laser were changed. Using previous experience on printing stainless steel SS 316L parts, the details of study on power and scan rate effects are listed in Table 6.1.

Table 6.1. The set of printing parameters.

Sample	A	B	C	D	E
Laser power (W)	$0.5P_0$	P_0	$2P_0$	$2P_0$	$2P_0$
Scan rate (mm/s)	u_0	u_0	u_0	$0.8u_0$	$0.67u_0$
Energy density factor	0.5	1	2	2.5	3

Note: P_0 and u_0 are the parameters for printing SS 316L parts, which used as baseline for investigating printing parameters for MS1. Herein, P_0 represents 60 W, and u_0 represents 1594 mm/s.

Using the parameters listed in the table, the DMLS processed samples are shown in Figure 6.7. It is obvious that only sample C was printed successfully. The laser power of 120 W, the scan rate of 1594 mm/s were combined and used for printing all molds in this study.

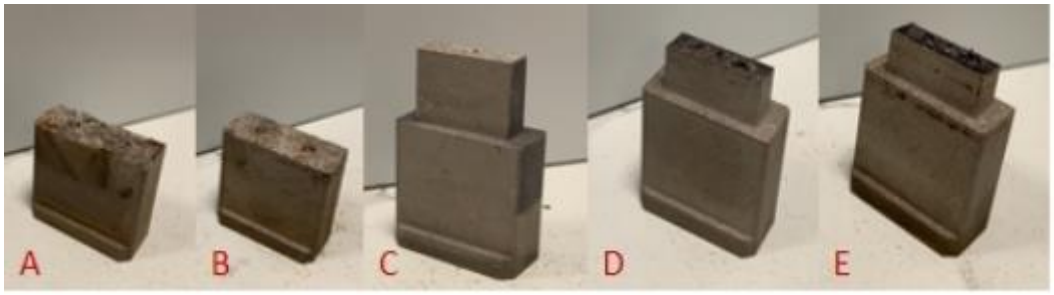

Figure 6.7. DMLS processed samples using different laser system parameters.

6.6.2. Printability validation

Thanks to the parametric study of the DMLS process, molds with different typed conformal cooling channels were fabricated successfully via the M100 machine, and all of them have a flawless appearance. As the focus of this project is internal channel design, the X-ray computed tomography (CT) scanning methodology was used to exhibit the real geometries of internal cooling channels, to validate the printability of different designed channels.

X-ray computed tomography (CT) is one of the non-destructive (NDT) techniques that can measure internal geometric features of 3D printed parts. The X-ray CT measurement process can be summarized as the sequence of emitting a cone-beam of X-rays through the tested sample, generating projections based on the intensity of X-rays falling on the detector, calculating 2D CT images from projections, and stacking multiple 2D CT images into the 3D ones. The schematic of the X-ray CT scanning system is shown in Figure 6.8.

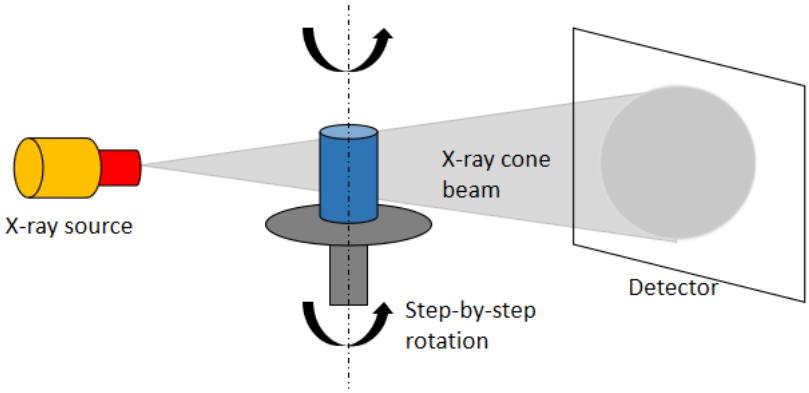

Figure 6.8. Schematic of X-ray CT scanning system.

In this project, the voltage and current of the X-ray source were set as 450 kV and 0.7 μA separately. The spatial resolution of the scanned image was 0.05 mm. The acquisition interval was set as a constant rotation step of 0.9°. In total, four hundred 2D CT images were calculated and then reconstructed into the CT image of the 3D volume. The software VGStudio MAX 3.4 (Volume Graphic GmbH) was used to visualize the internal channels.

6.7. Experiments

6.7.1. Introduction

In the injection molding process, the final plastic product is very thin with several tenths of millimeters, and the plastic changes its form from the fluid phase to the solid phase throughout the cooling cycle. To experimentally investigate the cooling performance of different channels at several continuous cycles, the high temperature silicone oil DPDM-400 (Clearco Products Co., Inc.) was used to replace hot fluid phase plastic. Besides, the volume of silicone oil cooled down in one cycle was also enlarged beyond that of the plastic product in order to perform better experimental results. The details of the experimental setup are elaborated on below.

6.7.2. Experimental setup

Figure 6.9. depicts the schematic of the experimental setup used to test the cooling performance of three types of optimized channel designs in the mold, i.e.circular, tapered, and BCC filled ones. From left to right, the setup is composed of three parts: the cooling system, the test module, and the hot oil loop.

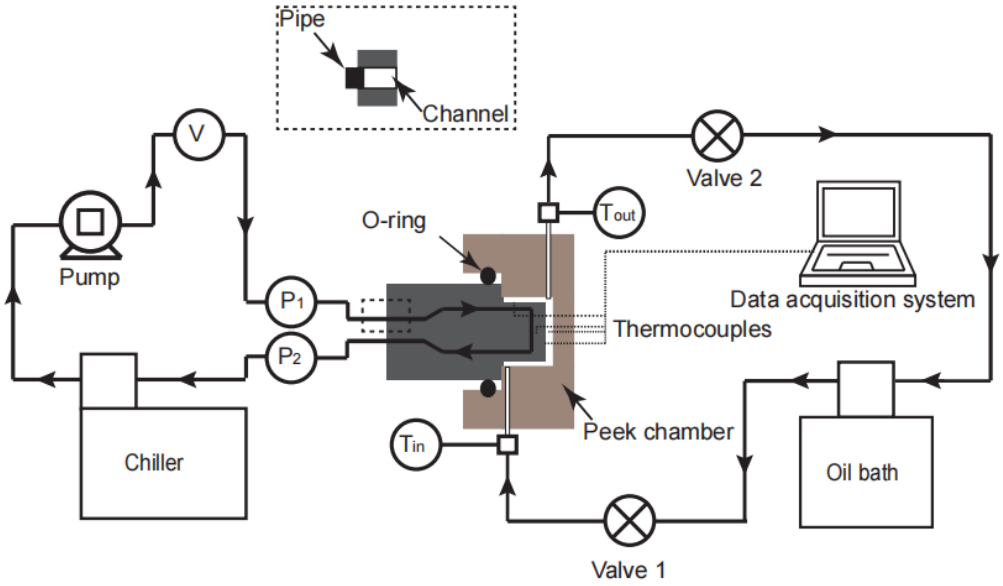

Figure 6.9. Schematic of the experimental setup for the CCCs performance test

In the cooling system, a gear pump (Model 75211-15, Cole-Parmer Instrument Co., Inc.) drew cooling water with a constant temperature of 293K from a chiller (Model AP 15R-40, Polyscience Solutions Co., Inc.). The cooling water was supplied to the product from the inlet point, then was circulated through the conformal cooling channel in DMLS processed mold, finally flushed back to the chiller. Hereby, a cooling loop was operated during the experiments. A flowmeter was used to monitor the flow rate of inlet cooling water, and the pressure values of inlet (P1) and outlet (P2) were measured by two pressure gauges. In the hot oil loop, opening two valves at the inlet and outlet of the oil bath (Model CC 308, Huber Co., Inc.), the hot silicone oil with a constant temperature value would flow from the oil bath into the test module, then back to the oil bath.

The experiment chamber in the test module was made from PEEK (polyetheretherketone), which can endure a high temperature up to 533K and has a relatively low thermal conductivity of 0.25 W/m·K. For performing better cooling experimental results and reducing operation difficulties, the internal cavity (for storing silicone oil) volume was enlarged to 25.5×11×16.5 mm^3. The 'insert' part of DMLS processed mold was inserted into the internal cavity of the experiment chamber and fixed by an O-ring. In experiments, the insert directly contacted with the silicone oil in the chamber.

In the test module, Two K-type thermocouples (T_{in} and T_{out}) were inserted into the inlet and outlet of silicone oil separately. Besides, in the oil chamber, other four K-type thermocouples (T_{top}, T_{side}, T_{front}, and $T_{int.}$) were inserted into the coupled volume of insert and oil, as shown in Figure 6.10. Herein, $T_{int.}$ (int.: interior) was placed at the centre of the oil between the insert front and the chamber right surface. The average of measured T_{in}, T_{out}, and $T_{int.}$ values were used as the silicone oil temperature (T_{oil}) in experiments. T_{top}, T_{side}, and T_{front} were inserted on the top, side, and front surface of the insert.

Account for the symmetry of conformal cooling channel in Mold sample, the use of T_{top}, T_{side}, and T_{front} was good enough to monitor temperatures of insert surfaces contacting the silicone oil. Besides, as the thermocouples can be seen as cylinders with a diameter of 0.3 mm, the number of them should be controlled to minimize the effect in the silicone oil volume. As Figure 6.10 shows, in the Mold 1 test module, T_{top}, T_{side}, and T_{front} were all placed at the symmetry axis of the insert surface, as well as in the plane along with the channel centre path. The remarkable characteristic of T_{top}, T_{side}, and T_{front} locations is that none of them were the centre of the insert surface, but they were all facing a piece of complete conformal cooling channel in order to guarantee the measured temperature

values that can reflect the channel design induced cooling performance in different surfaces.

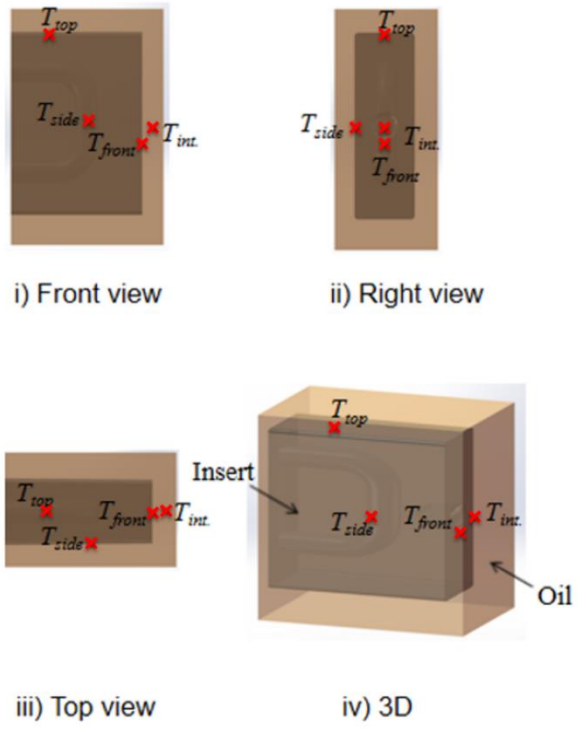

Figure 6.10. Locations of thermocouples in the oil chamber

6.7.3. Experimental procedures

Using the above-mentioned setup, the experimental procedures can be summarized as follows:

1) Closing Valve 1 and Valve 2; using the oil bath to heat the silicone oil to a constant temperature of 493.15 K (220°C), cooling down the water in the chiller to a constant temperature value of 293.15 K (20°C); Setting the flow rate of cooling water as 0 (zero).

2) Starting to record instant temperature values of T_{top}, T_{side}, T_{front}, T_{in}, T_{out}, and $T_{int.}$; Opening Valve 1 and Valve 2; Calculating T_{oil} (the average of measured T_{in}, T_{out}, and $T_{int.}$ values); Closing Valve 1 and Valve 2 as soon as the instant value of T_{oil}

reaches 493 K, as well as adjusting the flow rate of cooling water to a constant value; Recording pressure values of P_1 and P_2.

3) Closing Valve 1 and Valve 2 when the instant value of T_{oi} decreases to 323 K, as well as decreasing the flow rate of cooling water to 0 (zero).

4) Repeating 1) to 3).

In this project, the cooling performances of the molds were tested in the flow rate range of 0.1-0.4 L/min with 0.1 L/min interval. Besides, the experiments were repeated to ensure stable cooling cycles. Performing over ten continuous cooling cycles on each sample at a constant flow rate, then truncating the last five cycles as research objectives. The accuracy of thermocouples used in experiments reached 0.1K after the calibration, and the pressure gauges have a satisfying accuracy of 1 kPa.

6.8. Results and Discussion

6.8.1. Computational Simulations and Performance Maps

6.8.1.1. Circular CCCs

Results of the computational simulations and metamodels (performance maps) are evaluated according to the main objectives that are the cooling time, temperature non-uniformity, and pressure drop. Figure 6.11. represents the results of a case of a circular channel for three different objectives.

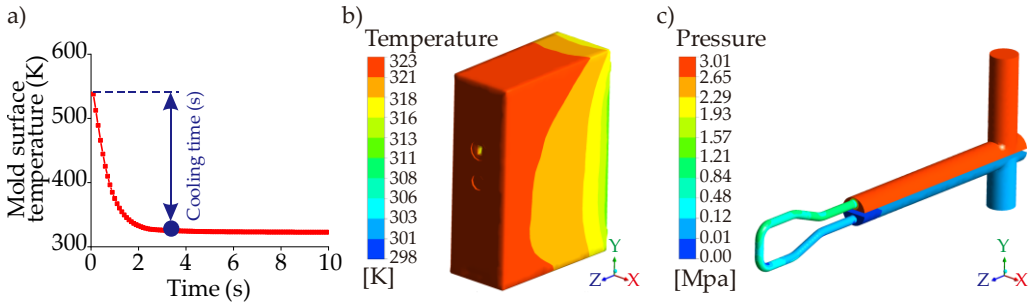

Figure 6.11. Representative CFD case of a circular channel (D=2.1mm, coolant temperature=298 K, volume flow rate=10 L/min) results; a) cooling time, b) temperature distribution, and c) pressure drop.

Following the outcomes of the computational simulations, performance maps generated by metamodels are obtained and the performance assessments are done with respect to the minimum cooling time, minimum temperature non-uniformity, and minimum pressure drop. As mentioned in the section of metamodel development, each CFD result is marked in the design space first; then, combining the increasing/decreasing trends of the computational simulations, performance maps are generated. Figure 6.12. shows the CFD results and corresponding performance maps for the main objective functions of the circular CCC with D=2.1 mm. The whole data of circular CCCs from D=2.1 mm to D=2.5 can be seen in Table A1. Regarding Figure 6.12, it is seen that the cooling time reaches its minimum value of 3.9 s at the coolant temperature of 288 K and the volume flow rate of 10 L/min, which is an expected outcome due to the high-volume flow rate and low coolant temperature. Compared to the cooling time performance of the straight-drilled channel, which is 7.0 s, the circular CCC decreases the cooling time by 44.3%. On the other hand, the maximum cooling time value is 6.3 s that belongs to the parameter set of the cooling temperature of 298 K and the volume flow rate of 1 L/min. This shows that the circular CCC with D=2.1 achieves the cooling time decrement at least by 10% compared to the straight-drilled channel. However, as the main point of this study, the

cooling time is not the primary objective; it should be considered with other two objectives: temperature non-uniformity and pressure drop. When the temperature non-uniformity values are seen in Figure 14b, it is seen that the maximum temperature non-uniformity is 7.01 K at the coolant temperature of 288 K and the volume flow rate of 10 L/s, which is exactly the same parameter set of the minimum cooling time data. The minimum temperature non-uniformity is 4.41 K at the coolant temperature of 298 K and the volume flow rate 1 L/min. When the cooling time and the temperature non-uniformity trends are evaluated together, it is clearly seen that the difference between the minimum and maximum values are more significant for temperature uniformity and the trends of cooling time & temperature non-uniformity are opposite to each other. This opposition supports our motivation for selecting the multi-criteria decision-making according to multiple objectives. The increase of diameter from 2.1 mm to 2.5 decreases the minimum cooling time from 3.9 to 3.6 s while grows the maximum temperature non-uniformity from 7.01 K to 7.29 K. That is, the increment rate of temperature non-uniformity is 3.9% while the decrement rate of cooling time is 7.7% from D=2.1 to D=2.5 mm.

In addition to the objectives of temperature non-uniformity and cooling time, pressure drop results and its performance map is projected in Figure 6.12 (c). Differently from others, the pressure drop inherently is affected only by volume flow rate for a constant diameter. For D=2.1 mm, the pressure drop increases by 1. 45 MPa from the volume flow rate of 1 L/min to 10 L/min. When the diameter increases from 2.1 to 2.5 mm, the pressure drop decreases by 59% (from 1.49 MPa to 0.61 MPa) at the volume flow rate of 10 L/min. It is worth noting that the decrement rate of pressure drop becomes smaller

by decreasing of volume flow rate. For example, at the volume flow rate of 1 L/min, the decrement is very small, only at decimal levels.

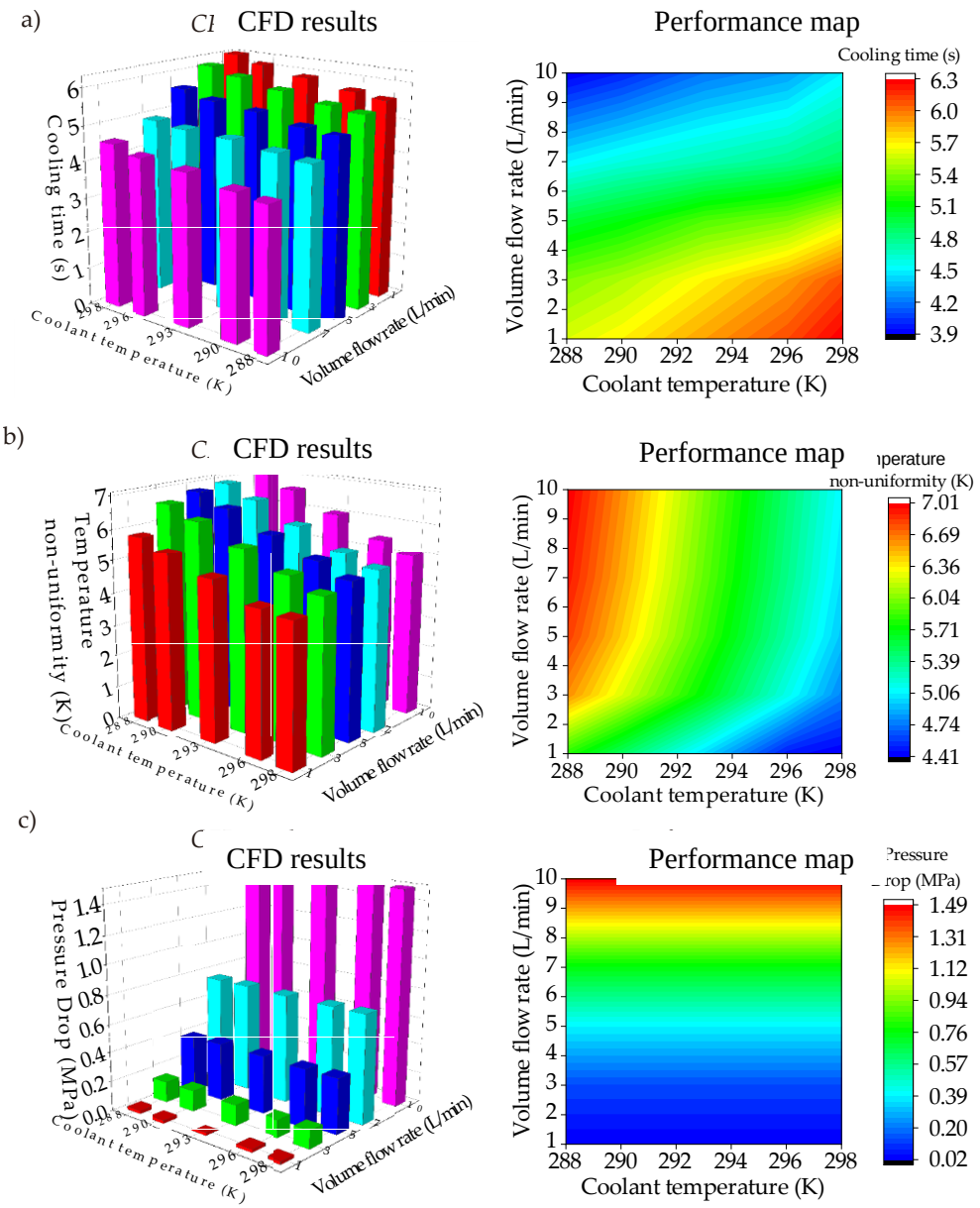

Figure 6.12. Computational results and performance maps for the circular CCC with D=2.1 mm; a) cooling time, b) temperature non-uniformity, and c) pressure drop.

6.8.1.2. Tapered CCCs

The tapered CCC aims to extend the lateral (internal wall) surface area in the mold geometry by changing the diameter from a smaller value to a higher value; hereby, a

greater heat transfer surface can be obtained. Due to the advantages of the circular cross-section compared to the elliptical, elongated, and triangular CCCs, we prefer circular cross-section for tapered CCCs. Figure 6.13. shows the performance maps of the tapered CCC and the BCC lattice-integrated tapered CCC according to cooling time, temperature non-uniformity, and pressure drop.

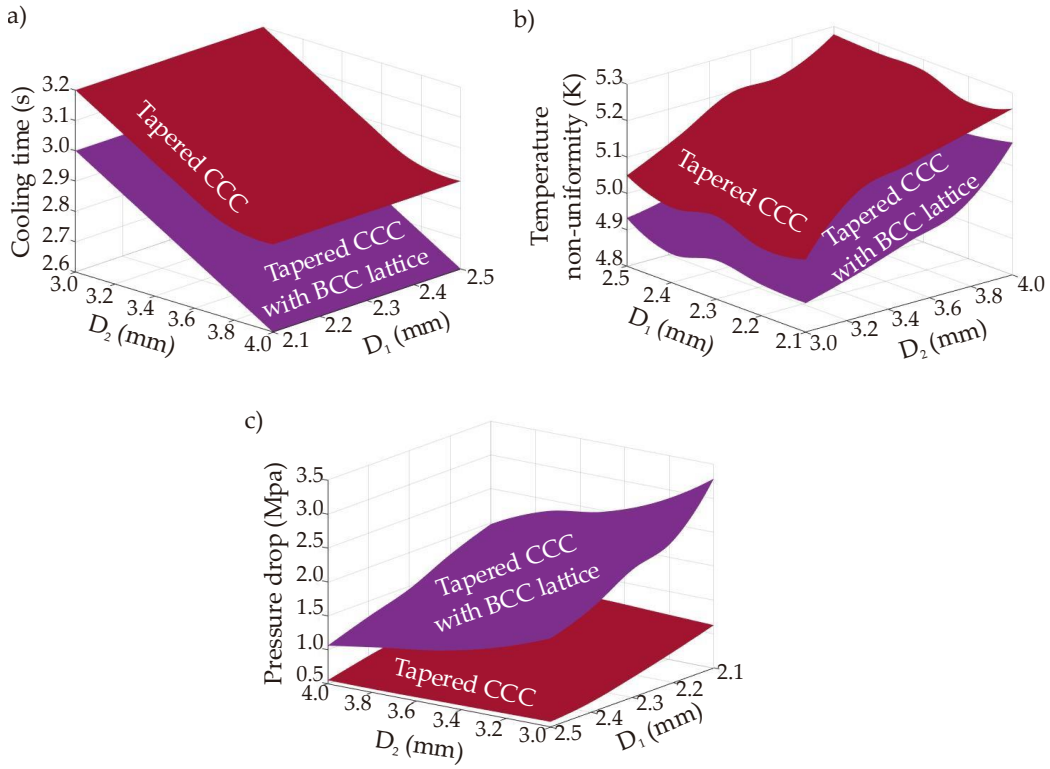

Figure 6.13. Performance maps for the tapered CCCs; a) cooling time, b) temperature non-uniformity and c) pressure drop (at the coolant temperature of 298 K and the volume flow rate of 10 L/min).

The performance map of the cooling time infers that the cooling time is not affected by the circular channel diameter, D_1 in Figure 6.3. (a), as that part is away from the hot spots of the mold part, which interacts with the melt polymer. Only D_2 value affects the cooling time trends because that part is directly in contact with the hottest spots and regions in the mold geometry. The minimum and maximum cooling time of the tapered CCC are 2.9 and 3.2 s, respectively; which shows that the tapered CCC design achieves better cooling time performance than the circular CCC. Compared to the circular CCC

from D=2.1 mm to D=2.5 mm, the tapered CCC shortens the cooling time in the range of 29.3%-35.6%. Also, compared to the straight-drilled channels, the cooling time is decreased by 58.6%. It is also seen that the BCC lattice integration provides further cooling time decrement as the BCC lattice surfaces increase the heat transfer rate through the convection and conduction mechanisms. Compared to the tapered CCC, BCC integration decreased the minimum cooling time from 2.9 s to 2.6 s; which makes the cooling time decrement by 62.9% when it is compared with the cooling time performance of the straight-drilled channel. The temperature non-uniformity map projects that both D_1 and D_2 affect the temperature uniformity but the impact of D_2 is inherently higher due to the same reason for the cooling time trends; D_2 is very near the hot spots and regions in the mold geometry. Similar to the cooling time trends, the tapered CCC achieves smaller temperature non-uniformity with an average decrement rate of 2.4%. The decrement rate is small so that it can be assumed that there is no significant change in the temperature non-uniformity trends between the circular CCCs and the tapered CCCs although the tapered CCC achieves a shorter cooling time. When the BCC lattices are integrated into the tapered CCC, the decrement in the temperature non-uniformity becomes larger with the average decrement rate of 5.7% compared to the circular CCCs from D=2.1 mm to D= 2.5 mm. Another effective point of tapered CCCs is the positive impact of the tapered design on the pressure drop. The difference between the minimum and maximum pressure drop values is not large and the average pressure drop of the tapered CCC is calculated 0.84 MPa. The pressure drop trends of the tapered CCC is smaller than the circular CCCs from D=2.1 mm to D=2.3 mm, but larger than the circular CCCs from D=2.4 mm to D.2.5 mm. That is, the pressure drop trends of the tapered CCC is in the same range as the pressure drop trends of the circular CCCs. However, the integration of the BCC lattices increases the pressure drop since

the lattice bodies result in additional flow resistance inside the channel. The pressure drop values of the BCC-integrated tapered CCC range between 1.06 and 3.29 MPa and the average pressure drop value is 1.91 MPa. These trends are larger than the pressure drop trends of the circular CCCs from D=2.1 mm to D=2.5 mm. That is, the BCC integration achieves better cooling time and temperature non-uniformity but results in higher pressure drop compared to both tapered CCCs and circular CCCs. Moreover, it is seen that the impact of D_1 on the pressure drop is greater than the impact of D_2 because the D_1 directly connects with the main coolant inlet, which has a higher diameter than both D_1 and D_2 (see Figure 2), thus the biggest pressure drop occurs at that stage.

6.8.2. Multi-criteria Decision Making

Computational simulations and performance maps show that the tapered CCCs (both tapered CCC and the BCC-integrated tapered CCC) and circular CCCs provide preferable performances from the viewpoints of cooling time, temperature non-uniformity, and pressure drop. Selection of the convenient design should depend on the weights of the objectives in the multi-criteria decision-making procedure, but it is clear that the serpentine CCCs are less preferable. Considering all objectives, the multi-criteria decision-making procedure focuses on the multiobjective optimization & 3D printing of the circular CCCs and tapered CCCs together. Following the multiobjective optimization procedure, Figure 6.14. projects the MATLAB-based Pareto frontier plots for the circular CCC, tapered CCC, and the tapered CCC with BCC lattices. The Pareto frontier plots of the circular CCC have a wider solution region compared to the tapered CCC and the BCC-integrated tapered CCC because the operating conditions of the circular CCC are defined in a broader range; in the ranges of 288.0 K- 298.0 K and 1 L/min – 10 L/min for the coolant temperature and the volume flow rate, respectively.

On the other hand, since the tapered CCC studies only focus on the changes in D_2 and D_1, we performed their simulations at the constant values of coolant temperature (298 K) and the volume flow rate (10 L/min). That is to say, even though the Pareto frontier plots of the circular CCCs and tapered CCCs are shown in the same figure (Figure 6.14.), their parameter sets are different so that we perform separate multiobjective optimization procedures for the circular CCCs and the tapered CCCs. The obtained Pareto frontier plots allow us to select the most convenient point according to our preferences. In this study, we put equal weights for all three objectives; namely, the weightage of each objective is 1/3 (~0.333 or ~33.3%). The weighted-sum approach is applied with the same weightage values for all objectives; then, the best trade-off points are obtained for each CCC type; circular CCC, tapered CCC, and tapered CCC with BCC lattice. The best trade-off point of the circular CCC is found at the coolant temperature of 297.68 K, volume flow rate of 1.01 L/min, and diameter of 2.5 mm. This shows that the equal weightage in the multiobjective optimization procedure provides the best trade-off point at the values of the maximum coolant temperature, the minimum volume flow rate, and the maximum pressure drop values. Even though the cooling time reaches its minimum value at the minimum coolant temperature value, the combined impact of the temperature non-uniformity and the pressure drop trends on the best trade-off point makes the most convenient coolant temperature at 297.68 K. The best trade-off point of the tapered CCCs are determined according to the parameters of D_1 and D_2 without considering the coolant temperature and volume flow rate. At equal weights, the best trade-off is obtained at the maximum value (2.5 mm) for D_1 and close to the maximum value (3.8 mm) for D_2. That is to say, although high diameter values increase the temperature uniformity, they are found feasible as they minimize the pressure drop and cooling time. Also, diameter values (D_1 and D_2) of the best trade-off points of the

tapered CCC and the tapered CCC with BCC lattices are the same but their corresponding cooling and pressure parameters (cooling time, pressure drop, temperature non-uniformity) are different. It is worth noting that the obtained best trade-off points are for equal weights. In the case of non-equal weights, the best trade-off point values depend on the primary objective functions.

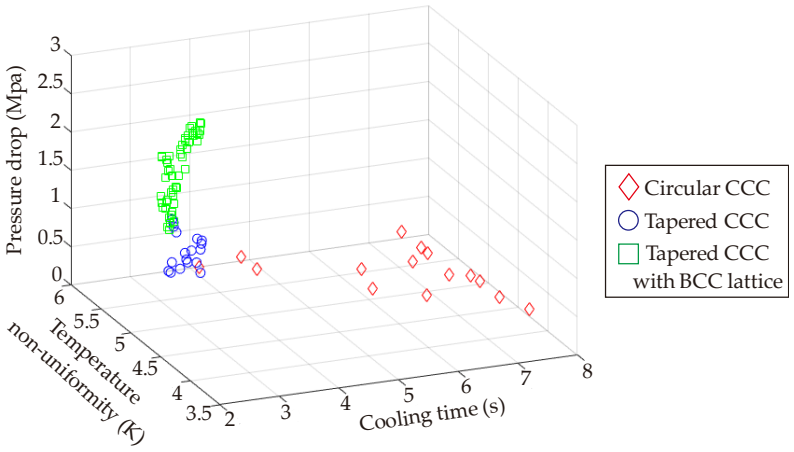

Figure 6.14. Pareto frontier plots of the circular CCCs and tapered CCCs.

6.8.3. DMLS processed molds

For circular and tapered channels, the channel diameter is the most significant evaluation index to evaluate printability. Figure 6.15. (a) and (b) show the 2D CT images of circular and tapered channel cross-section area, and the diameters of real printed internal channels were measured in the CT image process software. In the circular channel, the measured values of *Ø 1~ Ø 7* were used to compare with the designed channel diameter of 2.5 mm. In the tapered channel, the values of *Ø 1~ Ø 4* were used to check the printability of inlet and outlet channels with the diameter of 2.5 mm, and the values of *Ø 5*, *Ø 6*, and *Ø 7* were compared to the enlarged channels with the diameter of 3.8 mm.

As the BCC lattice filled design is a combination of BCC structures and a tapered cooling channel, the channel printability validation method in it is the same as that in the tapered channel. For checking the BCC lattice structure printability in the tapered channel, three pieces of BCC lattice structures were isolated, 3D CT images of them were then generated (See Figure 6.15 (c)). In each isolated BCC lattice structure, diameters of four component cylindrical struts d_1~d_4 were measured and compared with the designed ones of 0.5 mm.

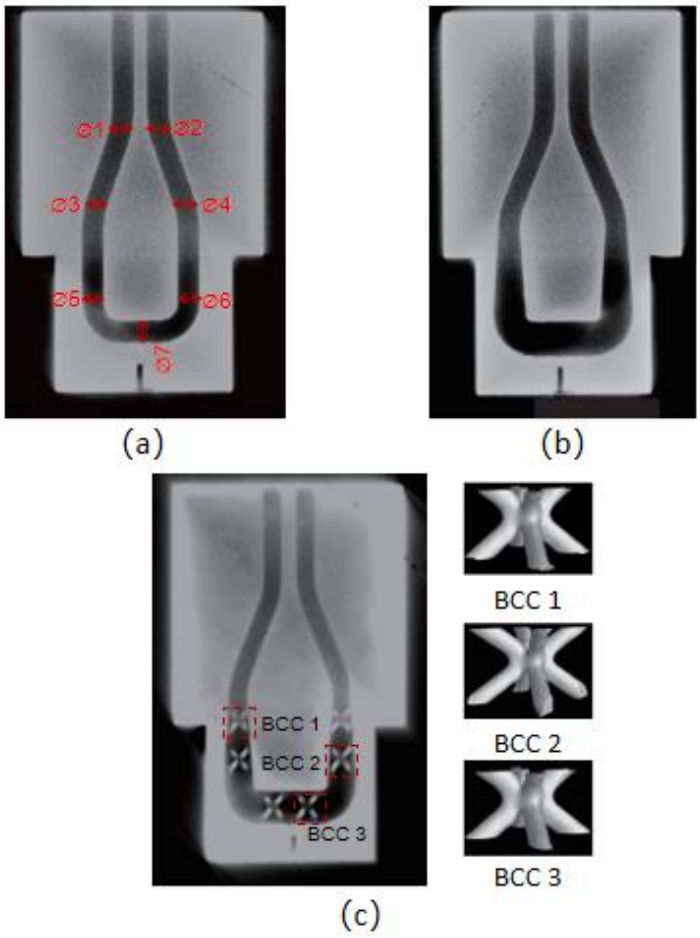

Figure 6.15. CT images of: (a) Mold 1_optimized circular, (b) Mold 1_optimized tapered, and (c) Mold 1_optimized BCC lattice filled samples.

The DMLS manufacturing error was defined based on Eq. (6.9).

$$\text{Error} = \frac{|x_M - x_D|}{x_D} \times 100\% \quad (6.9)$$

Where X_M and X_D are the measured and designed dimensions, respectively. Table 6.2. shows the detailed comparisons between the designed and X-ray CT system measured channel dimensions. It was found out that all DMLS processed Mold 1 samples have high-quality 3D printed cooling channels, in which the fabrication error was controlled within 3.2%.

Table 6.3 shows that the fabrication error of BCC is around 15%. As the maximum dimensional deviation of real 3D printed BCC strut diameters from the designed ones is smaller than 0.08 mm, the printing quality was considered satisfying.

Table 6.2 . Channel design validation in the plastic injection mold

Designed channel diameter (mm)	X-ray CT measured channel diameters (mm)	Maximum error (%)
Circular channel		
D=2.5	*Ø1~ Ø 7*: 2.42, 2.46, 2.40, 2.42, 2.44, 2.42, 2.46	4
Tapered channel		
D1=2.5	*Ø 1~ Ø 4*: 2.44, 2.48, 2.44, 2.44	*Ø 1~ Ø 4*: 2.4
D2=3.8	*Ø 5~ Ø 7*: 3.70, 3.84, 3.84	*Ø 5~Ø7*: 2.6
Tapered channel in the Mold 1_lattice filled		
D1=2.5	*Ø 1~ Ø 4*: 2.42, 2.46, 2.44, 2.48	*Ø* 1~ *Ø* 4: 3.2
D2=3.8	*Ø 5~ Ø 7*: 3.76, 3.82, 3.86	*Ø 5~ Ø 7*: 1.6

Table 6.3. BCC lattice structure printability validation

No. of X-ray CT measured BCC	Designed cylindrical strut diameter (mm)	X-ray CT measured diameters d_1~d_4(mm)	Maximum error (%)	Maximum deviation (mm)
1	0.5	0.44, 0.5, 0.52, 0.44	12	0.06
2		0.42, 0.52, 0.46, 0.44	16	0.08
3		0.48, 0.46, 0.5, 0.44	12	0.06

6.8.4. Experimental Validation

6.8.4.1. Cooling time

The DMLS processed molds with optimized circular, tapered, and BCC-filled conformal cooling channels were tested and compared with each other in terms of silicone oil cooling time, the temperature change of specific surface locations, and pressure drop between inlet and outlet of cooling water. Adjusting the flow rate of cooling water from 0.1 L/min to 0.4 L/min, the corresponding analysis of measured parameters is presented below.

In cooling experiments, over ten cooling cycles were conducted, and the last five continuous ones, in which relatively stable cooling time occurred, were picked up and studied (see Figure 6.16).

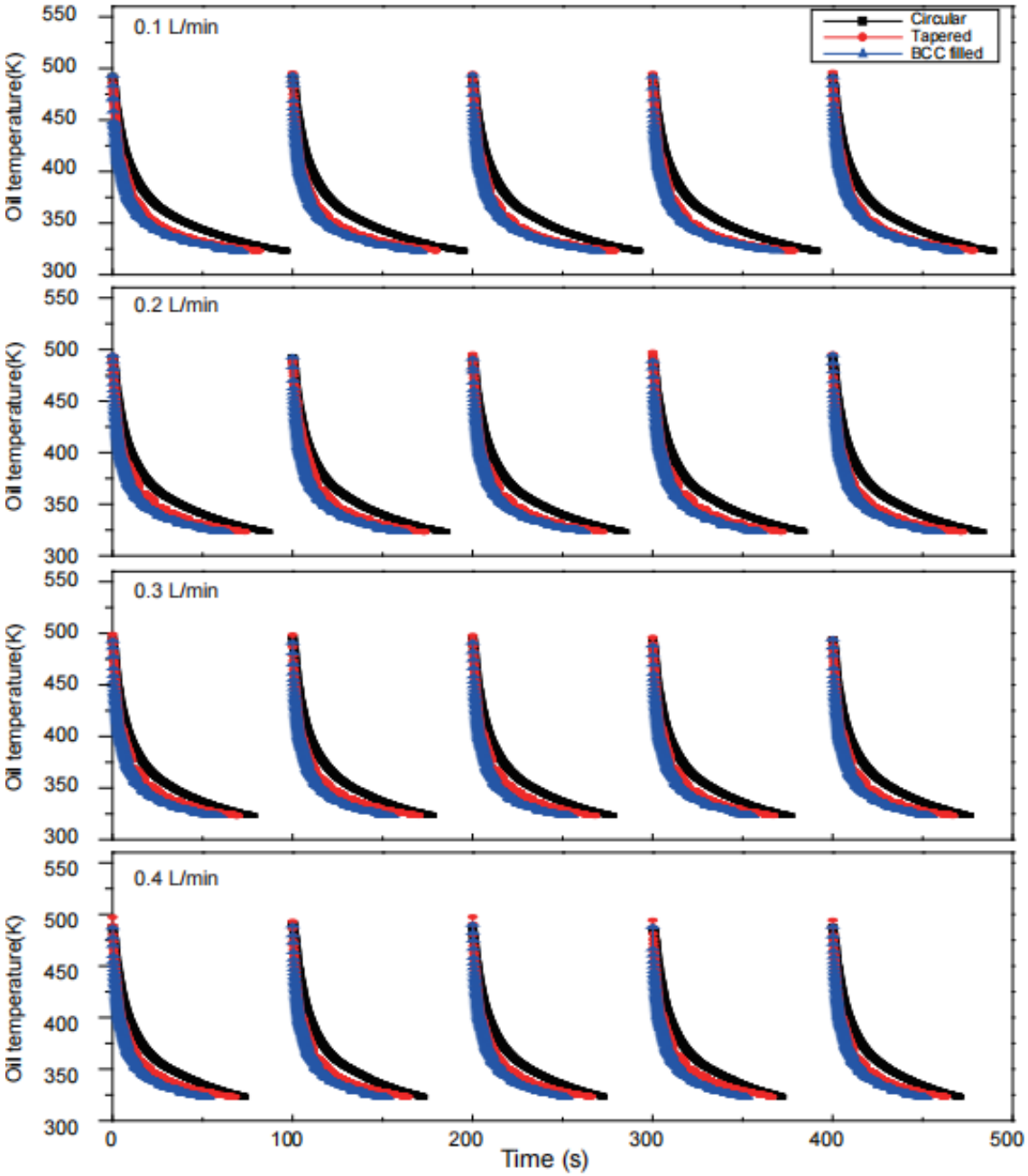

Figure 6.16. Continuous cooling cycles in CCCs experiments.

For the same sample, it is seen that the cooling time decreased significantly with the increase of the coolant flow rate. Besides, the cooling rate i.e. slope of the oil temperature curve, gradually decreased in every cooling cycle, resulting from the lower temperature gradients between the silicone oil, the solid mold part, and the cooling water in the channel. At the same flow rate value of the cooling water, the BCC filled channel

performed the best in the cooling efficiency, followed by the tapered one, and the last is the circular one. Table 6.4. summarizes the cooling time of all cycles.

Table 6.4. Experimental cooling time of Mold 1 samples.

Flow rate (L/min)	0.1	0.2	0.3	0.4
Circular channel				
Cooling time (s)	96.25, 95, 92.25, 91.125, 89	86.5, 85.25, 84.625, 83.75, 83	78.125, 77.75, 77.625, 76.5, 76.375	73.375, 73.375, 72.625, 71.875, 70.5
Tapered channel				
Cooling time (s)	81.625, 79.75, 79.25, 78.625, 78.5	78.625, 73.5 , 72.875, 72.25, 72.125	70.375, 70.25, 68.625, 67.875, 67.125	66.375, 65.875, 64.375, 64.375, 63.25
BCC filled channel				
Cooling time (s)	71.375, 71, 70.125, 69.25, 68.875	63.25, 62.625, 61.625, 60.625, 58.75	59.5, 55.125, 55.125, 54.75, 54.25	52.75, 52.25, 52.25, 51.875, 51.25

6.8.4.2. Temperature changes on the mold surface

In cooling experiments, as the locations of T_{top}, T_{side}, and T_{front} were the ones facing the central axis of conformal cooling channel path, their temperature changes in the cooling cycle reflect the effects of coolant flow rate and channel design on the cooling efficiency of different insert surfaces.

The surface temperature changes of the mold in the fifth cooling cycle, and the temperature trend is visually shown in Figure 6.17. The average of eight sampled temperature values per second was used as the real-time value at the time interval of 1s to increase the sampling stability. It was found out that the top surface is always the one with the highest temperature, followed by the front surface, then the side surface. It can also be seen that the tapered channels still keep slight temperature differences between

different surfaces like the circular channel, but the BCC filled ones perform the higher cooling efficiency at the cost of the large surface temperature nonuniformity.

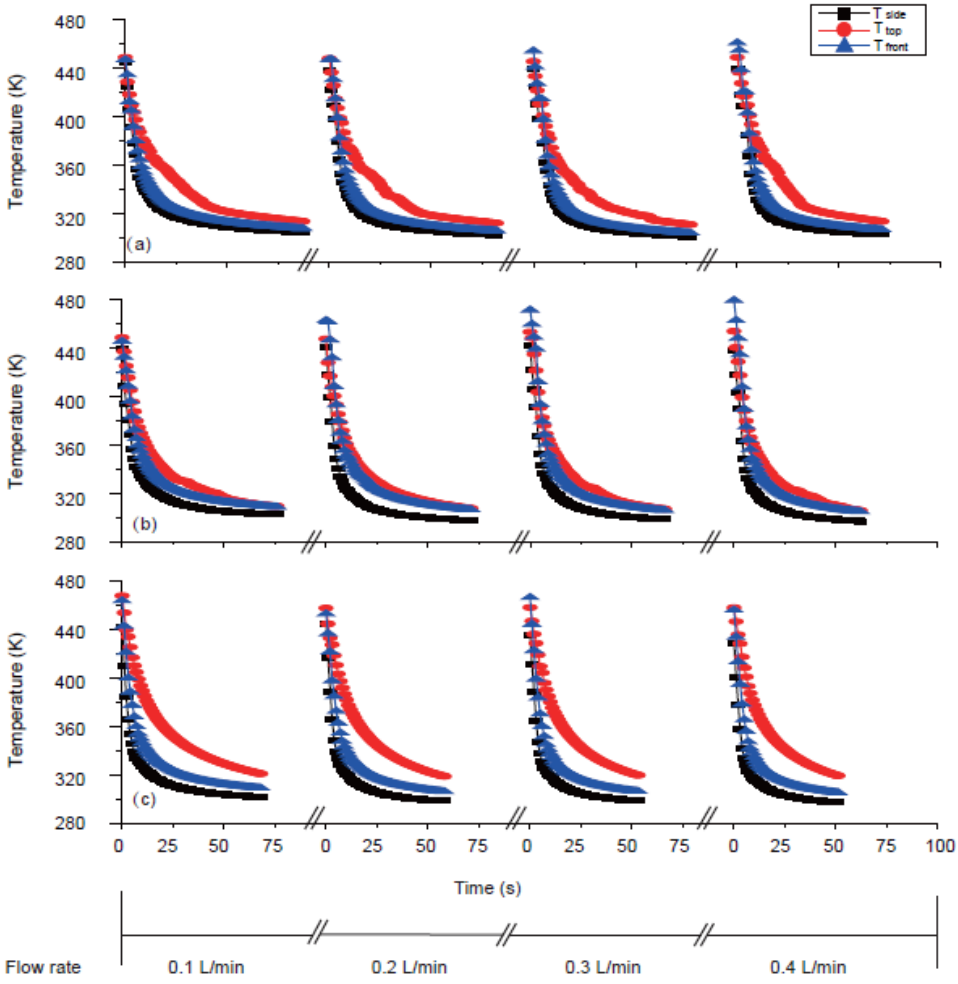

Figure 6.17. Surface temperature changes of optimized (a) circular, (b) tapered, and (c) BCC filled channels in the fifth cooling cycle

As the initial temperature values of different surfaces are different, a new concept of normalized temperature was introduced to depict the temperature change trend of T_{top}, T_{side}, and T_{front}, and it is determined as the ratio of the instant temperature value to the initial one, as shown in Eq. (6.10),

$$NT_i = \frac{T_i}{T_0} \tag{6.10}$$

where NT_i is the normalized temperature of specific surface location, T_i is the real-time measured temperature value (K), and T_0 is the initial temperature value(K). Figure 6.18. shows the plots of normalized temperatures and cooling time in the fifth cooling cycle. It's very clear that the NT_{top} decreased the most slowly, and the NT_{side} decreased a little faster than NT_{front}. The difference was mainly caused by the gravity effect. The top surface was cooled down by a parallel channel, whereas the side surface and front surface were mainly cooled down by the vertical channel, in which the cooling water velocity is larger owing to the gravity. As the wall thickness of the front part (5 mm) is larger than that of the side part (1.8 mm in circular channel, 1.2 mm in tapered and BCC filled channel), the front surface cooling efficiency was worse than the side surface due to the lower temperature gradient in the heat conduction.

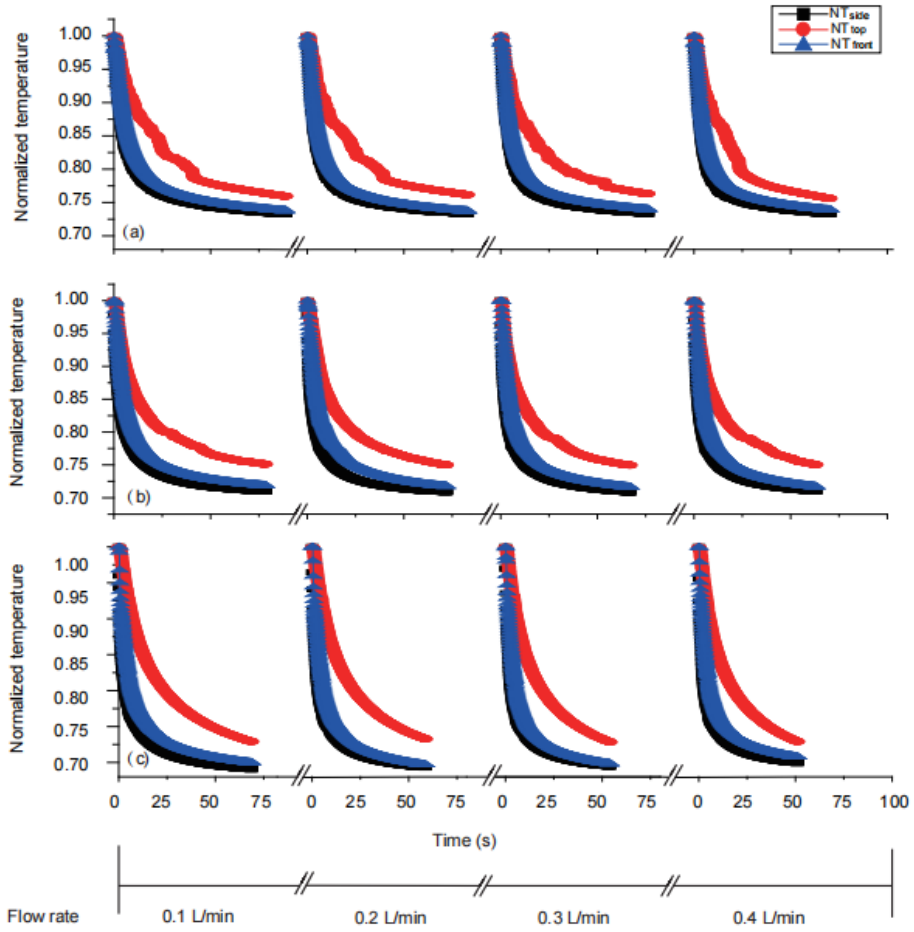

Figure 6.18. Normalized temperatures of top, side, and front surfaces in the mold with optimized (a) circular, (b) tapered, and (c) BCC filled channels

It can also be concluded that the surface cooling efficiency of BCC filled design is better than the circular and tapered ones, and the larger coolant flow rate contributes to the larger normalized temperature change. Using the normalized temperature change rate (*ΔNT/Δcooling time*) to explain the conclusion in detail. For each design, the normalized temperature change (*ΔNT)* was observed very similar to each other when adjusting the coolant flow rate, the larger normalized temperature change rate resulted from the shorter cooling time. Changing the channel designs from circular to tapered, and BCC filled ones, the shorter cooling time was still measured, meanwhile *ΔNT* increased

significantly. Consequently, the higher cooling efficiency can be attained. The analysis in this section provides the guides for the future design:

- The distance between the conformal cooling channel and the top surface of the insert should be adjusted to compensate the unsatisfying cooling performance caused by the gravity.
- The design optimization is more effective than enlarging the coolant flow rate. For example, the BCC filled tapered channel design performed the best cooling efficiency in the proposed Mold 1 channel designs.

6.8.4.3. Pressure drop

The pressure drop between the inlet and outlet of the cooling water was also measured in experiments, as shown in Table 6.5.

It can be seen that the pressure drop increased with the increase of the flow rate, and the BCC filled channel had the larger pressure drop than the circular and tapered ones. The larger pressure drop means that more impingement energy from the inlet was absorbed by the conformal cooling channels, which affect the required pump power in real operations.

Table 6.5. Experimental pressure drop of Mold 1 samples.

Flow rate (L/min)	0.1	0.2	0.3	0.4
Circular channel				
Pressure drop ($\times 10^4$Pa)	0.5, 0.5, 0.5, 0.5, 0.5	1.5, 1.5, 1.5, 1.5, 1.5	7, 7.1 ,7.1, 6.9, 6.9, 7	13.5, 13.5, 13.5, 13.4, 13.6
Average Pressure drop ($\times 10^4$Pa)	0.5	1.5	7	13.5
Tapered channel				
Pressure drop ($\times 10^4$Pa)	0.8, 0.8, 0.8, 0.8, 0.8	5.5, 5.5, 5.5, 5.4, 5.6	12, 12, 12, 12, 12	18.5, 18.7, 18.6, 18.6, 18.6
Average Pressure drop ($\times 10^4$Pa)	0.8	5.5	12	18.6
BCC filled channel				
Pressure drop ($\times 10^4$Pa)	1.1, 1.2, 1.2, 1.2, 1.3	6, 6, 6 ,6 , 6, 6	12.8, 12.7, 12.9, 12.8, 12.8	23, 23, 23, 23, 23, 23
Average Pressure drop ($\times 10^4$Pa)	1.2	6	12.8	23

6.8.4.4. Validation of experimental results

Experiments were used to verify the the cooling time and pressure drop derived from the numerical simulations of the plastic injection mold. The simulation setting is the same as described in Figure 6.4. and the total mesh number is around 0.6 million. The numerical model employed is a little different from the previous one) The cooling channels out of the sample were neglected; 2) The plastic was replaced by the silicone oil (the density is 1058 kg/m^3, the specific heat capacity is 1465 J/kg·K, and the thermal conductivity is 0.134 W/m·K); 3) Enlarged oil volume, as illustrated in the section of experimental setup. The comparisons between experimental and simulated cooling time are shown in Figure 6.19.

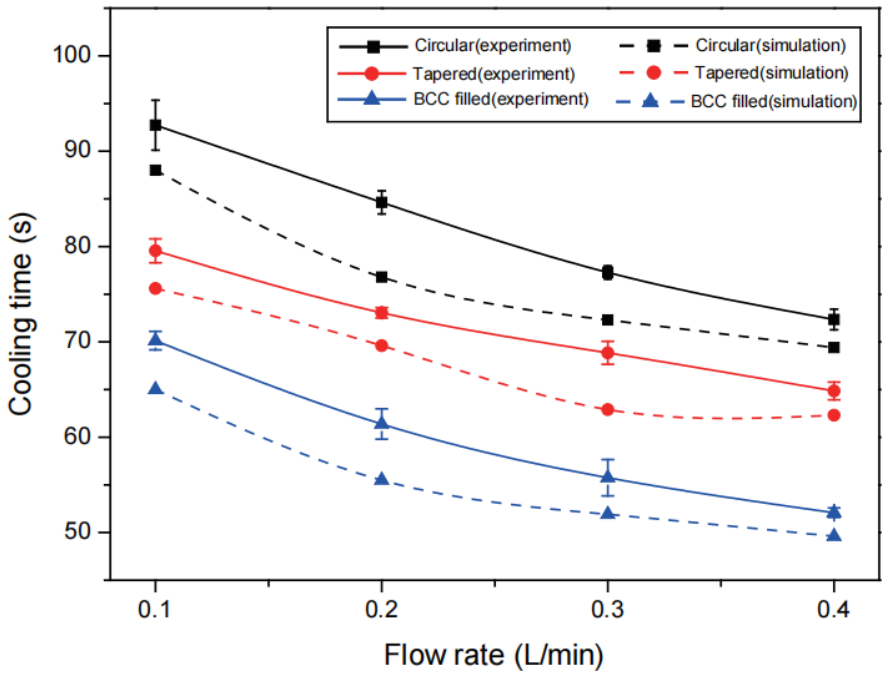

Figure 6.19. Comparisons on cooling time between experiments and simulations.

The experimental cooling time trends are good agreement with the simulation results, and the deviation was within 8s. In the test module of the experimental setup, there are two pipes used as inflow and outflow of the silicone oil, after closing Valve 1 and Valve 2 for conducting the cooling cycle, a certain volume of oil would be stored in the pipes, which led to the longer cooling time in experiments.

As listed in Table 6.5, since the values of measured pressure drop floated very slightly upward and downward the average value of pressure drop, the sample standard deviation can be neglected in the analysis. Using the average pressure drop value from the continuous five cooling cycles as the experimental data, the comparison between experiments and numerical simulations is shown in Figure 6.20. The experimentally measured pressure drop fit very well with the simulation derived one, especially at the lower flow rate. The reason for the higher pressure drop in experiments is that the numerical model didn't take the channel surface roughness into account. Besides, it was found out that with the increase of the coolant flow rate, the pressure drop increased

with an increasing slope, which inspires that the increase of flow rate in the real plastic injection molding process should be considered carefully, which affects the mold life significantly.

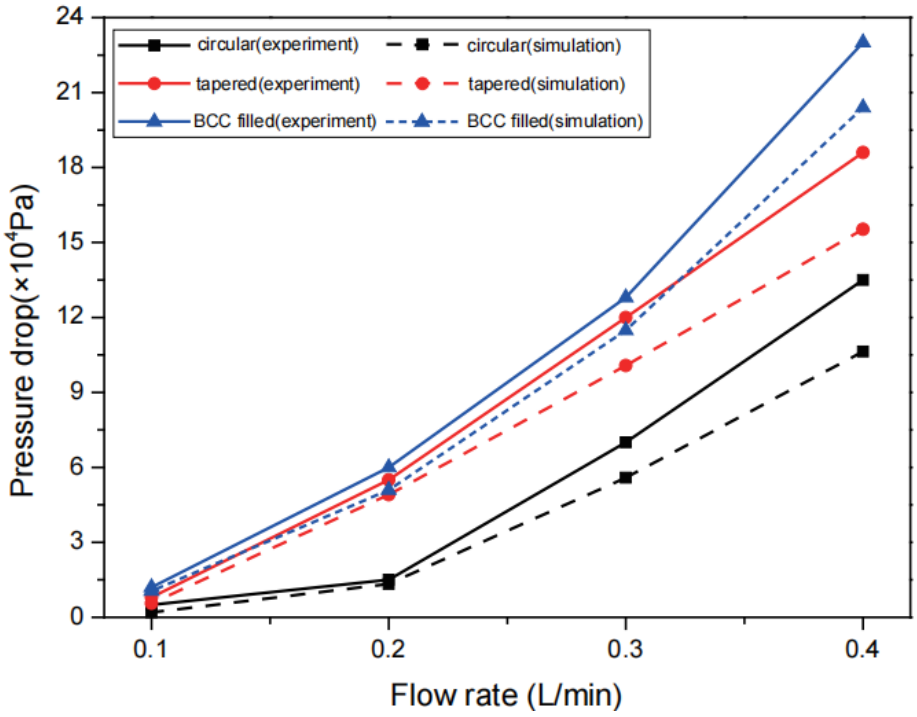

Figure 6.20. Experimental and numerical derived pressure drop trends through the optimized CCCs

For validating the accuracy of experimental and simulated pressure drop values, the flow patterns in optimized circular, tapered, and BCC filled channels at the flow rate of 0.4 L/min are shown in Figure 6.21. It can be seen that tapered channels increase the cooling efficiency by larger cooling areas, and BCC filled channels perform better cooling by inducing turbulence around the lattice structures.

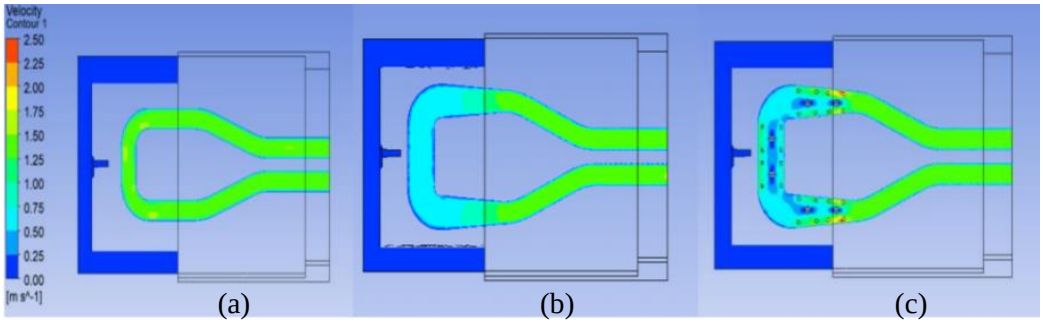

Figure 6.21. Flow patterns in: (a) circular, (b) tapered, and (c) BCC filled channels

Table 6.6. summarizes the average coolant velocity at the inlet and outlet. As the velocity difference between the inlet and outlet is proportional to the pressure drop, the pressure drop should be sorted as the order of BCC filled, tapered, and circular channels based on the simulated flow patterns, which fit well with the experimental and simulated pressure drop values.

Table 6.6. Coolant velocity at the inlet and outlet under the flow rate of 0.4 L/min

Flow rate (L/min)	Circular	Tapered	BCC filled
Inlet velocity (mm/s)	1358.80	1358.80	1358.80
Outlet velocity (mm/s)	1358.08	1355.48	1354.54
Velocity difference (mm/s)	0.72	2.32	4.26

6.9. Summary

This chapter presented the study investigated the entire process of design, simulation, optimization, fabrication, and experimental validation of the circular, tapered, and BCC lattice filled tapered conformal cooling channels (CCCs). A specific plastic injection mold product with multiple design parameters and three main objectives, which are minimum cooling time, minimum temperature non-uniformity, and minimum pressure drop were fabricated by the DMLS technology and experimentally validated by experiments. When BCC lattice structures were integrated into the channel body, the heat transfer via conduction and convection increased so that the cooling time decreased

dramatically when compared with circular and tapered CCCs. However, the circular CCCs had lower temperature non-uniformity than the tapered CCC with BCC lattice whilst there was no significant difference between the temperature non-uniformity values of circular CCCs and tapered CCCs. Pressure drop trends inferred that the tapered CCCs and circular CCCs had very similar pressure drop values but the integration of BCC lattices increased the pressure drop to the average value of 1.91 MPa, which was still acceptable as the cooling time has been shortened significantly.

Chapter 7. Conclusions and future works

7.1. Conclusions

In this work, the heat conduction mechanisms of lattice structures were investigated experimentally and numerically. The hydraulic and heat transfer characteristics in the forced convection process were determined by experiments. Combining the conductive and convective heat transfer studies, the lattice structure was applied in a specific conformal cooling channel design in industry. The major findings from different studies in this work are listed as follows.

1. Design and fabrication of lattice structures

In studies of heat conduction and forced heat convection, four kinds of muti-layered lattice structures including BCC, FCC-Z, FCC-XY, and octet-truss ones, were designed by characterizing the unit cell geometry and fabricated by the selective laser melting technology. For fully and theoretically investigating the effects of structural parameters on lattice structure thermal performance, the explicit dimensional parameter strut radius values of different lattice structures were adjusted to make sure they have the same porosity, or the same porosity and same surface area at the same time. Subsequently, based on the conduction and convection studies, the direct metal laser sintering method was used to fabricate the plastic injection mold with lattice structure integrated conformal cooling channels, to utilize the thermal advantages of lattice structures in industry.

2. The steady-state heat conduction process in 3D printed lattice structures

Experimental and numerical studies were both employed to investigate the effects of structure design variables on the conductive heat transfer performance of lattice

structures, so as to further control the heat conduction in lattice structures. It was found that for a specific type of lattice structure, decreasing the porosity or specific surface area contributed to the larger effective thermal conductivity value. However, different lattice structures have different effective thermal conductivity values even at the same porosity, which disobeyed the previous analytical models predicting the effective thermal conductivity based on the porosity value. A deeper study was then conducted on the lattice structure containing tapered struts for determining the effect of cross-section area along the main heat conduction direction, and it was concluded that the minimum cross section area corresponds to the heat conduction weak point. For achieving a perfect balance between the lightweight characteristic and excellent heat conduction performance, a new concept of specific thermal conductivity was firstly proposed.

3. The steady-state heat convection process in 3D printed lattice structures

The hydraulic and heat transfer characteristics of different typed lattice structures in forced convection have been studied, and the analysis of geometric parameter study provides fundamentals for further controlling the convective performance of lattice structures. In the term of hydraulic performance, the FCC-XY lattice structure performed the best due to the smallest open area ratio, which inspired the future application of FCC-XY in the fields that the lower pumping power is preferred. In the term of convective heat transfer performance, the octet-truss lattice structure performed the best due to the largest interfacial surface area contacting with the air flow.

4. Application of lattice structure in the conformal cooling channel design

In order to improve the cooling efficiency of optimized tapered conformal cooling channels, BCC lattice structures were integrated to the tapered channels. The integration of BCC lattice structures into conformal cooling channel design is the preliminary study

on using lattice structures to improve the mechanical and thermal properties of plastic injection mold. The use of lattice structures is expected to elongate the mold fatigue life and improve productivity of the plastic injection molding at the same time. The BCC integrated channels performed the shorter cooling time than the optimized circular and tapered channel designs, which demonstrated the promising application of lattice structure in industry. However, the pressure drop and surface temperature nonuniformity through the BCC integrated channel is not as good as circular channels. A perfect balance between the minimum cooling time, minimum surface temperature nonuniformity, and minimum pressure drop still needs to be further studied.

7.2. Future works

Based on previous studies, some recommendations for future work related to the thermal management and application of lattice structures were summarized as below.

1. Controllable heat convection performance

In this work, the factors that affecting the effective thermal conductivity of lattice structure have been fully investigated, which can be used to guide the lattice structure design for controllable heat conduction performance. While in the forced convection study, the factors influencing the hydraulic characteristics have been studied, not too many findings related to the factors determining the convective heat transfer characteristics. In this condition, the future work focusing on controllable convective heat transfer studies will be combined with the controllable heat conduction performance in this work to thermally manage the lattice structure.

2. Application of lattice structure in conformal cooling channel design

This study just shows a very beginning work that taking the advantage of lattice structure excellent conductive and convective heat transfer characteristics to improve the cooling performance of the cooling channel design. The limitation is that for each design, the multi-objective optimization process needs to be started from the very beginning. So a new optimization model which can be generally used to help optimize the dimensions for the objectives of minimum cooling time, minimum temperature nonuniformity, and minimum pressure drop will be preferred.

Publications

[1] S. Shen, B. B. Kanbur, **Y. Zhou**, F. Duan. Thermal and Mechanical Assessments of the 3D-Printed Conformal Cooling Channels: Computational Analysis and Multi-objective Optimization. Journal of Materials Engineering and Performance **29,** 8261–8270 (2020). https://doi.org/10.1007/s11665-020-05251-5.

[2] B. B. Kanbur, S. Shen, **Y. Zhou**, F. Duan,Thermal and mechanical simulations of the lattice structures in the conformal cooling cavities for 3D printed injection molds, Materials Today: Proceedings, volume 28, Part 2, 2020, Pages 379-383, https://doi.org/10.1016/j.matpr.2019.10.017.

[3] **Y. Zhou**, F. Duan. Heat conduction performance of 3D printed lattice structure. The 15th International conference on heat transfer, fluid mechanics and thermodynamics (HEFAT) and editorial board of applied thermal engineering (ATE), 26-28 Jul 2021.

References

[1] W. Tao & M. C. Leu, "Design of lattice structure for additive manufacturing", in: 2016 International Symposium on Flexible Automation (ISFA) held in Cleveland, USA, 2016.

[2] C. Yan, L. Hao, A. Hussein, P. Young, D. Raymont, "Advanced lightweight 316L stainless steel cellular lattice structures fabricated via selective laser melting", Materials & Design, vol. 55, pp. 533-541, 2014.

[3] F. N. Habib, P. Iovenitti, S. H. Masood, M. Nikzad, "Fabrication of polymeric lattice structures for optimum energy absorption using Multi Jet Fusion technology", Materials & Design, vol. 155, pp. 86-98, 2018.

[4] H. Xue, Y. Yang, F. Gao, Y. Chong, B. Zhang, "Acoustic higher-order topological insulator on a kagome lattice", Nature Materials, vol. 18(2), pp. 108-112, 2019.

[5] K. J. Maloney, K. D. Fink, T. A. Schaedler, C. S. Roper, Multifunctional heat exchangers derived from three-dimensional micro-lattice structures, International Journal of Heat and Mass Transfer 55(9–10) (2012) 2486-2493.

[6] K. N. Son, J. A. Weibel, V. Kumaresan, S. V. Garimella, "Design of multifunctional lattice-frame materials for compact heat exchangers", International Journal of Heat and Mass Transfer, vol. 115, pp. 619-629, 2017.

[7] N. Lebaal, A. SettaR, S. Roth, S. Gomes, "Conjugate heat transfer analysis within in lattice-filled heat exchanger for additive manufacturing", Mechanics of Advanced Materials and Structures, vol. 29(10), pp. 1361-1369, 2022.

[8] H. N. G. Wadley, N. A. Fleck, A. G. Evans, "Fabrication and structural performance of periodic cellular metal sandwich structures", Composites Science and Technology, vol. 63(16), pp. 2331-2343, 2011.

[9] S. Huang, P. Liu, A. Mokasdar, and L. Hou, "Additive manufacturing and its societal impact: a literature review." International Journal of Advanced Manufacturing Technology, vol. 67, pp. 1191-1203, 2013.

[10] Vasiliev, V. V., and A. F. Razin. "Anisogrid composite lattice structures for spacecraft and aircraft applications." Composite structures, vol. 76, pp. 182-189, 2006.

[11] Alsalla, Hamza, Liang Hao, and Christopher Smith. "Fracture toughness and tensile strength of 316L stainless steel cellular lattice structures manufactured using the selective laser melting technique." Materials Science and Engineering: A, vol. 669, pp. 1-6, 2016.

[12] Saedi, Soheil, et al. "On the effects of selective laser melting process parameters on microstructure and thermomechanical response of Ni-rich NiTi." Acta Materialia 144 (2018): 552-560.

[13] Persenot, Théo, et al. "Fatigue performances of chemically etched thin struts built by selective electron beam melting: experiments and predictions." Materialia, vol. 9, pp. 89-100, 2019.

[14] Y. Chai, X. H. Yang, M. Zhao, Z. Y. Chen, X. Z. Meng, and L. W. Jin, "Study of Microstructure-Based Effective Thermal Conductivity of Graphite Foam." Journal of Heat Transfer, vol. 139, pp. 12-25, 2017.

[15] S. R. Seagle, R. L. Martin, and O. Bertea, "Electron-Beam Melting." Journal of Materials, vol. 14, pp. 812-820, 1962.

[16] W. E. Frazier, "Metal Additive Manufacturing: A Review." Journal of Materials Engineering and Performance, vol. 23, pp. 1917-1928, 2014.

[17] L. E. Murr, S. M. Gaytan, D. A. Ramirez, E. Martinez, J. Hernandez, and K. N. Amato, "Metal Fabrication by Additive Manufacturing Using Laser and Electron Beam Melting Technologies." Journal of Materials Science & Technology, vol. 28, pp. 1-14, 2012.

[18] J. Otubo, O. D. Rigo, C. M. Neto, and P. R. Mei, "The effects of vacuum induction melting and electron beam melting techniques on the purity of NiTi shape memory alloys." Materials Science and Engineering, vol. 438, pp. 679-682, 2006.

[19] P. Heinl, L. Müller, C. Körner, R. F. Singer, and F. A. Müller, "Cellular Ti–6Al–4V structures with interconnected macro porosity for bone implants fabricated by selective electron beam melting." Acta Biomaterialia, vol. 4, pp. 1536-1544, 2008.

[20] C. R. Deckard, J. J. Beaman, and J. F. Darrah, "The Method for Selective Laser Sintering (SLS) with the layerwise cross-scanning." [Online], Available: https://patents.google.com/patent/US5155324A/de15.

[21] T. Laoui, L. Froyen, and J.-P. Kruth, "Effect of mechanical alloying on selective laser sintering of WC-9Co powder." Powder metallurgy, vol. 42, 1999.

[22] J. P. Kruth, P. Mercelis, J. V. Vaerenbergh, L. Froyen, and M. Rombouts, "Binding mechanisms in selective laser sintering and selective laser melting." Rapid Prototyping Journal, vol. 11, pp. 26-36, 2005.

[23] C. Atwood, M. Ensz, D. Greene, M. Griffith, L. Harwell, and D. Reckaway, "Laser Engineered Net Shaping (LENS(TM)): A Tool for Direct Fabrication of Metal Parts." Sandia National Laboratories, Albuquerque, NM, and Livermore, CA, 1998.

[24] Y. Zhai, D. A. Lados, E. J. Brown, and G. N. Vigilante, "Fatigue crack growth behavior and microstructural mechanisms in Ti-6Al-4V manufactured by laser engineered net shaping." International Journal of Fatigue, vol. 93, pp. 51-63, 2016.

[25] D. White, "Ultrasonic object consolidation." [Online], Avaliable: https://patents.google.com/patent/US6519500B1/en.

[26] D. Janaki and Y. Stucker, "Use of ultrasonic consolidation for fabrication of multi-material structures." Rapid Prototyping Journal, vol. 13, 2007.

[27] C. Y. Kong and R. Soar, "Method for embedding optical fibers in an aluminum matrix by ultrasonic consolidation." Applied Optics, vol. 44, pp. 6325-6333, 2005.

[28] Chee Kai Chua and K. F. Leong, "3D Printing And Additive Manufacturing." Singapore: World Scientific, 2015.

[29] L. Thijs, F. Verhaeghe, T. Craeghs, J. V. Humbeeck, and J.-P. Kruth, "A study of the microstructural evolution during selective laser melting of Ti–6Al–4V." Acta Materialia, vol. 58, pp. 3303-3312, 2010.

[30] E. O. Olakanmi, R. F. Cochrane, and K. W. Dalgarno, "Densification mechanism and microstructural evolution in selective laser sintering of Al–12Si powders." Journal of Materials Processing Technology, vol. 211, pp. 113-121, 2011.

[31] S. K. Ghosh, K. Bandyopadhyay, and P. Saha, "Development of an in-situ multi-component reinforced Al-based metal matrix composite by direct metal laser sintering technique: Optimization of process parameters." Materials Characterization, vol. 93, pp. 68-78, 2014.

[32] A. Simchi and H. Pohl, "Effects of laser sintering processing parameters on the microstructure and densification of iron powder." Materials Science and Engineering, vol. 359, pp. 119-128, 2003.

[33] C. G. Ferro, S. Varetti, G. De Pasquale, and P. Maggiore, "Lattice structured impact absorber with embedded anti-icing system for aircraft wings fabricated with additive SLM process." Materials Today Communications, vol. 15, pp. 185-189, 2018.

[34] M. Niinomi, Y. Liu, M. Nakai, H. Liu, and H. Li, "Biomedical titanium alloys with Young's moduli close to that of cortical bone." Regenerative Biomaterials, vol. 3, pp. 173-185, 2016.

[35] G. S. Prihandana, M. Mahardika, Y. Nishinaka, H. Ito, Y. Kanno, and N. Miki, "Electropolishing of Microchannels and its Application to Dialysis System." Procedia CIRP, vol. 5, pp. 164-168, 2013.

[36] C. P. Paul, P. Ganesh, S. K. Mishra, P. Bhargava, J. Negi, and A. K. Nath, "Investigating laser rapid manufacturing for Inconel-625 components." Optics & Laser Technology, vol. 39, pp. 800-805, 2007.

[37] L. C. Ardila, F. Garciandia, J. B. González-Díaz, P. Álvarez, A. Echeverria, and M. M. Petite, "Effect of IN718 Recycled Powder Reuse on Properties of Parts Manufactured by Means of Selective Laser Melting." Physics Procedia, vol. 56, pp. 99-107, 2014.

[38] V. Seyda, N. Kaufmann, and C. Emmelmann, "Investigation of Aging Processes of Ti-6Al-4 V Powder Material in Laser Melting." Physics Procedia, vol. 39, pp. 425-431, 2012.

[39] M. G. Rashed, M. Ashraf, R. A. W. Mines, and P. J. Hazell, "Metallic microlattice materials: A current state of the art on manufacturing, mechanical properties and applications." Materials & Design, vol. 95, pp. 518-533, 2016.

[40] T.-S. Lok and Q.-H. Cheng, "Elastic Stiffness Properties and Behavior of Truss-Core Sandwich Panel." Journal of Structural Engineering, vol. 126, pp. 552-559, 2000.

[41] D. Bhate, "Classification of Cellular Solids (and why it matters)," [Online], Available: http://www.padtinc.com/blog/the-focus/classification-of-cellular-solids-and-why-it-matters.

[42] N. S. K. Ho, P. Li, and G. B. Chai, "Compressive Deformation Behaviour of AlSi10Mg Microlattice Structures by Selective Laser Melting." the 6th European Conference on Computational Mechanics (ECCM 6), Glasgow, UK, 2018.

[43] M. Leary, M. Mazur, J. Elambasseril, M. McMillan, T. Chirent, and Y. Sun, "Selective laser melting (SLM) of AlSi12Mg lattice structures." Materials & Design, vol. 98, pp. 344-357, 2016.

[44] I. Ullah, J. Elambasseril, M. Brandt, and S. Feih, "Performance of bio-inspired Kagome truss core structures under compression and shear loading." Composite Structures, vol. 118, pp. 294-302, 2014.

[45] M. Smith, Z. Guan, and W. J. Cantwell, "Finite element modelling of the compressive response of lattice structures manufactured using the selective laser melting technique." International Journal of Mechanical Sciences, vol. 67, pp. 28-41, 2013.

[46] D. T. Queheillalt, Y. Murty, and H. N. G. Wadley, "Mechanical properties of an extruded pyramidal lattice truss sandwich structure." Scripta Materialia, vol. 58, pp. 76-79, 2008.

[47] R. B. Fuller, "Synergetic Building Construction " United States Patent, Patent Number: US2986241A, 1961.

[48] L. Dong, V. Deshpande, and H. Wadley, "Mechanical response of Ti–6Al–4V octet-truss lattice structures." International Journal of Solids and Structures, vol. 60-61, pp. 107-124, 2015.

[49] J. Tian, T. Kim, T. J. Lu, H. P. Hodson, D. T. Queheillalt, and D. J. Sypeck, "The effects of topology upon fluid-flow and heat-transfer within cellular copper structures." International Journal of Heat and Mass Transfer, vol. 47, pp. 3171-3186, 2004.

[50] A. G. Evans, J. W. Hutchinson, N. A. Fleck, M. F. Ashby, and H. N. G. Wadley, "The topological design of multifunctional cellular metals." Progress in Materials Science, vol. 46, pp. 309-327, 2001.

[51] J. Tian, T. J. Lu, H. P. Hodson, D. T. Queheillalt, and H. N. G. Wadley, "Cross flow heat exchange of textile cellular metal core sandwich panels." International Journal of Heat and Mass Transfer, vol. 50, pp. 2521-2536, 2007.

[52] S. Gu, T. J. Lu, and A. G. Evans, "On the design of two-dimensional cellular metals for combined heat dissipation and structural load capacity." International Journal of Heat and Mass Transfer, vol. 44, pp. 2163-2175, 2001.

[53] P. X. Jiang, M. Li, T. J. Lu, L. Yu, and Z. P. Ren, "Experimental research on convection heat transfer in sintered porous plate channels." International Journal of Heat and Mass Transfer, vol. 47, pp. 2085-2096, 2004.

[54] K. Boomsma, D. Poulikakos, and F. Zwick, "Metal foams as compact high performance heat exchangers." Mechanics of Materials, vol. 35, pp. 1161-1176, 2003.

[55] J. J. Hwang, G. J. Hwang, R. H. Yeh, and C. H. Chao, "Measurement of Interstitial Convective Heat Transfer and Frictional Drag for Flow Across Metal Foams." Journal of Heat Transfer, vol. 124, pp. 120-129, 2001.

[56] C. Hutter, D. Büchi, V. Zuber, and P. Rudolf von Rohr, "Heat transfer in metal foams and designed porous media." Chemical Engineering Science, vol. 66, pp. 3806-3814, 2011.

[57] M. L. Hunt and C. L. Tien, "Effects of thermal dispersion on forced convection in fibrous media." International Journal of Heat and Mass Transfer, vol. 31, pp. 301-309, 1988.

[58] R. Rezaey, "Experimental Investigation of Heat Transfer in Laser Sintered and Wire Mesh Heat Exchangers." Doctor of Philosophy, Department of Mechanical and Industrial Engineering University of Toronto, 2017.

[59] Gu, "Analysis of Thermal Conductive Characteristics of Non-Homogeneity Porous Foam," College of Power Engineering of Chongqing University, Chongqing, China, 2013.

[60] Y. Chai, X. Yang, X. Meng, Q. Zhang, and L. Jin, "Study of Micro-Structure Based Effective Thermal Conductivity of Graphite Foam." Journal of Heat Transfer, vol. 139, 2016.

[61] Q. Yu, B. E. Thompson, and A. G. Straatman, "A Unit Cube-Based Model for Heat Transfer and Fluid Flow in Porous Carbon Foam." Journal of Heat Transfer, vol. 128, pp. 352-360, 2005.

[62] A. G. Leach, "The thermal conductivity of foams. I. Models for heat conduction." Journal of Physics D: Applied Physics, vol. 26, pp. 733, 1993.

[63] T. J. Lu, H. A. Stone, and M. F. Ashby, "Heat transfer in open-cell metal foams." Acta Materialia, vol. 46, pp. 3619-3635, 1998.

[64] T. J. Lu, "Heat transfer efficiency of metal honeycombs." International Journal of Heat and Mass Transfer, vol. 42, pp. 2031-2040, 1999.

[65] T. Kim, C. Y. Zhao, T. J. Lu, and H. P. Hodson, "Convective heat dissipation with lattice-frame materials." Mechanics of Materials, vol. 36, pp. 767-780, 2004.

[66] S. Y. Kim, B. H. Kang, and J.-H. Kim, "Forced convection from aluminum foam materials in an asymmetrically heated channel." International Journal of Heat and Mass Transfer, vol. 44, pp. 1451-1454, 2001.

[67] H. Yan, X. Yang, T. Lu, and G. Xie, "Convective heat transfer in a lightweight multifunctional sandwich panel with X-type metallic lattice core." Applied Thermal Engineering, vol. 127, pp. 1293-1304, 2017.

[68] W. Lin, G. Xie, J. Yuan, and B. Sundén, "Comparison and Analysis of Heat Transfer in Aluminum Foam Using Local Thermal Equilibrium or Nonequilibrium Model." Heat Transfer Engineering, vol. 37, pp. 314-322, 2016.

[69] Ebnesajjad, S. Melt Processible Fluoroplastics, 1st ed.; William Andrew Publishing: New York, USA, 2002; pp. 151-193.

[70] Kim, H.K.; Sohn, J.S.; Ryu, Y.; Kim, S.W.; Cha, S.W. "Warpage Reduction of Glass Fiber Reinforced Plastic Using Microcellular Foaming Process Applied Injection Molding. " Polymers 2019, 11, 360.

[71] Shayfull, Z.; Sharif, S.; Zain, A.M.; Ghazali, M.F.; Saad, R.M. "Potential of Conformal Cooling Channels in Rapid Heat Cycle Molding: A Review. " Adv Polym Technol, vol. 33, pp. 1-24, 2014.

[72] Shine, M.S.; Ashtankar, K.M.; Kuthe, A.M.; Dahake, S.W.; Mawale, M.B. "Direct rapid manufacturing of molds with conformal cooling channels. " Rapid Prototyping, vol. 24, pp. 1347–1364, 2018

[73] Ahn, D.G. "Applications of laser assisted metal rapid tooling process to manufacture molding and forming tools. " Int J Precis Eng Man, vol. 12, pp. 925–938, 2011.

[74] Chen, X.; Lam, Y.C.; Li, D.Q. "Analysis of thermal residual stress in plastic injection molding. " J Mater Process Tech, vol. 101, pp. 275–280, 2000.

[75] Wang, T.H.; Young, W.B. "Study on residual stresses of thin-walled injection molding. " Eur Polymer, vol. 41, pp. 2511–2517, 2005.

[76] Rajamani, P.K.; Ageyeva, T.; Kovács, J.G. "Personalized Mass Production by Hybridization of Additive Manufacturing and Injection Molding. " Polymers, vol. 13, 2021

[77] Frazier, W.E. "Metal Additive Manufacturing: A Review. " J Mater Eng Perform, vol. 23, pp. 1917-1928, 2014

[78] Zhang, Y.; Wu, L.; Guo, X.; Kane, S.; Deng, Y.; Jung, Y-G.; Lee, J-H.; Zhang, J. "Additive Manufacturing of Metallic Materials: A Review. " J Mater Eng Perform, vol. 27, pp. 1-13, 2018.

[79] Guilong, W.; Guoqun, Z.; Huiping, L.; Yanjin, G. "Analysis of thermal cycling efficiency and optimal design of heating/cooling systems for rapid heat cycle injection molding process. " Mater Design, vol. 31, pp. 3426–3441, 2010.

[80] Hsu, F.H.; Wang, K.; Huang, C.T.; Chang, R.Y. "Investigation on conformal cooling system design in injection molding. " Adv Prod Eng Manag, vol. 8, pp. 107–115, 2013.

[81] Vojnova, E. "The benefits of a conformal cooling systems the molds in injection moulding process. " Procedia Eng, vol. 149, pp. 535– 543, 2016.

[82] Beard, R. "Why conformal cooling makes sense. " Plast Technol, vol. 60, pp. 34-37, 2014.

[83] Dimla, D.E.; Camilotto, M.; Miani, F. "Design and optimization of conformal cooling channels in injection moulding tools. " J Mater Process Tech, vol. 164-165, pp. 1294–1300, 2005.

[84] Venkatesh, G.; Ravi Kumar, Y.; Raghavendra, G. "Comparison of straight line to conformal cooling channel in injection molding. " Mater Today Proc, vol. 4, pp. 1167–1173, 2017.

[85] Saifullah, A.B.M.; Masood, S.H. "Cycle time reduction in injection moulding with conformal cooling channels. "In the Proceedings of the International Conference on Mechanical Engineering (ICME 2007), Dhaka, Bangladesh, 2007, pp. 42-44.

[86] Saifullah, A.B.M.; Masood, S.H.; Sbarski, I. "Thermal-structural analysis of bi-metallic conformal cooling for injection moulds. " Int J Adv Manuf Tech, vol. 62, pp. 123–133, 2012.

[87] Mazur, M.; Brincat, P.; Leary, M.; Brandt, M. "Numerical and experimental evaluation of a conformally cooled H13 steel injection mould manufactured with selective laser melting. "Int J Adv Manuf Tech, vol. 93, pp. 881–900, 2017

[88] Schmidt, W.R.; White, R.D.; Bird, C.E.; Bak, J.V. "Conformal cooling versus conventional cooling: an injection molding case study with P-20 and 3DPTM-processed tooling. " Mat Res Sco Sym Proc, vol. 625, pp. 51–56, 2000.

[89] Kanbur, B.B.; Shen, S.; Duan, F. "Design and Optimization of Conformal Cooling Channels for Injection Molding: A Review. " Int J Adv Manuf Tech, vol. 106, pp. 3253–3271, 2020.

[90] EOS Co., "aluminium AlSi10Mg material data sheet." [Online]. Available: http://www.eos.info/en.

[91] L. L. Hou, Z. X. Yin, and X. B. Fan, "Research status and development of aluminum matrix composite materials." Heat Treatment Technology, vol. 4, pp. 84, 2008.

[92] M. M. Dewidar, K. W. Dalgarno, and C. S. Wright, "Processing conditions and mechanical properties of high-speed steel parts fabricated using direct selective laser sintering." Journal of Engineering Manufacture, vol. 217, pp. 1651-1663, 2003.

[93] R.J. Moffat, Using uncertainty analysis in the planning of an experiment, Journal of Fluid Engineering vol. 107, pp. 173–178, 1985.

[94] C. Ji, Z. Qin, S. Dubey, F. H. Choo, and F. Duan, "Three-dimensional transient numerical study on latent heat thermal storage for waste heat recovery from a low temperature gas flow." Applied Energy, vol. 205, pp. 1-12, 2017.